Role of colloidal transport in the formation of high-grade gold veins at Brucejack, British Columbia

Nicolas J. Harrichhausen

Master of Science

Earth and Planetary Sciences

McGill University

Montréal, Québec

A thesis submitted to McGill University in partial fulfillment of the requirements of the degree of Master of Science

© Nicolas Harrichhausen 2016

Acknowledgements

This thesis would not have been possible without the contributions of many people. Firstly, I would to thank my supervisor Dr. Christie Rowe for taking this project on with me and providing me with the necessary feedback, ideas and encouragement throughout the whole process. I have yet to meet someone so enthusiastic about science and there is no one who could have motivated me better. I would also like to thank Dr. Warwick Board and Charles Greig, both geologists with Pretium Resources for their equally enthusiastic review and discussion on the Brucejack deposit. It was their passion for geology that first motivated me to return to research while working for Pretium Resources, and I appreciate all of their dedication to the project.

I would like to thank everybody at Pretium Resources. The staff both at the Brucejack camp and in the head office in Vancouver, provided excellent support for us during field work at the Brucejack camp. From organizing helicopter time to assisting in our work in the underground mine, the staff were always willing to help and accommodate us. I have great memories of all the wonderful people I have met at Brucejack over the years while working on this project and as a geologist for Pretium Resources.

While doing field work I had the great pleasure of being accompanied by undergraduate field assistants from McGill. Both Matthew Tarling and Paul Rakoczy were invaluable in mapping, taking structural measurements, and sample collecting at both Brucejack and Dixie Valley. They both had unwavering work ethic and enthusiasm, and their ideas on top of their great company made my field work a great experience. I would also like to thank Carla Gonzales for her contribution to the project as an undergraduate research thesis on the Mirrors samples. It was a pleasure to have you along to discuss the formation of the Mirrors.

Researching at McGill was a great experience mostly in part to the people in the Department of Earth and Planetary Sciences. The members of my research group, Nils Backeberg, Ben Melosh, Naomi Barshi, Noah Phillips, Samantha Carruthers, Erik Young and Catherine Ross all provided great discussion and moral support. I greatly appreciate the economic geology group at McGilll, led by Dr. Anthony Williams-Jones, allowing me to present my ideas at their "beer-talks" giving me further feedback on my research. Duncan McLeish, who just started his own Ph.D. project on Brucejack was especially helpful in discussion. I would also like to thank Pierrick Lamontagne-Hallé and Caitlin Beland for their help translating my abstract.

Analysis of the samples using the electron microscopes was a challenge for me as I was completely new to the process. I would like to thank David Liu, Line Mongeon, Weawkamol Leelapornpisit, and Lang Shi for all of their help in preparing samples and using the TEM and SEMs at McGill. In addition to analysis at McGill, one of our samples was analyzed at Fibics Inc. in Ottawa by Dirk Schumann. This was done without cost I would like to extend to Dirk my sincere gratitude.

This project was funded from a Natural Science and Engineering Research Council of Canada (NSERC) Collaborative Research Agreement (CRD) with Pretium Resources. Additional funding was received from the Society of Economic Geologists and Geoscience BC and their contribution has significantly benefited my during my time at McGill by allowing for me to visit more research conferences and spend more time doing field work.

My family and friends are the reason behind where I am today. My parents, Angela and

Martin, and my brother and sister, Justin and Carly, have never doubted my decisions and have always unconditionally loved and supported me.

Finally, I would like to dedicate this thesis to Matthew Huszar. Matt was a good friend and geologist at Brucejack who is no longer with us. Matt's honour's thesis at UBC on the Bridge Zone at Brucejack laid the foundation for scientific research at the Brucejack deposit and I will always remember his passion for science and adventure in life.

Contents

List of Tables

List of Figures

Abstract

Low solubility of Au in hydrothermal fluids at epithermal pressures and temperatures make it difficult to reconcile extremely localized, very high Au grades in epithermal vein deposits. Au has been known to form colloidal suspensions (sols) of nanoparticles when it is super-saturated within solution. Drop in temperature and/or pressure of hydrothermal fluids causing super-saturation of Au is also known to saturate a fluid with respect to silica leading to the precipitation of silica nanoparticles. Au can adhere to silica nanoparticles causing the stability of Au within suspension to be greatly enhanced increasing transport distance. A silica-protected Au sol allows a much higher flux of Au through a hydrothermal system and deposition of very concentrated Au grades within an epithermal vein system. Depressurization caused by fracture and fault-slip within the epithermal environment commonly causes super-saturation of silica leading to sudden precipitation of amorphous silica phases such as opal, which traps any suspended Au nanoparticles. Subsequent recrystallization of amorphous silica alters depositional textures by forcing nanoparticles to quartz grain boundaries. Deformation and metamorphism will further recrystallize quartz, obscuring evidence of this process.

This thesis presents structural data, and detailed optical and electron microscopy observations of epithermal quartz-carbonate vein stockwork systems at Brucejack, British Columbia and Dixie Valley, Nevada that are used to test a colloidal Au transport model. At the Jurassic aged Brucejack Au-Ag deposit, very high grades up to 41 582 ppm Au are reported within electrum that is hosted within metamorphosed and deformed quartz-carbonate stockwork. I show that initial stockwork development occurred during north-south extension and formation of mode 1 fractures with continued stockwork development within major normal fault zones. Electrum mineralization within these veins is shown to consist of an amalgamation of nanoparticles. Observations made on quartz formed within the recently active Stillwater fault zone at Dixie Valley, Nevada show that quartz here has recrystallized from an amorphous silica phase. Using these observations for comparison, quartz associated with nanoparticulate electrum at the much older Brucejack deposit is shown to also have recrystallized from an amorphous phase. The association between amorphous silica and nanoparticulate electrum indicates a colloidal origin for high-grade Au at the Brucejack deposit.

Abrégé

La faible solubilité de l'or dans les fluides hydrothermaux à des températures et pressions hydrothermales rend difficile la réconciliation avec des zones aurifères extrêmement localisées, à très hautes teneurs dans des gîtes à veines épithermales. Il est connu que l'or forme des suspensions colloïdales (sols) de nanoparticules lorsqu'il est sursaturé dans une solution. Une importante diminution température et/ou de pression des fluides hydrothermaux causant une sursaturation de l'or est aussi reconnue pour saturer le fluide en silice entraînant la précipitation de nanoparticules de silice. L'or peut adhérer aux nanoparticules de silices, améliorant considérablement la stabilité de l'or dans le fluide à être grandement améliorée, et ainsi augmenter la distance de transport. Un sol d'or protégée par de la silice permet un flux d'or beaucoup plus important dans le système hydrothermal et la déposition aurifère à très hautes teneurs dans un système de veines épithermales. La dépressurisation causée par la fracturation et le développement de failles dans un environnement épithermal provoquent communément une sursaturation de silice donnant lieu à une précipitation soudaine de phases amorphes de silice telle que l'opale, qui peut emprisonner les nanoparticules d'or en suspension. Une recristallisation subséquente de la silice amorphe altère les textures de déposition en forçant les nanoparticules aux surfaces des grains de quartz. La déformation et

le métamorphisme vont recristalliser le quartz, masquant les indications de ce processus.

Cette thèse présente des données structurales et des observations détaillées au microscopes optique et électronique du stockwork de veines épithermales de quartz-carbonates à Brucejack en Colombie-Britannique et à Dixie Valley au Nevada qui sont utilisées pour tester un modèle de transport d'or colloïdal. Au dépôt Jurassique Au-Ag de Brucejack, de très hautes teneurs allant jusqu'à 41 582 ppm d'or ont été rapportées dans l'électrum du stockwork déformé et métamorphisé de quartz-carbonate. Je démontre que le développement initial du stockwork s'est produit durant une phase d'extension nord-sud et durant la formation de fractures de type 1 en développement continu du stockwork dans des zones de failles majeures normales. La minéralisation en électrum dans ces veines semble consister d'un amalgame de nanoparticules. Des observations faites sur le quartz formé dans la zone récemment active Stillwater Fault à Dixie Valley au Nevada montre que le quartz a été recristallisé à partir d'une phase amorphe de silice. En comparant les observations des deux sites, on remarque que le quartz associé aux nanoparticules d'électrum au plus vieux dépôt Brucejack semble s'être également recristallisé à partir d'une phase amorphe de silice. L'association entre la silice amorphe et les nanoparticules d'électrum indique que les hautes teneurs aurifères du dépôt Brucejack sont d'origine colloïdale.

Contribution of authors

With permission of Geoscience BC, portions of this thesis contain edited versions of a publication titled, 'Structure of a high-grade, electrum-bearing quartz-carbonate vein stockwork at the Brucejack deposit, northwestern British Columbia,' published in the Geoscience BC Summary of Activities 2015. I, Nicolas Harrichhausen, was the lead author of this publication and undertook all data collection, analysis and interpretation. My supervisor Dr. Christie Rowe, and Pretium Resources geologists, Dr. Warwick Board and Mr. Charles Greig are listed as co-authors and their role was to provide editing advice. The portions of this thesis that contain text adapted from the Geoscience BC publication are sections 1.4, 2.1, 3.1, and 5.2.1. Figures adapted from that document are 2.1, 3.1, 3.2, 3.3, 3.4, and 5.2. The remainder of the work presented in this thesis was performed solely by Nicolas Harrichhausen.

CHAPTER 1

Introduction

One of the most commonly cited mechanisms for the formation of Au deposits invokes transport of Au in aqueous solution through the Earth's crust and localized precipitation due to changes in physical conditions or solution chemistry. Numerous examples of epithermal and orogenic deposits, where Au is contained in hydrothermal vein systems, have been explained by dissolved transport (e.g., Krupp and Seward, 1987; Simmons and Browne, 1990; Mikucki, 1998; Hayashi et al., 2001; Williams-Jones et al., 2009). However, solubility of Au in hydrothermal solutions is low (approximately 1-10 ppb in vapour and 100-1000 ppb in liquid; Heinrich et al., 2004; Williams-Jones et al., 2009; Zezin et al., 2011) and, in deposits where Au concentrations are highly variable and locally reach extremely high grades, it may be worthwhile to search for an alternative mechanism for Au transport and enrichment.

At the Brucejack deposit of Pretium Resources Inc. in northwestern British Columbia, Au is present as electrum, a Au-Ag alloy, within epithermal quartz-carbonate veins. These veins locally show extremely high grades of Au (up to 41 582 ppm), occurring as porous or dendritic blebs of visible electrum approximately 0.5-5 cm in size (Figure 1.1; Board and

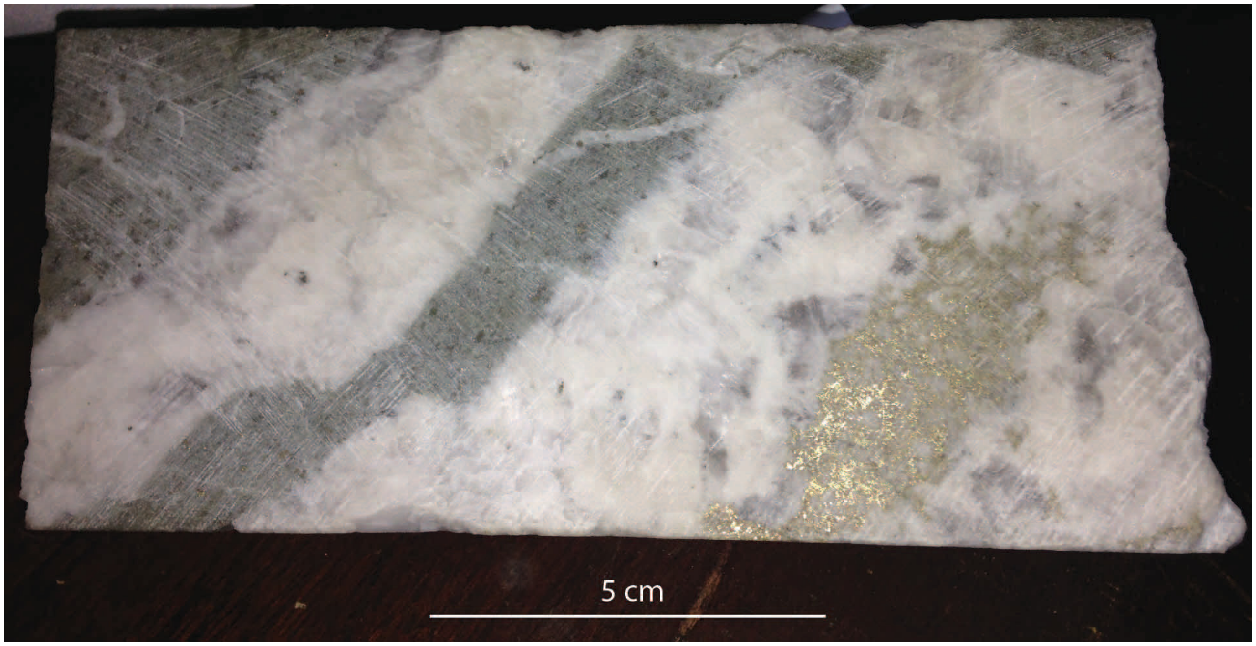

Figure 1.1 Photograph of drill core from the Brucejack deposit showing electrum bearing quartz-carbonate vein with extremely high Au grades. Electrum mineralization is seen at the bottom right of the photo. Drill core provided by Pretium Resources Inc.

McNaughton, 2013; Jones, 2013). However, the adjoining wallrock and vein material are typically low grade (<1 ppm Au). The extreme nugget effect, or inherent unpredictability, of the spatial statistics of the Au-assay population present complications for estimating the mineral resource. In order to help with resource estimation and further exploration, controls on Au mineralization, in particular the local enrichment of electrum within the quartz-carbonate veins, must be understood. The extreme concentration gradients of Au seen at Brucejack leads to the possibility that additional transport mechanisms may aid in localizing Au enrichment. One suggested mechanism is the transport of Au in colloidal suspension (e.g., Saunders, 1990; Herrington and Wilkinson, 1993; Saunders and Schoenly, 1995; Hough et al., 2008, 2011).

1.1 Au solubility

Though relatively insoluble, Au does complex with several species in order to form solutions under different conditions. Under epithermal conditions, i.e., <1.5 km depth and 150° to 300°C

(Taylor, 2007), the most important ligand to form a complex with Au is bisulphide, either forming $Au(HS)^{\circ}$ or $Au(HS)_2^-$ (Seward, 1973; Williams-Jones et al., 2009). Both experimental and field observation provide constraints on the maximum concentrations of Au bisulphide (plus other minor species) within typical epithermal hydrothermal fluids. Thermodynamic and phase relation modelling suggest the maximum dissolved concentration of Au is 1-2 ppm (Heinrich, 2005; Williams-Jones et al., 2009), while measured Au concentrations in brines taken from active hydrothermal systems are lower than 30 ppb (Figure 1.2).

It has been shown that a large economical Au deposit can be formed by an active Au-bearing hydrothermal system, with a typical geothermal flux, in a relatively short geological time span (<50 000 yrs) (Simmons and Brown, 2006, 2007). While this model of deposit formation may be reasonable for a low-grade bulk-tonnage deposit it does not address the problem of having a highly localized distribution of Au. Pearce et al. (2015b) showed that the flux of hydrothermal fluids calculated using silica alteration as an indicator for fluid flux, cannot account for the observed Au grades at a mesothermal Au deposit in Western Australia. A process of aggregation of Au within the system is required for the formation of high-grade localized Au mineralization. Simmons and Brown (2006) assume that all the Au is precipitated out of solution, and that flux of hydrothermal fluid remains constant. It has been argued that many auriferous vein deposits form during sudden depressurization of hydrothermal fluids during fracturing events (Sibson et al., 1988; Boullier and Robert, 1992; Weatherley and Henley, 2013; Peterson and Mavrogenes, 2014) causing a rapid precipitation of dissolved solids and very sharp reduction in permeability and flux through veins. Sudden localized depressurization is also used to explain the occurrence of localized areas of Au mineralization with grades well above its solubility limit (<10 ppm). If this is the case, then the mismatch between Au grades in veins and the solubility of Au in hydrothermal solutions dictates that this Au cannot be directly deposited from solution.

1.2 Colloidal Au transport

A colloid is a substance containing evenly dispersed particles ranging in size from 1-1000 nm (nanoparticles) in a stable suspension. When solid particles are dispersed throughout a liquid, the colloid is referred to as a sol (McNaught and Wilkinson, 2006). Sols containing nanoparticles of precious metals such as Au and Ag, and minerals such as naumannite and electrum, have been observed in nature and reproduced in the lab (e.g., Turkevich et al., 1953; Weitz and Oliveria, 1984; Benedetti and Boulëgue, 1991; Hough et al., 2008; Reith et al., 2012;

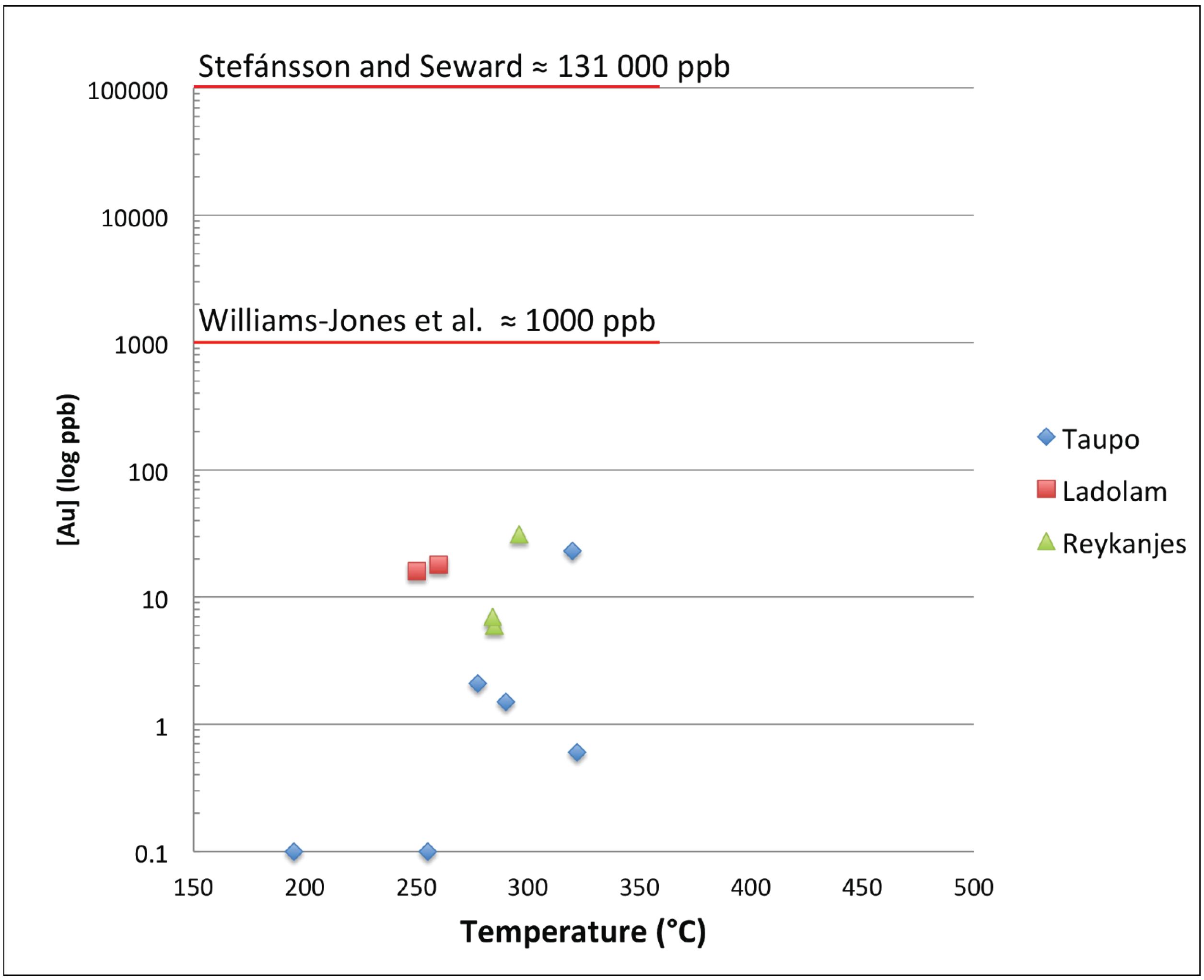

Figure 1.2 Maximum Au concentrations from experimental data (Stefánsson and Seward, 2004; Williams-Jones et al., 2009) compared with measured concentrations from geothermal brines. Taupo data is from Simmons and Brown (2007), Ladolam data is from Simmons and Brown (2006), and Reykjanes data is from Hardardóttir et al. (2009).

Saunders, 2012). Within the lab, formation of Au nanoparticles is commonly accomplished using the Turkevich method where a Au complex, tetrachloroauric acid ($HAuCl_4$), is reduced and the fluid is suddenly saturated with respect to Au (Turkevich et al., 1951; Kimling et al., 2006; Ojea-Jiménez et al., 2010; Doyen et al., 2013; Wuithschick et al., 2015). Similarily, in nature rapid precipitation of Au may also produce nanoparticles. Once formed they may be entrained in the rising hydrothermal fluid and would continue to grow to via Ostwald ripening. This process occurs when the volume-to-surface area ratio becomes big enough that momentum overcomes the repelling surface charge allowing them to collide and stick due to van der Waals forces (orthokinetic aggregation) (Frondel, 1938; McNaught and Wilkinson, 2006). As their radii increase their ability to be transported within a hydrothermal fluid decreases. In other words, the stability of the colloid decreases and would tend towards coagulation and potential deposition (Frondel, 1938; Wiese and Healy, 1970; Saunders, 1990). Coagulation may also be aided by the presence of NaCl which provides a positively charged ion that negatively charged Au nanoparticles can use as a bridge (Iller, 1979; Saunders, 1990), also leading to growth and potential settling from suspension.

Textural evidence of Au nanoparticles within a hydrothermal ore deposit has been recognized at the Sleeper deposit by Saunders (1990). Since then, further textural evidence of metallic nanoparticles, such as Au, Ag, electrum, naumannite, and chalcopyrite have been found at several epithermal deposits (Moiseenko and Kulik, 2010; Saunders, 2012), as well as within supergene deposits (Hough et al., 2008; Reith et al., 2010; Fairbrother et al., 2012). The evidence for nanoparticles has mostly been observed using optical microscopy and scanning electron microscopy (SEM) imaging of the morphology of metals in veins. Shapes and geometries that resemble a coagulation of small spherical nanoparticles have been reported, as well as instances of isolated nanoparticles (Figure 1.3a, b; Moiseenko and Kulik, 2010; Hough et al., 2011; Reith et al., 2012; Saunders et al., 2015). The propensity of colloids to coagulate with certain fractal geometries (Weitz and Oliveria, 1984; Weitz et al., 1985; Lin et al., 1989) is also used as evidence for the precipitation of metallic nanoparticles (Figure

1.3c; Schoenly and Saunders, 1993; Saunders and Schoenly, 1995; Saunders, 2012). The isolation of individual nanoparticles and their internal structure has been studied using transmission electron microscopy (TEM) using samples of nano-Au in arsenian pyrite (Reich et al., 2006; Hough et al., 2011) and Au nanoparticles created in the lab (Figure 1.3d; Scott et al., 2012). These studies indicate that Au nanoparticles have a crystalline lattice structure. Recently, Hannington et al. (2016) observed Au grades within geothermal reservoir fluids in the Reykjanes geothermal field, increasing over a period of 7 years to an order of magnitude above the Au solubility limit. They argue that the increase in Au is due to depressurization and increased boiling caused to extraction of brine for geothermal energy, and that Au must exist as a colloidal suspension for it to occur at their measured concentrations.

Metallic nanoparticles may precipitate and immediately coagulate and be deposited in place (e.g., Mikhlin and Romanchenko, 2007), or they may stay in suspension and travel within hydrothermal fluids (e.g., Trefry et al., 1985). A sol may be able to transport a greater concentration of a substance with low solubility than a saturated solution alone. Transport as a sol would require the presence of nanoparticles which may persist as evidence after metal deposition. Collisions of Au nanoparticles during transport, causing orthokinetic coagulation, may limit the distance a Au or electrum colloid can travel. However, the stability of these colloids has been shown to be enhanced by the presence of a silica colloid. Frondel (1938) shows that when Au sols are protected by colloidal silica they are stable in the presence of an electrolyte and up a temperature of up to 410°C. This protected Au sol forms when nanoparticles of Au adhere to larger silica particles and are less likely to collide with other Au nanoparticles and coagulate. Au nanoparticles have been shown to adhere to larger silica nanoparticles under different laboratory conditions. These techniques require the functionalization (change of surface chemistry) of silica spheres by attaching, or precipitating particles, or ions to the surface of silica spheres in order for Au nanoparticles to deposit on, or be adhered to them. Au nanoparticles have been adhered to silica nano-spheres functionalized using hydrophilic groups (Westcott et al., 1998), or Sn and Ag ions (Lim et al.,

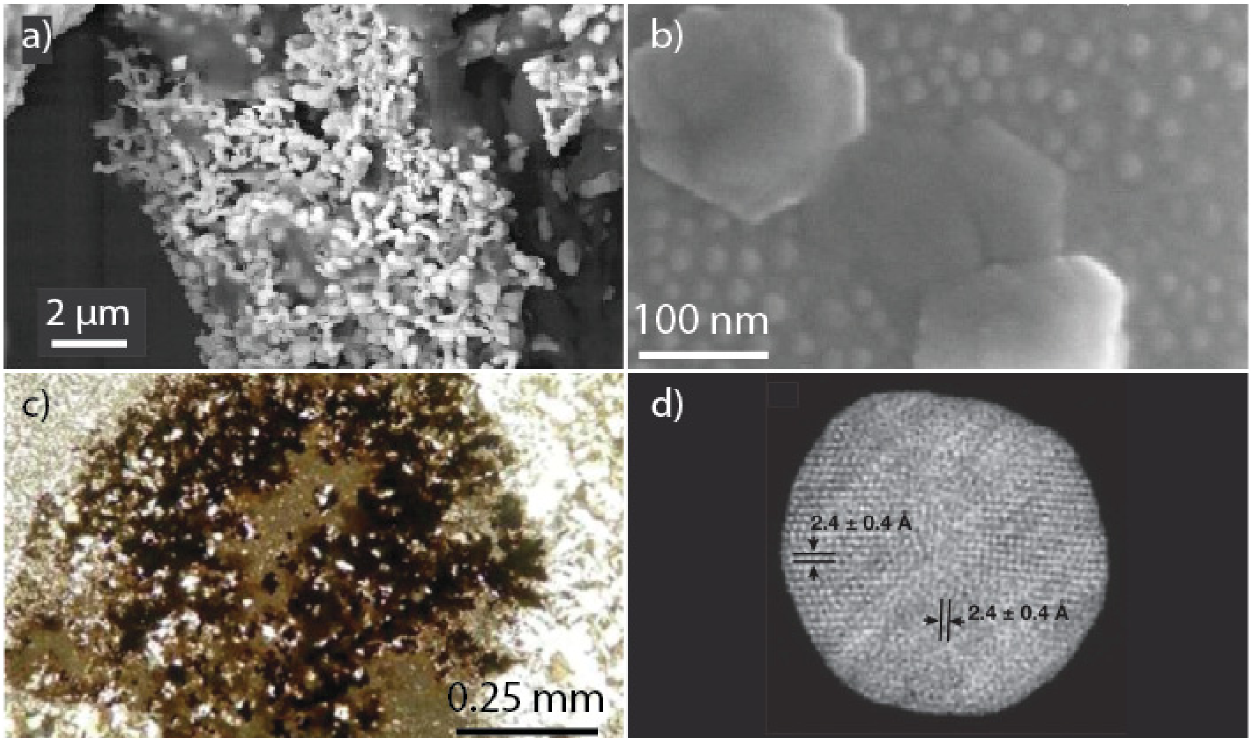

Figure 1.3 Textural evidence of Au nanoparticles revealed by optical microscopy, SEM, and TEM. a) Field emission scanning electron microscope (FEG-SEM) image of a conglomerate of secondary Au micro-crystals in a silica-rich matrix of an eluvial Au grain from a highly weathered quartz-vein deposit near Reefton, New Zealand. Modified from Reith et al. (2012). b) FEG-SEM image of hexagonal and spherical Au nanoparticles from a supergene (secondary) Au deposit sample from the Golden Virgin Pit in Western Australia. Modified from Hough et al. (2011). c) Plain polarized light (PPL) optical micrograph of a fractal dendrite of electrum from the Sleeper epithermal Au deposit, Nevada. Opaque phase is electrum while recrystallized opal is shown in beige and fine grained quartz is shown in white. Modified from Saunders (2012). d) 3.36 angstrom thick slice of a lab precipitated Au nanoparticle imaged using scanning transmission electron microscopy (STEM) showing internal crystalline structure. Modified from Scott et al. (2012).

2003; Kobayashi et al., 2005). If this adhering process can happen within a hydrothermal fluid, it may allow Au to be more efficiently transported as a sol. Amorphous silica spheres are known to form when a solution is supersaturated with respect to silica (Steefel and Van Cappellen, 1990). If conditions promote both this and Au nanoparticle formation, or the direct adsorption of Au nanoparticles from solution onto the silica surfaces, a protected Au sol may form allowing for Au to be transported for long distances in quantities above its solubility limit.

Recent studies using Pb, Re-Os, Cu, and S isotope data from epithermal deposits with colloidal textures indicate that precious metals may not have precipitated in the shallow epithermal systems where they are found. Kamenov et al. (2007) and Saunders et al. (2008, 2015) show that isotope ratios from these precious metals differ from those of gangue minerals within the same veins. Gangue minerals have ratios that indicate mixing between meteoric water and magmatic water while the precious metals have ratios indicating that they formed from a magmatic fluid source alone.

If precious metal did originate in a deeper part of the hydrothermal system and was transported as nanoparticles, a mechanism is required for them to coagulate, or accumulate within ore. Charged surfaces on sulphide minerals such as pyrite may attract negatively charged Au nanoparticles (Frondel, 1938) from within a sol and act as a point for local precious metal nanoparticle accumulation (Herrington and Wilkinson, 1993). If they are attached to silica nanopoarticles as a sol, then entrainment of those of silica particles during silica vein formation would effectively deposit the Au with silica, as suggested by Herrington and Wilkinson (1993). Because the solubility of silica is much higher than Au, a sudden vein formation occurring due to supersaturation with respect to silica (Steefel and Van Cappellen, 1990; Okamoto et al., 2010), would trap Au nanoparticles.

1.3 Amorphous silica

Precious metal mineralization has been associated with the precipitation of amorphous silica at several localities (e.g., Saunders, 1990; Herrington and Wilkinson, 1993; Bozkaya and Banks, 2015). Amorphous silica can form when quartz is amorphosed into a gel due to friction during fault slip (Hayashi and Tsutsumi, 2010; Bestmann et al., 2012; Nakamura et al., 2012; Kirkpatrick et al., 2013). It can also form when a fluid becomes supersaturated with respect to silica, due to the nucleation rate of amorphous silica being much higher than that of quartz under supersaturated conditions (Steefel and Van Cappellen, 1990; Okamoto et al., 2010). Silica superaturation commonly occurs at temperatures lower than 250°C (Fournier, 1985a,b), or with a sudden change in physical conditions such as temperature and/or pressure, or chemical factors such as pH. These changes may also deposit associated precious metals. In addition, the sudden precipitation of amorphous silica species may trap any suspended solids within hydrothermal fluids and act as a deposition mechanism. Hydrothermal fluids drop in temperature and pressure as they travel upwards within the crust due to lithostatic/hydrostatic pressure and geothermal gradients. A nearly instantaneous change in the hydrothermal fluid environment due to dilation associated with hydrofracture or seismic rupture, or fluid introduction, may be required for silica supersaturation and amorphous silica precipitation (Hedenquist and Henley, 1985; Saunders, 1994).

A sudden increase in volume due to rock fracture and/or slip can be an effective way to decrease both temperature and pressure in a hydrothermal environment. Fault-valve processes (Sibson et al., 1988; Cox, 1995; Peterson and Mavrogenes, 2014) and dilational fractures in local or regional extensional settings (e.g., Sibson, 1992; Micklethwaite et al., 2010) can effectively increase volume and decrease pressure by up to a few orders of magnitude (Weatherley and Henley, 2013). Thus, quartz veins formed along active faults and within damage zones at low temperatures provide a likely place for amorphous silica precipitation, and ideal sites to look for entrapment of precious metal nanoparticles. Fault-hosted epithermal precious metal deposits provide both the right structural and low temperature setting for these veins to form and previous studies show that some of these deposits have veins with textures indicating amorphous silica deposition (e.g., Saunders, 1990; Herrington and Wilkinson, 1993; Dong et al., 1995; Saunders, 2012; Marinova et al., 2014).

Due to the metastability of amorphous silica phases under typical geological conditions, they recrystallize to quartz over a relatively short geologic time period (e.g., Kastner et al., 1977; Williams et al., 1985; Herdianita et al., 2000; Lynne et al., 2005; Lee, 2007). Amorphous opaline silica sinter deposits often form as surface expressions to geothermal systems. Non-crystalline opal has been described as a gel consisting of an aggregate of silica particles with water-filling interstitial spaces (e.g., Jones et al., 1964; Graetsch, 1994). Without significant burial, silica sinter deposited as amorphous opal-A crystallizes to poorly crystalline opal-CT

Mosaic: areas of abundant microcrystalline quartz crystals with interpenetrating and tortuous grain boundaries (Lovering, 1972; Saunders 1990; Dong, 1995).	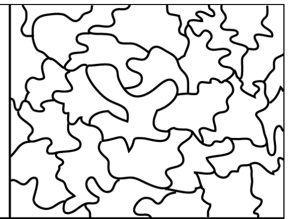
Flamboyant: radial extinction of quartz crystals with a rounded crystal outline. Either surrounds and extends radially from a euhedral core defined by inclusions or is present throughout entire crystal (Adams, 1920; Sander and Black, 1988; Dong, 1995)	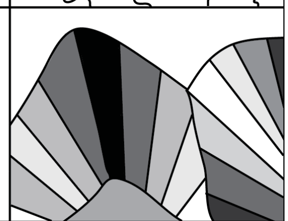
Feathery: Similar to flamboyant but with less developed grains. Has a feathery appearance in cross-polarized light due to slight optical difference in extinction positions. This occurs radially around a euhedral core or in patches (Adams, 1920; Sander and Black, 1988; Dong, 1995).	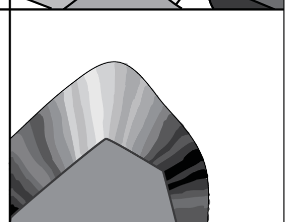
Ghost sphere: commonly seen in microcrystalline quartz where the distribution of impurities or inclusions form spheres (Adams, 1920; Dong, 1995; Kirpatrick, 2013; Faber 2014).	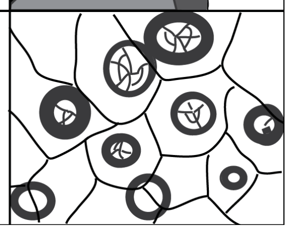

Figure 1.4 Descriptions and sketches showing quartz textures seen in thin section that indicate recrystallization from amorphous silica. Sketches modified from Dong et al. (1995) and descriptions modified from Adams (1920); Lovering (1972); Sander and Black (1988); Saunders (1990); Dong et al. (1995); Kirkpatrick et al. (2013); Faber et al. (2014).

and/or opal-CA within the timespan of 10,000 to 50,000 years and after about 50,000 years to microcrystalline quartz, reducing total water content and increasing density (e.g., Williams et al., 1985; Herdianita et al., 2000; Lynne et al., 2005; Lee, 2007). At higher pressure and temperatures (3 kb and 100°-300°C), silica gel or opal-A has been found to recrystallize directly to quartz with no intermediate silica phases (Oehler, 1976). Recrystallization to quartz occurs much more quickly (opal-A to opal-C in less than 50 years), if initial silica deposition occurs with other materials such as calcite or organic matter (Herdianita et al., 2000). The presence of adsorbed Au nanoparticles on silica spheres also may also accelerate the overall recrystallization process (Pol et al., 2003). As the the structure of quartz permits few impurities within its crystal lattice, any impurities such as metals will be forced to the grain boundaries (Herrington and Wilkinson, 1993). This will affect visible vein textures as well as destroy any relict texture indicating transport of precious metal nanoparticles by a silica-protected sol. However, there are quartz textures that may indicate it's original deposition as an amorphous phase. In hand sample, the presence of cryptocrystalline quartz may indicate a precursor amorphous phase. Several more of these textures in thin section are described by Dong et al. (1995), and can be seen in Figure 1.4. Fournier (1985a) also suggests that the presence of abundant fluid inclusions is evidence for dehydration of silica during recrystallization of a silica gel to quartz. As the majority of quartz vein deposits in the geological record are much older than 50 Ka and have been held at elevated temperatures and pressure, these textures are key in determining the importance of amorphous silica precipitation during quartz vein formation. Some authors suggest that many quartz veins formed in epithermal environments could have initially formed with an amorphous silica species (e.g., Fournier, 1985a; Herrington and Wilkinson, 1993; Okamoto et al., 2010), and this step in vein formation may be very important in controlling ore mineral deposition.

1.4 Objective of this study

The purpose of the study is to test the potential for colloidal deposition and contextualize the role of colloidal transport of Au in the formation of high-grade epithermal Au deposits by examining both quartz and electrum for evidence of relict nanoparticles (cf. Saunders, 1990; Hough et al., 2011; Kirkpatrick et al., 2013; Faber et al., 2014). Very high-grade Au mineralization at Brucejack provides a good setting to test for colloidal transport in that is hard to reconcile localized high-grade Au using a transport-by-solution model alone. A Au-bearing hydrothermal system at Dixie Valley, Nevada is also examined in order to better determine the role of amorphous silica in colloidal Au transport. The instability of amorphous silica under normal geologic conditions does not allow it to persist for long periods of time before recrystallizing into quartz. To better understand the effect of recrystallization I compare quartz vein samples from the metamorphosed Jurassic Brucejack deposit, with the much younger auriferous hydrothermal system at Dixie Valley. Here, on the historically active Stillwater fault zone (Caine et al., 2010), amorphous silica with up to a few weight percent

Figure 1.5 TEM images of silica from the Stillwater fault zone in Dixie Valley, Nevada. Amorphous silica with $\sim$ 3 wt. % Au (A). As amorphous silica recrystallizes Au concentration drops (B) until it is below detection limit in completely recrystallized quartz (C). Taken from Rowe et al. (2012).

Au is reported (Figure 1.5; Rowe et al., 2012). This amorphous silica is formed on fault plane slicken-surfaces while adjacent recrystallized quartz on the same surface contains Au below measurement detection limits. Nearby, Au ore has also been mined from the fault-related quartz vein and vein stockwork systems at the Dixie Comstock mine (Vikre, 1994). At these locations, amorphous silica and quartz have undergone less alteration and recrystallization than seen at Brucejack, and will provide a useful analogue representing a fresh deposit with Au and associated amorphous silica.

In order to determine whether colloidal transport plays a role in high-grade Au mineralization, this thesis uses observations from the Brucejack deposit and Dixie Valley to address the following questions:

1. **Is there textural evidence for the deposition of Au nanoparticles?** Electron microscopy was used to observe ore textures at the nanoscale to determine if isolated precious metal nanoparticles are present, or if high-grade Au or electrum is present as an agglomeration of smaller particles. Textural evidence for precious metal nanoparticles has been reported before within different deposit types and in laboratory conditions. If this evidence is observed, it will show that Au or electrum has been deposited as nanoparticles.

2. **Are there specific structural trapping sites for Au nanoparticles and amorphous silica precipitation?** An essential aspect of the study was to describe and interpret the structural relationships within the faults, extensional veins and stockwork that constitute vein systems, and to understand the roles of hydrofracture, fault slip and static fluid flow in controlling vein-mineral precipitation and Au distribution. An aim of the project was to understand the specific deformational context of the formation of enriched veins at Brucejack. Understanding this included the differentiation of sites of structural dilation that may have contributed to precipitation of amorphous silica and subsequent entrapment of suspended precious metal nanoparticles. The structural setting at Dixie Valley was examined in order to confirm that the Stillwater fault zone is a useful analogue to the older metamorphosed Brucejack deposit. If the potential for colloidal precious metal transport at Brucejack can be established, and specific trapping sites for colloidal deposition are determined, key pieces of a depositional model for this site and others can be put in place for future mineral exploration.

3. **Is there evidence of long distance transport of Au nanoparticles?** The formation of amorphous silica at depth within a hydrothermal system may provide silica nanoparticles for precious metals to adhere to and be transported efficiently. Formation of amorphous silica may also play a role in electrum deposition by trapping nanoparticles during quick precipitation of veins. An association between amorphous silica and electrum will provide evidence of an efficient mechanism for the transport of precious metal nanoparticles over distance and their deposition.

CHAPTER 2

Background geology

2.1 Brucejack

2.1.1 Tectonic setting

The Brucejack deposit is hosted by rocks of the Early Jurassic lower Hazelton Group, a package of arc-related volcano-sedimentary rocks within the Stikinia terrane. Stikinia, along with other Paleozoic-Mesozoic arc and oceanic terranes of the Intermontane Belt, is interpreted to have accreted to ancestral North America by mid-Jurassic time forming a part of the western Canadian Cordillera (Figure 2.1; Monger et al., 1982; Nelson and Colpron, 2007; Gagnon et al., 2012). Following accretion, Stikinia was subjected to at least one major episode of compressional deformation during the mid-Cretaceous formation of the northeast-verging, sinistral-transpressive Skeena fold-and-thrust belt (Evenchick, 1991, 2001). This deformation gave rise to the McTagg anticlinorium (Henderson et al., 1992), where the thickness of the lower Hazelton Group decreases considerably from the east to the west limb. The change in stratigraphic thickness is interpreted by Nelson and Kyba (2014) to represent

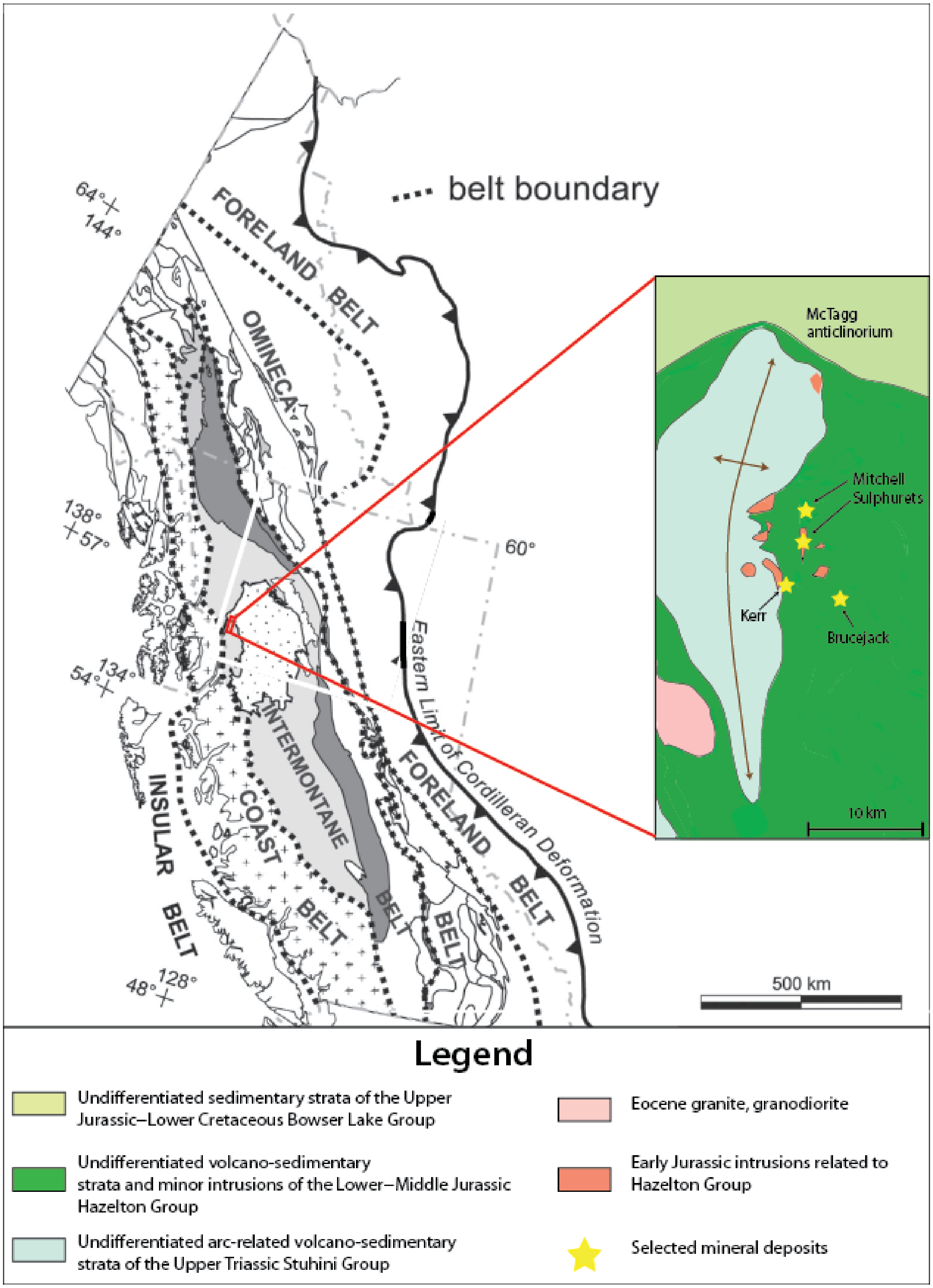

Figure 2.1 Terrane map of the western Canadian Cordillera showing the location of the Brucejack deposit within the Intermontane Belt. The other major belts of the western Canadian Cordillera are shown and labelled. The lightest grey colouring within the Intermontane Belt indicates rocks of the Stikinia terrane. Map taken from Evenchick et al. (2005). Inset on right shows a simplified regional geology map with the location of the McTagg anticlinorium. The stars show the locations of three major copper-Au porphyry deposits, as well as the Brucejack Au-Ag epithermal deposit. Legend applies only to the inset. Geology contacts from Erdmer and Cui (2009) and legend modified from Nelson and Kyba (2014).

the presence of a paleostructural highland along the axis of the McTagg anticlinorium and a volcano-sedimentary basin to the east. Hazelton Group deposition within this basin was coeval with displacement along basin-bounding faults. Several large mineral deposits, including the Kerr-Sulphurets-Mitchell (KSM) copper-Au porphyries and the epithermal Brucejack Au vein-stockwork system, are located along a narrow south-southeast trend just east of the axis of the McTagg anticlinorium and are interpreted to relate to Jurassic magmatic and hydrothermal systems controlled by the basin-bounding faults (Figure 2.1; Nelson and Kyba, 2014; Febbo et al., 2015).

2.1.2 Deposit geology and mineralization

Quartz-carbonate stockwork veining in the Brucejack deposit hosts the majority of a total mine reserve of 7.3 million oz. Au and 35.3 million oz. Ag (proven and probable reserves), with the majority of the high-grade Au resource located within the Valley of the Kings (VOK) Zone (Jones, 2013). The VOK is one of several, almost continuous, zones of Au and Ag mineralization located along a band of quartz-sericite-pyrite (QSP) altered latite lavas and breccias, and associated immature volcaniclastic rocks. This stratigraphy has been interpreted to have undergone N-S compression forming steep easterly plunging gentle folds with a wavelength of ~1 km (Figure 2.2; Board and McNaughton, 2013; Jones, 2013). These fold axes are folded by a north-trending syncline, suggesting polyphase deformation (Board and McNaughton, 2013; Jones, 2013). This observation is consistent with polyphase-deformation recorded in mid-Jurassic to early Cretaceous clastic sequences within the Bowser Basin that overlies Hazelton Group strata (Evenchick, 2001), and three phases of deformation recorded within the nearby Mitchell copper-Au porphyry deposit (Febbo et al., 2015). Peak metamorphism, up to lower-greenschist facies, coincided with the beginning of the formation of the Skeena fold-and-thrust belt at 110 Ma (Kirikham and Margolis, 1995; Evenchick, 2001). The early Jurassic Brucejack deposit predates this metamorphism and deformation (Kirikham and Margolis, 1995; Board and McNaughton, 2013; Jones, 2013).

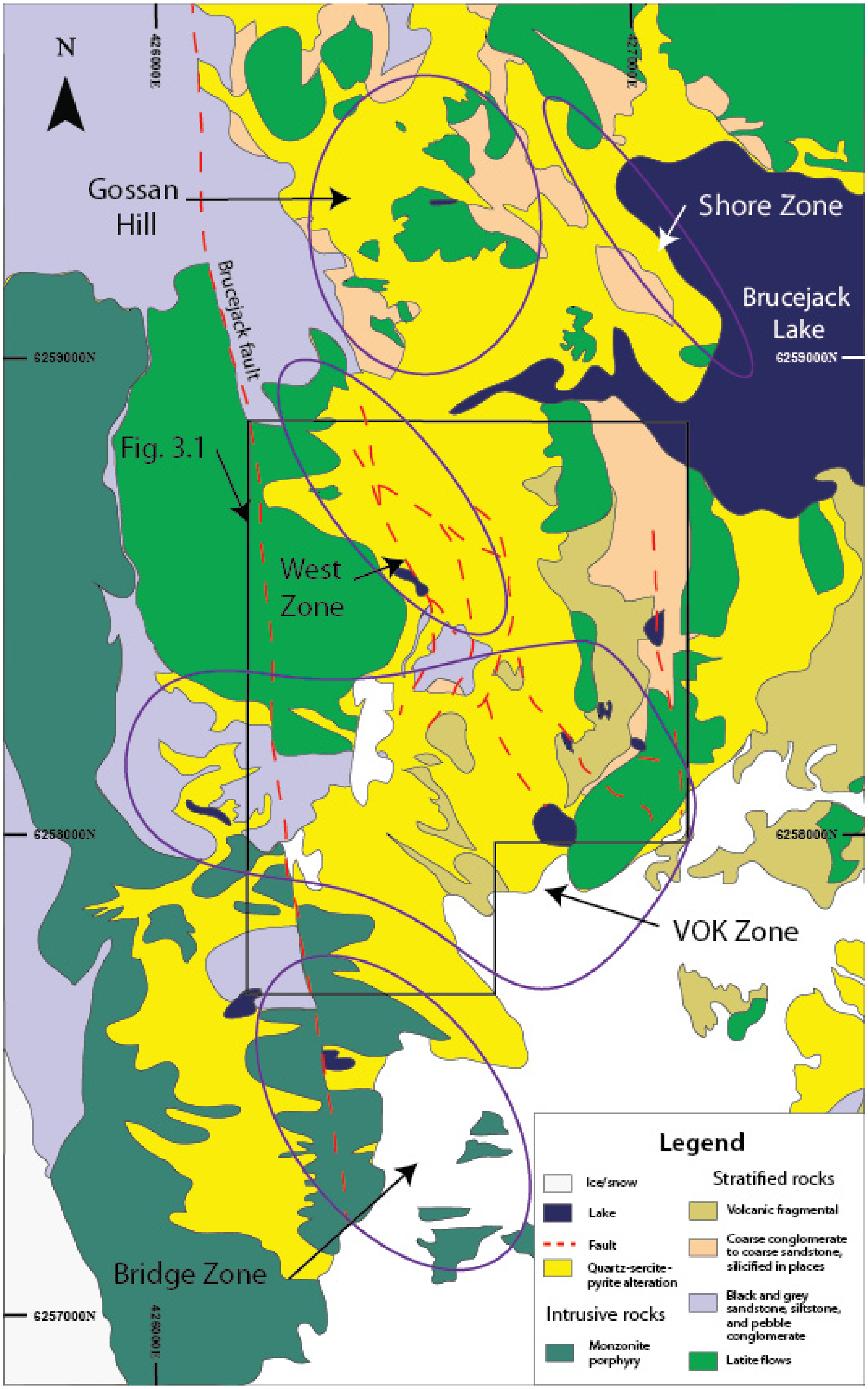

Figure 2.2 Brucejack property geology map showing location of different mineralization zones described by Pretium Resources Inc. (Jones, 2013; Pretium Resources Inc., 2013) and the location of Figure 3.1. Map adapted from Pretium Resources Inc. (2013).

Lenses of silicified conglomerate have been identified as a marker horizon that outlines the stratigraphy within the band of quartz-sericite-pyrite (QSP) alteration. Stockwork-vein systems follow an east-northeast trend and dip sub-vertically, subparallel to host rock foliation, however, this foliation is believed to postdate vein formation (Kirkham, 1992; Davies et al., 1994; Board and McNaughton, 2013; Jones, 2013). Within stockwork zones, veins may occur in many different orientations. Although mineralization is hosted within veins, higher grades are not clearly correlated with vein intensity because diffuse stockwork zones with a smaller percentage of vein material may contain significant electrum.

Table 2.1 shows several generations of veining that have been documented in the Brucejack deposit. Board and McNaughton (2013); Jones (2013); Tombe (2015) describe these generations as follows. Pyrite veins (vein 0) that are suggested to be associated with early QSP alteration are cross-cut by electrum-bearing quartz-carbonate veins (vein 1a-c). These quartz-carbonate veins exist as dense stockwork and stockwork breccia, and as parallel, decimetre- to metre-spaced, layered 1-10 cm-wide vein sets. They, in turn, are cut by quartz-carbonate veins containing base-metal sulphides (sphalerite, galena, chalcopyrite), electrum, and Ag sulphide mineralization (vein 2). A third generation, manganoan carbonate-quartz veining (vein 3), contains local high-grade electrum mineralization. Quartz-chlorite fibrous slicken veins and tension gashes (vein 4), associated with later (probably Skeena fold-and-thrust belt) shortening, cross-cut all earlier vein systems. They contain limited chalcopyrite and no reported electrum. Thin syntaxial quartz veins represent a later sub-horizontal vein generation (vein 5) that may be related to erosional unloading following structural uplift.

Fluid-inclusion thermobarometry completed by Tombe (2015) yielded homogenization temperatures of approximately 160°C. Tombe (2015) interpreted these to indicate co-trapping of liquid and vapour inclusions, suggesting that boiling probably occurred during quartz precipitation. The vein generations have not been individually dated, but rhenium-osmium dates on molybdenite suggest some of the veining occurred at 188 Ma (Tombe, 2015). Cross-cutting relationships between an electrum-bearing generation of veins and 182.7 Ma, late

Vein Generation	Description	Mineralization
Vein 0	Discontinuous pyrite stringers and veinlets	Zoned pyrite containing nano-inclusions of arsenopyrite, galena, sericite, calcite, rutile, chalcopyrite, and electrum
Vein 1a	Continuous sheeted or isolated narrow quartz or quartz-carbonate veins with syntaxial growth of quartz that are deformed and may form ptygmatic textures.	Zoned pyrite with inclusions in vein 0 pyrite, can contain discrete visible electrum
Vein 1b	Zones of quartz-carbonate vein breccia and pervasively silica altered wallrock	Zoned pyrite with inclusions, can contain discrete visible electrum
Vein 1c	Metre-wide multiphase quartz-carbonate veins and vein breccias that can extend over 100 m along strike and be up to several metres wide	Zoned pyrite with inclusions, galena, sphalerite, chalcopyrite, apatite, monazite, titanite, Ag sulphosalts, and visible electrum
Vein 2	Continuous (often >10m along stirke) base metal rich quartz-carbonate veins that can be from 1 cm to 1m in width	Pyrite, sphalerite, galena, Ag sulphosalts, Ag-rich electrum
Vein 3	Orange to pink calcite-quartz veins that can be up to 40 cm wide. Carbonate is the dominant vein mineral	Abundant electrum is present in one particular vein, chalcopyrite
Vein 4	Thrust fault associated quartz-carbonate-chlorite veins that form along fault planes, within damage zones, and as tension gashes	Rare chalcopyrite
Vein 5	Thin subhorizontal vuggy quartz veins with syntaxial texture	None

Table 2.1 Vein generations 0 through 5 at the Brucejack deposit modified from Pretium Resources, unpublished data, 2015

syn- to post-mineralization monzonite dikes suggest that the latest electrum-mineralizing event may have occurred at this time (Pretium Resources Inc., 2013). Volcanic rocks on the property range in age from 196 to 182 Ma (U-Pb zircon, Pretium Resources Inc., 2013), and porphyritic intrusions related to copper-Au mineralization at the nearby KSM deposit have yielded U-Pb zircon ages of 197 to 189.9 Ma (Bridge, 1993; Febbo et al., 2015). If the deposits are related to the same magmatic activity, these dates suggest a magmatic-hydrothermal system lasting up to 15 million years.

Jones (2013) showed that electrum mineralization occurs in the VOK zone with a 2:1 ratio of Au to Ag while to the north it occurs in association with an increased presence of sulphides with a ratio down to 1:40 Au to Ag. This change in ratio and increased sulphides may represent different mineralizing events or a zonation in temperature and alteration away from a magmatic source for hydrothermal fluids. In the VOK zone, electrum occurs as discrete blebs and dendrites within veins that can yield drill core grades as high as 41,582 ppm Au (Board and McNaughton, 2013; Jones, 2013). Electrum lies along the grain boundaries of quartz grains, within fractures of and adjacent to pyrite grains, as inclusions within pyrite mineralization, and within fractures in calcite. Although electrum occurs along with a variety of other minerals it is discretely localized throughout stockwork systems and exhibits a fairly random distribution within mineralized zones. High-grade deposition sites are surrounded by relatively low-grade vein material, giving the deposit an extreme nugget value and presenting challenges when modelling.

2.2 Dixie Valley

2.2.1 Tectonic setting

Dixie Valley is located within the Basin and Range province of Nevada where Late Cenozoic crustal extension has formed multiple horst and graben sequences (e.g., Hintze, 1973; Zoback et al., 1981; Okaya and Thompson, 1985). Figure 2.3 shows the location of the eastward dipping normal Stillwater fault zone (SFZ) on the western edge of the Dixie Valley. The eastern slope of the Stillwater range is the exposed footwall of this fault zone (Caine et al., 2010), and the graben forming Dixie Valley has been down-dropped approximately 3-6 km along the SFZ. The valley is filled with late Tertiary and Pleistocene alluvial and lacustrine sediments deposited syn-tectonically (Power and Tullis, 1989). Crystalline rocks that are offset by the

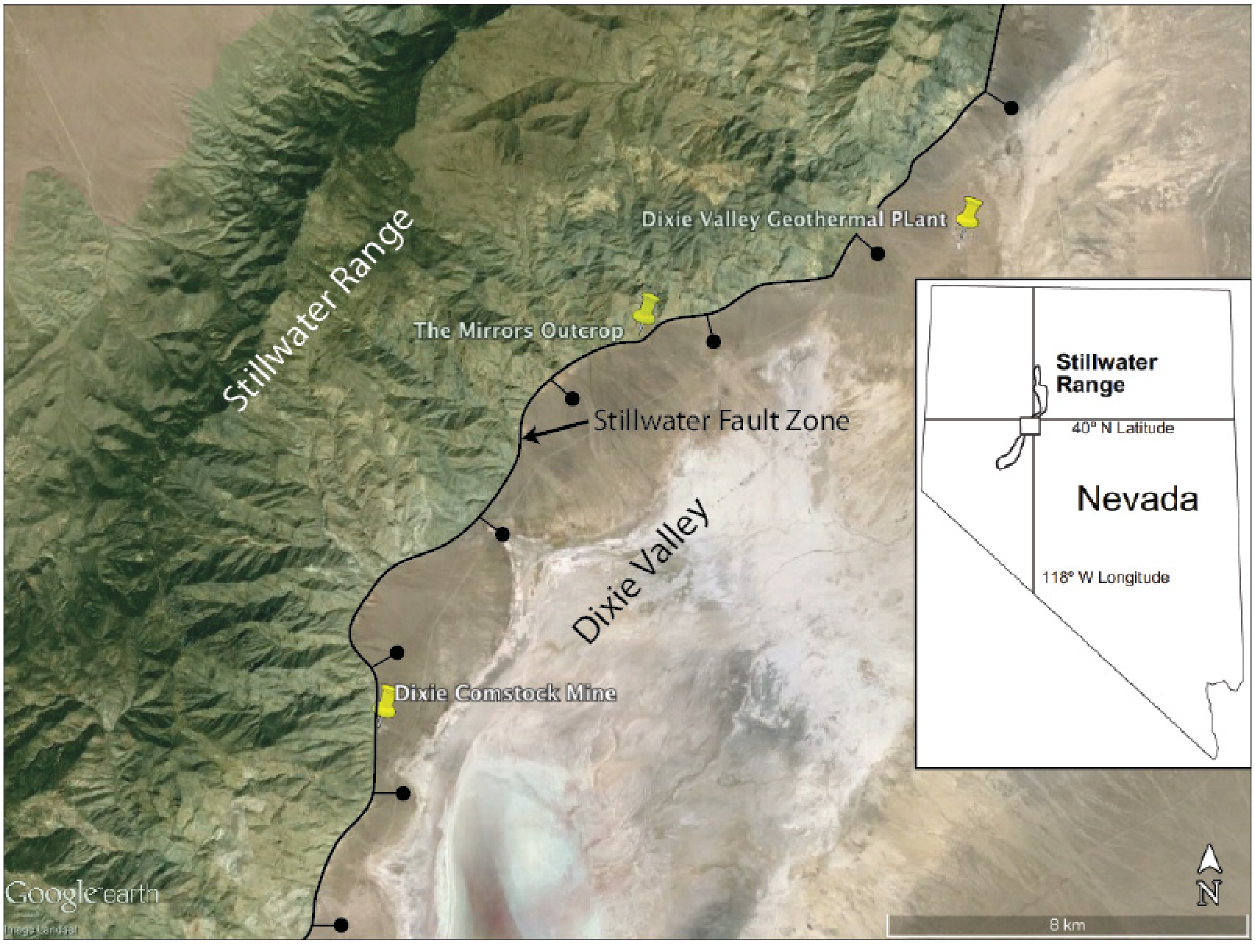

Figure 2.3 Google Earth^{TM} image of the location of the SFZ in Dixie Valley, Nevada. SFZ trace is from Caine et al. (2010). Locations of the Mirrors outcrop, the Dixie Comstock mine, and the Dixie Valley geothermal plant are shown. Inset on right shows the location of the Stillwater range within the state of Nevada (taken from Caine et al., 2010).

fault include variably metamorphosed Mesozoic rocks unconformably overlain by Tertiary sedimentary and volcanic rocks, the youngest of which is an 11-17 Ma basalt unit (Page, 1964; Hastings, 1979; Fonseca, 1988; Power and Tullis, 1989). Steep geothermal gradients (Denton et al., 1980; Parchman and Knox, 1981) have resulted in vigorous hydrothermal circulation as evidenced by hot springs within the Dixie Valley (providing geothermal energy) and alteration and veining along the fault zone. Different segments of the SFZ in ruptured in1915 and 1954 resulting in a 40 km long seismic gap between them, where no known earthquakes have occurred in the last 300 years (Wallace and Whitney, 1984). Within this seismic gap, along the SFZ, lie the Mirrors locality and the Dixie Comstock Au mine.

2.2.2 The Mirrors

The Mirrors locality is an exposed portion of the exhumed footwall and slip surfaces of the SFZ described in detail by Power and Tullis (1989) and by Caine et al. (2010). At this location, a unique coating of fine-grained quartz forms several shiny surfaces that reflect in the sunlight. The footwall here is mapped as Jurassic gabbroic and dioritic rocks (Page, 1964), while the hanging wall consists of Quaternary alluvium. Power and Tullis (1989) concluded that the slip surfaces formed at depths less than 2 km and a temperature less than 270 °C. Detailed outcrop mapping by Caine et al. (2010) indicates that the fault zone here consists of several slip surfaces with a broad range of orientations and a mean slip surface orientation striking northeast to east-northeast and dipping 32° to 70,° towards the southeast with predominantly normal dip-slip motion.

A schematic of the SFZ (Figure 2.4) shows the fault zone (within the footwall) is composed of a highly silicified fault core, containing pods of matrix-supported breccia contained within clast-supported breccia, and a broader damage zone of fractured intrusive rocks (Caine et al., 2010). Quartz-carbonate and cryptocrystalline silica veins filling open space within breccias are related to the fine-grained silica-coated slip surfaces (Power and Tullis, 1989; Caine et al., 2010). Caine et al. (2010) suggests that the microcrystalline quartz within the breccia and slickenside surfaces was formed during an abrupt drop in pressure in hydrothermal fluids due to coseismic dilatancy. In contrast, Power and Tullis (1989) suggest that the slickenside surfaces formed by the modification of hydrothermally precipitated silica by non-brittle, relatively low strain, continuous deformation (i.e., solution creep), while the breccias are a result of high strain discontinuous deformation.

2.2.3 Dixie Comstock mine

Approximately 7 km southeast of the Mirrors locality along the SFZ, lies the historic Dixie Comstock Au mine which produced an estimated 4600 oz of Au (10,000 t ranging from 0.5-3 oz/t) from 1938 to 1970 (Vikre, 1994). Au ore was mined from the middle of the

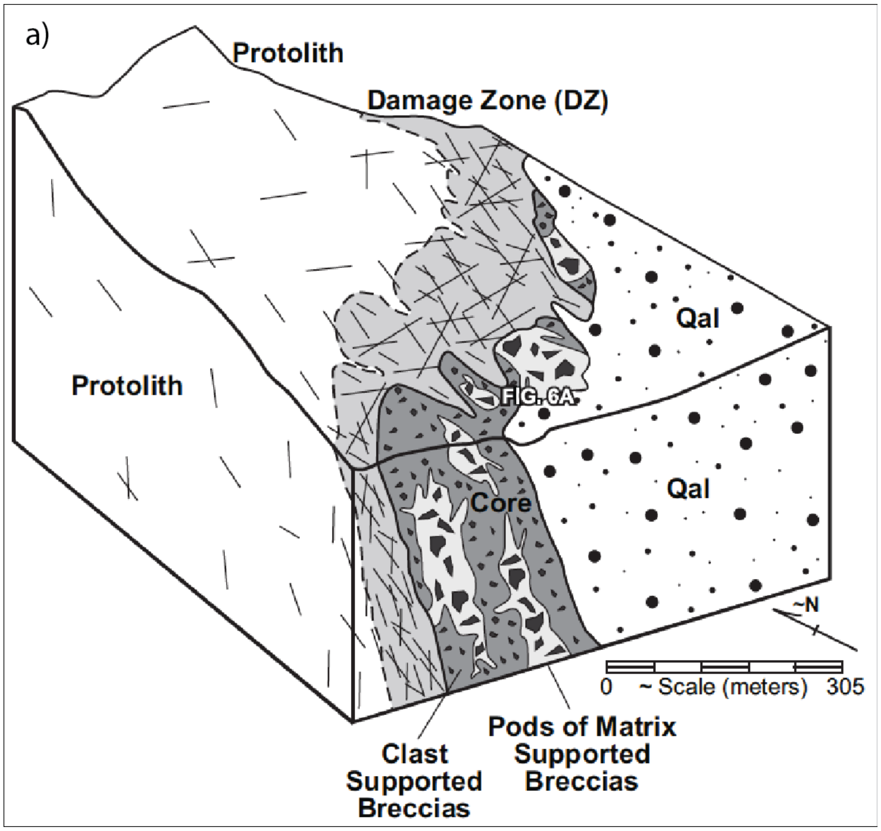

Figure 2.4 Detailed schematic of the SFZ (taken from Caine et al., 2010).

main range-bounding fault zone (the SFZ) and consists of quartz-carbonate breccia, quartz stockwork veins, crushed gabbro and fault gouge (Vikre, 1994). Footwall and hanging wall rocks are mapped the same as the Mirrors locality (Page, 1964). The SFZ here is up to 76 m thick, strikes north and dips 40°-45° to the east, reflecting a significant bend along strike from the Mirrors. Higher grade Au occurring as electrum is found largely as discrete grains in the first generation of cloudy, fine-grained quartz that cements and replaces clasts of a matrix supported breccia that makes up part of the fault zone. A second generation of euhedral quartz and third generation of vug filling calcite are generally not mineralized (Vikre, 1994). It is suggested that a single hydrothermal event was responsible for Au mineralization, that this event occurred at a relatively low temperature around 180° C and low depth (>100 m), and that it was sourced entirely from meteoric water (Vikre, 1994). Precipitates from geothermal fluids recovered in 1983 containing 27 ppb Au and 1.2 ppm Ag (Vikre, 1994), indicate Au mineralization could still be occurring along the SFZ.

CHAPTER 3

Observations: Brucejack

Field observations of quartz-carbonate stockwork veining at Brucejack were made over two field seasons during August 2014 and August 2015. Observation, mapping, and sampling took place on surface outcrop and within the underground exploration development of the Brucejack mine. Additional high-grade vein samples were also provided in the form of drillcore and thin section by Pretium Resources Inc. Samples were cut and analyzed by optical microscopy, backscattered electron imaging (BSE) using a scanning electron micrscope (SEM), electron dispersive X-ray spectroscopy (EDS), and transmission electron microscopy (TEM).

3.1 Structural setting

In order to document the scale and geometry of the vein system at Brucejack, detailed maps were prepared of vein orientations, lithology, and faulting at a scale of tens of metres, on surface exposures of major vein systems. These were then linked, in part using drillhole intersections, to structural measurements underground, where the same vein systems were intersected by active workings. Aerial photographs were acquired using a lightweight drone (DJI Phantom3 Advanced). Low-altitude airphotos were used to construct a three-dimensional surface model from which a detailed georeferenced orthophoto was extracted (methods described in Johnson et al., 2014). The orthophotos have a scale of approximately 1-2 pixels/cm depending on the size of the outcrop. Veins were then mapped directly onto these orthophotos using a tablet, with locations of structural measurements and vein descriptions denoted by station names. Rock types were mapped directly onto paper printouts of the outcrop orthophotos. Three outcrop areas were mapped, two of which are interpreted in this thesis (shown in Figure 3.1). These two areas were chosen to get a good representation of the stockwork systems at Brucejack. The third map area (Figure 3.1, map area 3) appears in the appendix (Figure A1). Each of these areas is located around stockwork systems of different size and orientation, and within different host rocks or alteration assemblages. The first interpreted location (Figure 3.1, map area 1) was also chosen because this vein system may be correlative with Domain 20, an important Au-bearing vein system that is well exposed in the underground workings of the Brucejack mine. This stockwork system is shown to extend underground for 400 m along strike (east-southeast) and at least 400 m vertically (steeply south dipping, Pretium Resources Inc., unpublished data, 2015). The second interpreted location (Figure 3.1, map area 2), was chosen as it contains a vein system proximal to near surface, high-grade Au drillcore samples, as well as thrust faults that outcrop at surface.

Map area 1

Figure 3.2a presents the detailed outcrop geology of map area 1 (location shown in Figure 3.1). This outcrop is part of a large, steeply south-dipping stockwork system that strikes east-southeast to the west of the map area. Figure 3.1 shows northeast- to east-trending veins directly east of map area 1 that are part of an area of pervasive quartz-carbonate stockwork that extends east and southeast for several hundred metres. Previous detailed surface mapping (Figure 3.1) shows that the stockwork system in map area 1 may actually

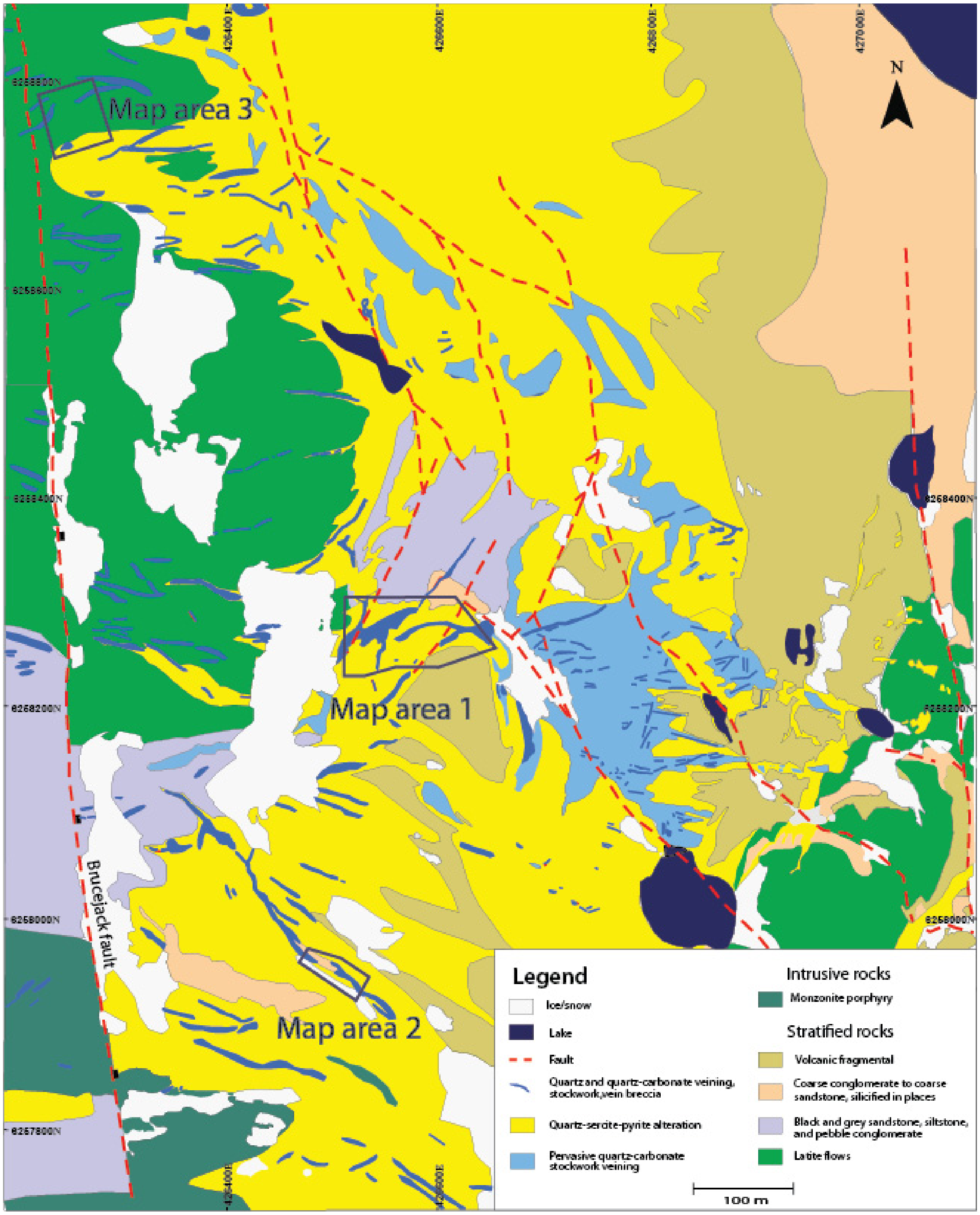

Figure 3.1 Simplified deposit geology of the VOK zone at the Brucejack Au-Ag deposit (modifed from Pretium Resources Inc., unpublished data, 2015), with schematic representation of quartz-carbonate veining, stockwork and breccia (true thickness of veins ∼ 0.5-10 m). Detail of map area 1 is shown in Figure 3.2. Stockwork system shown in map area 1 extends to the southeast as a broad zone of stockwork with both southeast- and east-striking veins. Detail of map area 2 is shown in Figure 3.5. The stockwork system shown in map area 2 extends as narrow vein stockwork to the northwest and southeast. Detail of map area 3 is shown in appendix (Figure A1).

consist of several large, en echelon stockwork zones (Pretium Resources, unpublished data, 2015).

Figure 3.2a shows that map area 1 contains several composite quartz veins, the largest of which is up to 10 m wide and strikes ∼240° for at least 60 m. The boundaries of the smaller individual veins that form the composite 10 m-wide zone can be distinguished only on the weathered surface of the outcrop. Some of these individual veins are subhorizontal, creating a weathering-resistant cap that may enhance the strong positive relief of the vein. On the southern edge of the intensely veined zone is 10-20 m of less intense stockwork and vein networks cutting intact wallrock, where several additional parallel subsidiary stockwork zones, up to 4 m in width, were mapped. At the eastern edge of the mapped area, there is a 2-3 m wide quartz vein that strikes east. At the western edge of the main stockwork zone, a 2 m wide fault zone offsets veining in a reverse right-lateral sense (Figure 3.2a, station C15). To the north, several veins join with the main stockwork zone. These east-southeast-trending veins can be up to a metre wide. Stockwork veining surrounding the intensely veined core is typically asymmetric with respect to width about the core (Figure 3.2a) and may consist of subsidiary zones of dense stockwork veining ∼1 m wide. Along strike to the northeast from the intensely veined core, several continuous quartz-carbonate veins up to 1 m in width continue out of the map area at the same 060° azimuth as the main zone (station C34).

In total, 273 vein orientations were measured at indicated stations throughout the map area (Figure 3.2a, b). Mapping and equal-area projection plots of these veins indicate at least three sets of orientations: 1) continuous, east- to northeast-striking veins, up to 1 m wide, that are parallel with the main (en echelon) stockwork zones; 2) discontinuous, north-trending veins and veinlets (many below map scale on Figure 3.2a) located mainly in the eastern half of the map area; and 3) centimetre-scale, subhorizontal veins associated with dense stockwork zones. Many of the quartz-carbonate veins throughout the area of surface outcrop change orientation near intersections with other veins. Intersections where several veins coalesce are common, with each vein bending or following a previous fracture or vein toward a single

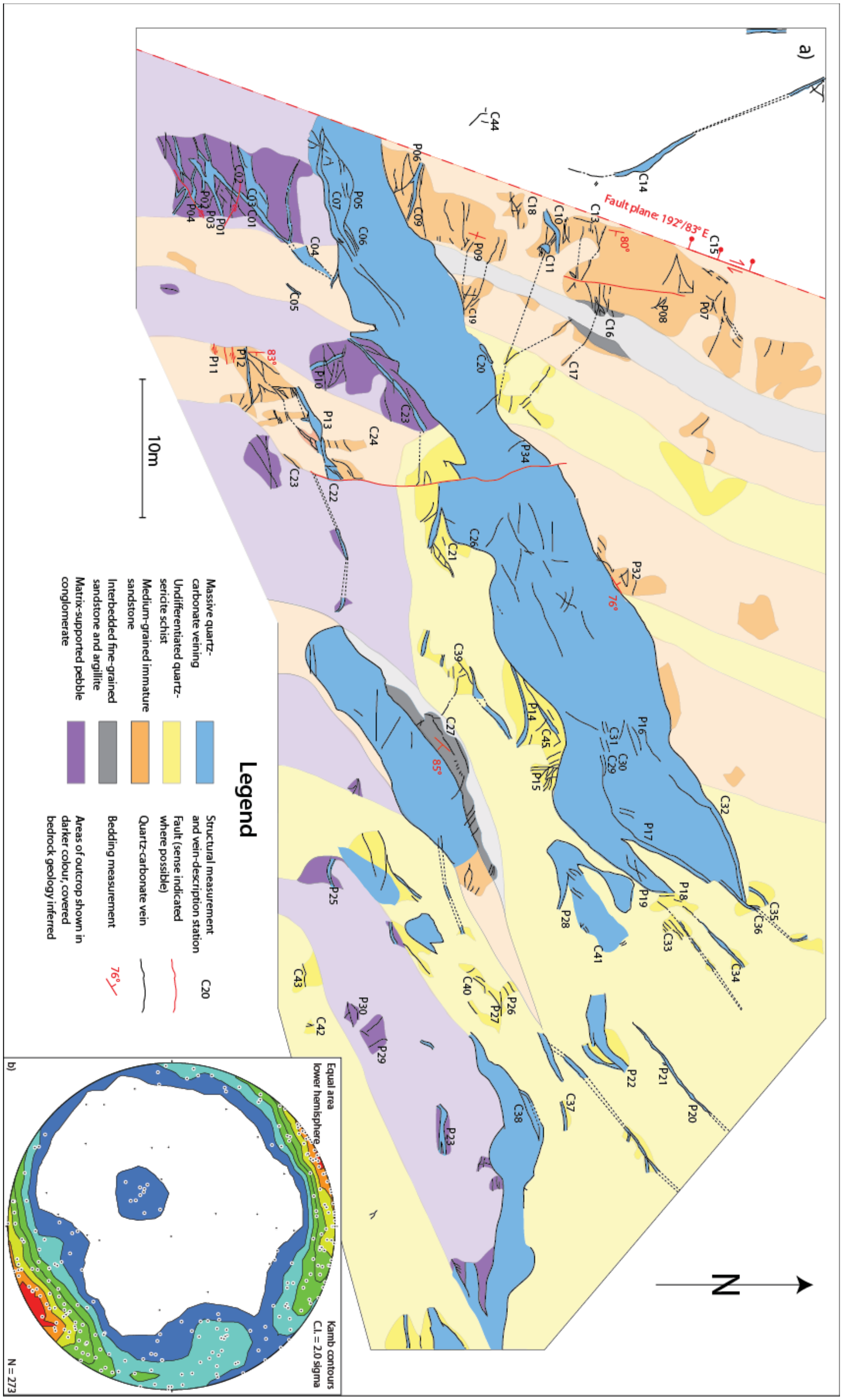

Figure 3.2 a) Lithology, stockwork quartz-carbonate veining and faults in map area 1 of the Brucejack Au-Ag deposit (see Figure 3.1 for location). b) Equal-area projection of poles to vein orientations measured at stations indicated in (a); Kamb contour interval at 2σ indicate concentration of poles.

intersection (Figure 3.3a). This geometry is evidence that at least some of the veins were open fractures when subsequent veins formed, acting as free surfaces to reorient the local stress field during crack propagation (e.g., Fossen, 2016).

Lithological mapping is difficult due to the intensity of the QSP alteration around the stockwork veining, which obliterated diagnostic rock textures. The rock type close to the intense veining is predominantly undifferentiated quartz sericite schist. However, where primary sedimentary textures can be observed, units of immature medium-grained sandstone, interbedded finer-grained sandstone and argillite, and matrix-supported pebble conglomerate are mapped. To the north of the main stockwork zone are regular, 3-10 m wide beds of coarse sandstone, interbedded sandstone and undifferentiated quartz-sericite schist. To the south are irregular beds of pebble conglomerate. This juxtaposition of dissimilar rock sequences across the stockwork zone suggests that it coincides with a fault. Measurements and contact traces indicate that stratigraphy dips steeply towards the east and strikes north-northeast to northeast.

Minor faults mapped to the south of the main stockwork zone show minor left- and right-lateral apparent offset on the 10-50 cm scale. Only 12 exposed fault planes were measured in map area 1, which is not enough for a kinematic analysis, but a distinct set of faults was observed that is parallel to the large fault cutting the main stockwork zone on the western side of the map area. These faults strike south-southeast and dip steeply to the east. A few steeply dipping faults subparallel to the main stockwork are also exposed. They show both right-lateral (Figure 3.3b) and left-lateral apparent offset (Figure 3.2a, stations P01, P04, P11). Several veins have been deformed into disharmonic folds (Figure 3.3c). The axial plane of these folds strikes $\sim 35°$ with approximately subvertical dip, indicating some southeast-directed shortening that postdates vein formation.

Veins in map area 1 (Figure 3.2a) are predominantly quartz with minor calcite, although a small stockwork zone with 0.5-1 m thick, grey-weathering blocky calcite was mapped directly southeast of the main stockwork (Figure 3.2a, station C31). These carbonate veins show

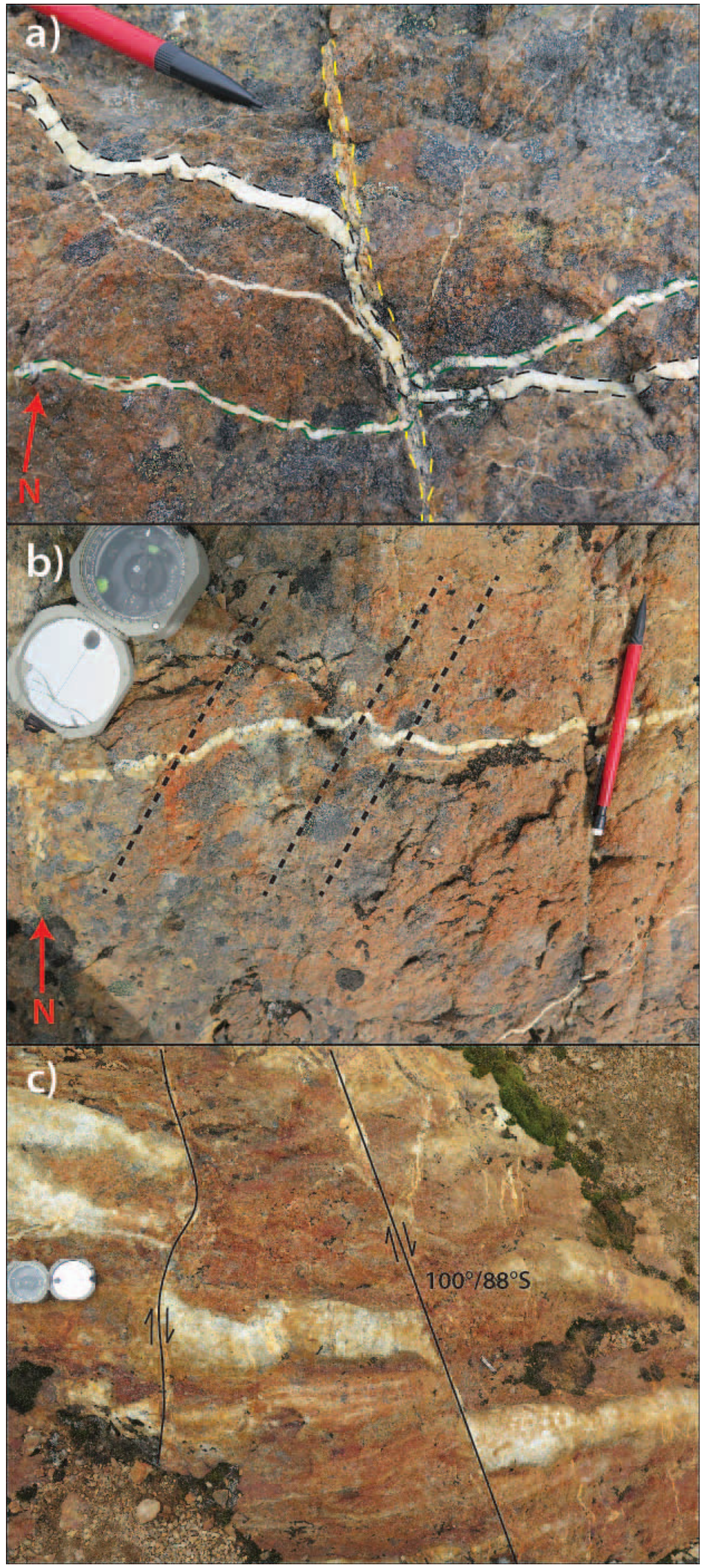

Figure 3.3 Photographs showing textures and geometry of veins and faults in map area 1. a) Syntaxial quartz-carbonate veins bending and coalescing (green and black) along the surface of an earlier vein (yellow), station P10 (Figure 3.2a). b) Disharmonic folding of a quartz-carbonate vein, the axial planes of the folds trending approximately 035°, station P10 (Figure 3.2a). C) Two subvertical faults showing approximately 20 cm of apparent dextral offset of sandstone beds, station P11 (Figure 3.2a).

multiple phases of mineralization, with quartz layers in the centre and along the wallrock, as well as along fractures within the grey calcite. Quartz in this area displays a bladed crystal habit similar to that of calcite, suggesting that it replaced calcite. Within the main stockwork zone, multiple phases of veining cross-cut one another and are locally brecciated. Similarily, large bull quartz veins were observed in the underground workings cross-cutting early-silicified wallrock and breccia, as well as early veins of banded colloform quartz with local cores of cryptocrystalline silica. Quartz growth in most veins, where it can be observed, is syntaxial, with symmetric crystal growth away from the wallrock toward the centre of the vein (e.g., Bons et al., 2012). Similar euhedral to blocky quartz is also found as rims on many of the breccia clasts, with radial quartz growth occurring from clast boundaries into pore space. Both of these textures suggest there was open-space growth of quartz.

Where the tentatively related stockwork system (Domain 20) is exposed in the walls of underground workings down-dip from map area 1, patterns similar to those observed at surface emerge (Figure 3.4a). However, the vein orientations underground represent only a portion of vein orientation population measured on surface. Steep to moderately dipping veins exposed in the underground workings strike east-southeast (Figure 3.4b), while steeply dipping veins on surface strike in all directions with the largest concentration striking east-northeast (Figure 3.2b). The thickest veins may dominate the pattern seen in weathered outcrop, which makes more apparent at surface but indistinct on the equal-area projection that includes all vein measurements. Underground, a distinct set of vertical veins parallel to and south of the main stockwork is seen. Sigmoidal tension gashes that cross-cut steep veins occur in the footwall of a significant reverse fault. However, these definitive fault-related veins are the latest stage of veining seen in Figure 3.3a and do not appear to be related to the stockwork veining in Domain 20.

Map area 2

Figure 3.5 presents the detailed outcrop geology of map area 2 (location shown in Figure

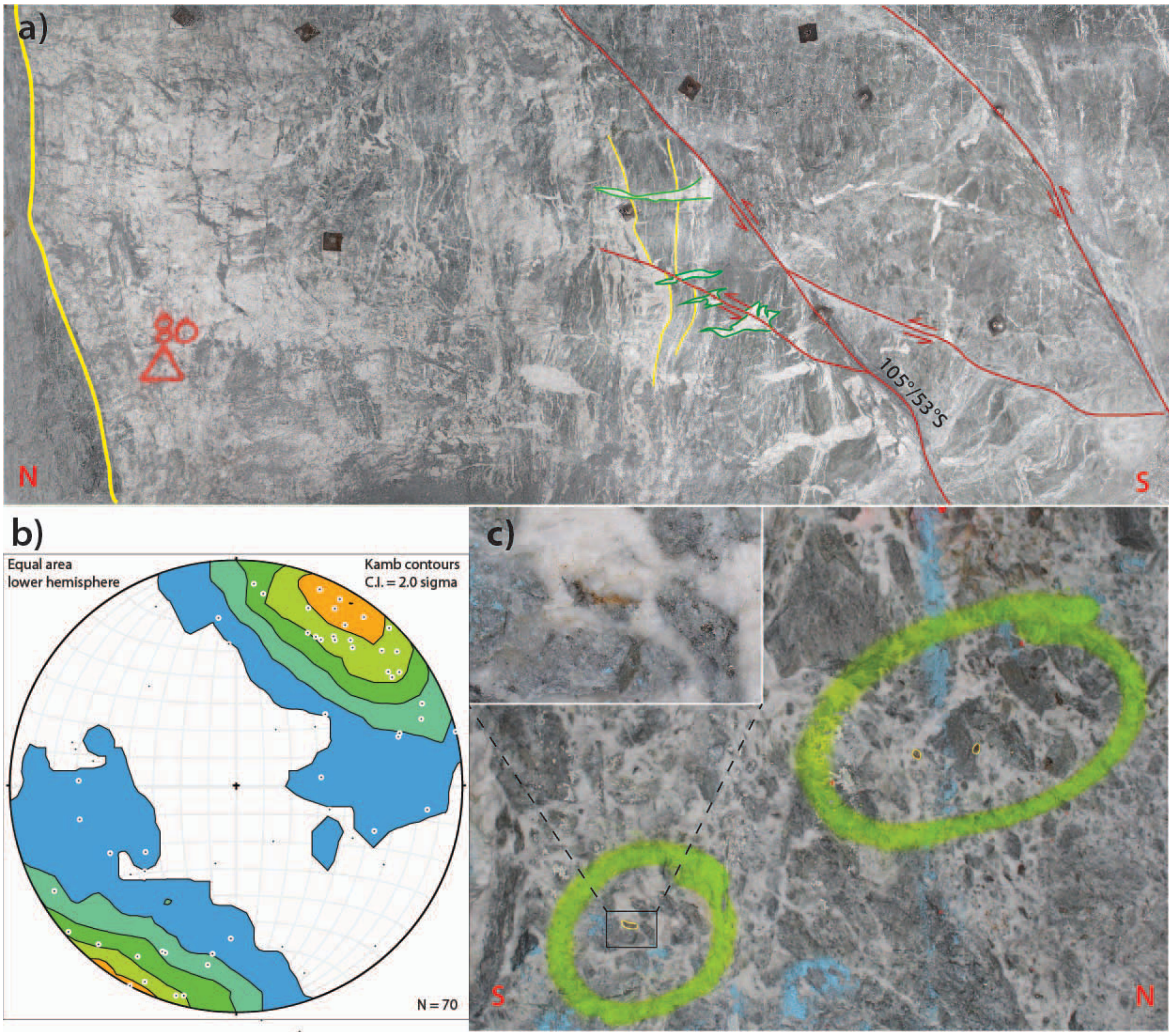

Figure 3.4 Photographs and measurements of stockwork exposure in the underground workings at the Brucejack. a) Domain 20 exposure in the east wall of a cross-cut. View of vertical wall is approximately 8 m wide and faces east. Yellow lines indicate subvertical veining and the sharp northern contact of the core stockwork zone of Domain 20. Location of the subvertical veins highlighted in yellow on the south side shows where there is a transition from the core stockwork zone to less intense quartz-carbonate veining. Red lines show late faults with associated tension-gash veins that cross-cut subvertical veins highlighted in green. b) Equal-area stereonet projection showing poles to 71 veins. Kamb contour interval is 2σ. Measurements were taken from both the east and west walls of the photographed cross-cut, as well as both the east and west walls of another exposure up dip (85 m vertically above photo). c) Quartz-carbonate breccia along the north (footwall contact) of Domain 20. Small yellow circles indicate electrum-quartz vein fragments that form clasts in the breccia. The green circle in bottom left of photo is approximately 15 cm in diameter and the inset in the top left corner shows electrum within a clast of older grey quartz surrounded by younger white quartz that forms cement within the breccia. Electrum here is tarnished reddish-brown due to reaction between diesel exhaust emitted from underground mining equipment and Ag in the electrum.

3.1). Previous mapping shows that this outcrop belongs to a southeast-striking, steeply dipping, 10-15 m wide quartz-carbonate stockwork system that extends along strike for at least 50 m to the southeast and 250 m to the northwest. It also shows that it has en-echelon stockwork veining at low angles to the strike directly to the northwest of map area 2 (Figure 3.1). This system links with a layer of silicified conglomerate lenses, delineated by drillcore, that extend ~200 m down-dip (Jones, 2013) and are offset by south dipping thrust faults (Pretium Resources Inc, unpublished data, 2015). At surface, this stockwork veining is hosted within linked elongate outcrops of predominantly silicified conglomerate which form topographical highs whereas surrounding quartz-sericite-pyrite altered schist is eroded away. The vein intensity within these outcrops can be as high as 50% making most of the outcrop quartz-carbonate stockwork. However, as large distinguishable quartz-carbonate vein cross-cut earlier alteration and stockwork, these could be mapped individually.

Detailed vein mapping in Figure 3.5 shows up to 1 m wide quartz-carbonate veins that are mostly sub-parallel to the major stockwork zone mapped in Figure 3.1. However, large, tabular veins greater than 50 cm wide are much less common than in map area 1. Veins are commonly less than 10 cm and tend to be wider only at vein intersections. Mapped veins are more continuous along strike within the eastern portion of the outcrop than the west where many veins are less than a few metres long. These shorter veins occurred in an area with more intense silica alteration. Within the eastern portion of the outcrop, veins continuous for up to 10 m occur in subparallel sets forming linked networks. Very few predominantly carbonate veins were mapped, with 2 occurring in the northwestern part of the outcrop.

Unlike map area 1, the veins in map area 2 have features that indicate that many of them formed during shear-strain instead of extension. An increase in shear-related veining is consistent with a significantly larger number of through-going faults and associated veins that are mapped at this location. Textures that indicate formation during shear are stretched quartz fibres, breccias along veins and at vein intersections, and veins parallel to S-fabrics (Figure 3.6). Also, tension gashes filled with quartz occur within the hanging wall of mapped thrust

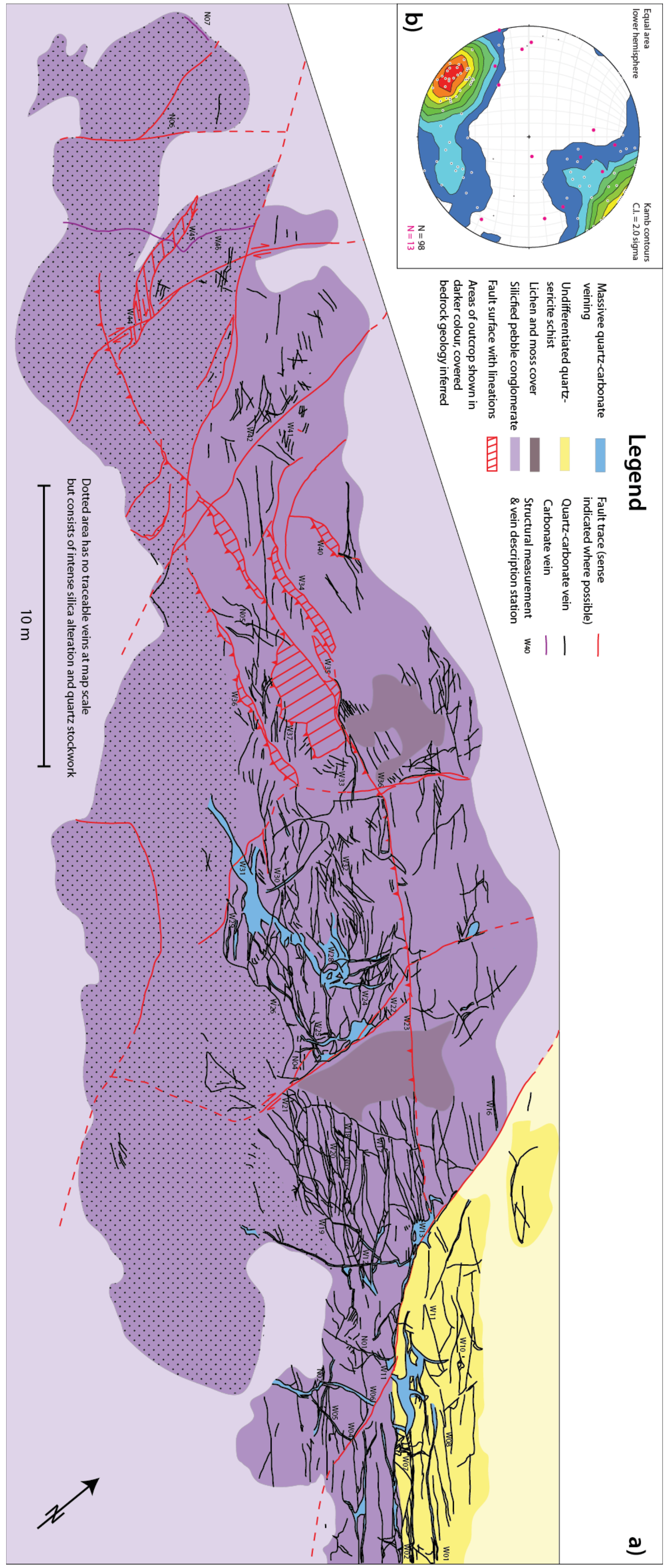

Figure 3.5 a) Lithology, stockwork quartz-carbonate veining and faults in map area 2 of the Brucejack Au-Ag deposit (see Figure 3.1 for locations). b) Equal-area projection of poles to vein (in black) and fault (in red) orientations measured at stations indicated in (a). Kamb contours indicate concentration of poles to vein orientations. See text for further description.

faults (Figure 3.5a, station W33), and weathered sheets of quartz occur on the southwest edge of the outcrop on surfaces that may be fault planes.

Several faults were mapped within map area 2. Dip-slip faults striking northwest with a moderate southeast dip were paired with steeper dipping conjugate back-thrusts (Figure 3.5a, station W35). Steeply dipping oblique-slip faults, with both sinistral (Figure 3.6b) and dextral (Figure 3.5a, station W21) sense, strike north. There does not appear to be a consistent offset of either the thrust or oblique slip faults at locations where they intersect. Several of these faults define the edges of outcrop within the northwest portion of the map area. In conjunction with brittle deformation highlighted by fault formation, several veins are also folded and buckled. Disharmonic folds with axial planes trending 310° are shown in Figure 3.6c. These are approximately perpendicular to trends of axial planes in map area 1.

Ninety-eight vein orientations and 13 fault plane orientations were taken at stations labelled on map area 2 (Figure 3.5a, b). Mapping and equal-area stereonet projection show that there is a predominant set of of northwest striking veins dipping steeply southwest to moderately northeast. There is also a subordinate set of northeast striking veins dipping moderate to steeply southeast. Fault orientations coincide with moderately northeast dipping northwest striking veins. Steeper faults are north-northwest striking and do not seem to correlate with a significant concentration of vein orientations. This data shows that there is a substantial portion of the mapped veins that do not directly coincide with mapped faults.

Lithological mapping, as in map area 1, is made difficult by pervasive quartz-sericite-pyrite alteration. In the case of map area 2, this alteration was more intense and only two different lithological units were described (Figure 3.5a). Silicified, clast-supported, pebble conglomerate makes up much of the outcrop area, including all areas with significant topographical prominence. To the north-northeast lies undifferentiated quartz-sericite-pyrite schist. Fibrous quartz (Figure 3.6a) and truncated veins (figure 3.5a) indicate that the contact between these two units is a fault. Drillcore from this region shows that silicified conglomerates are bounded by rocks with extreme sericitic alteration (Pretium Resources Inc. unpublished data 2015)

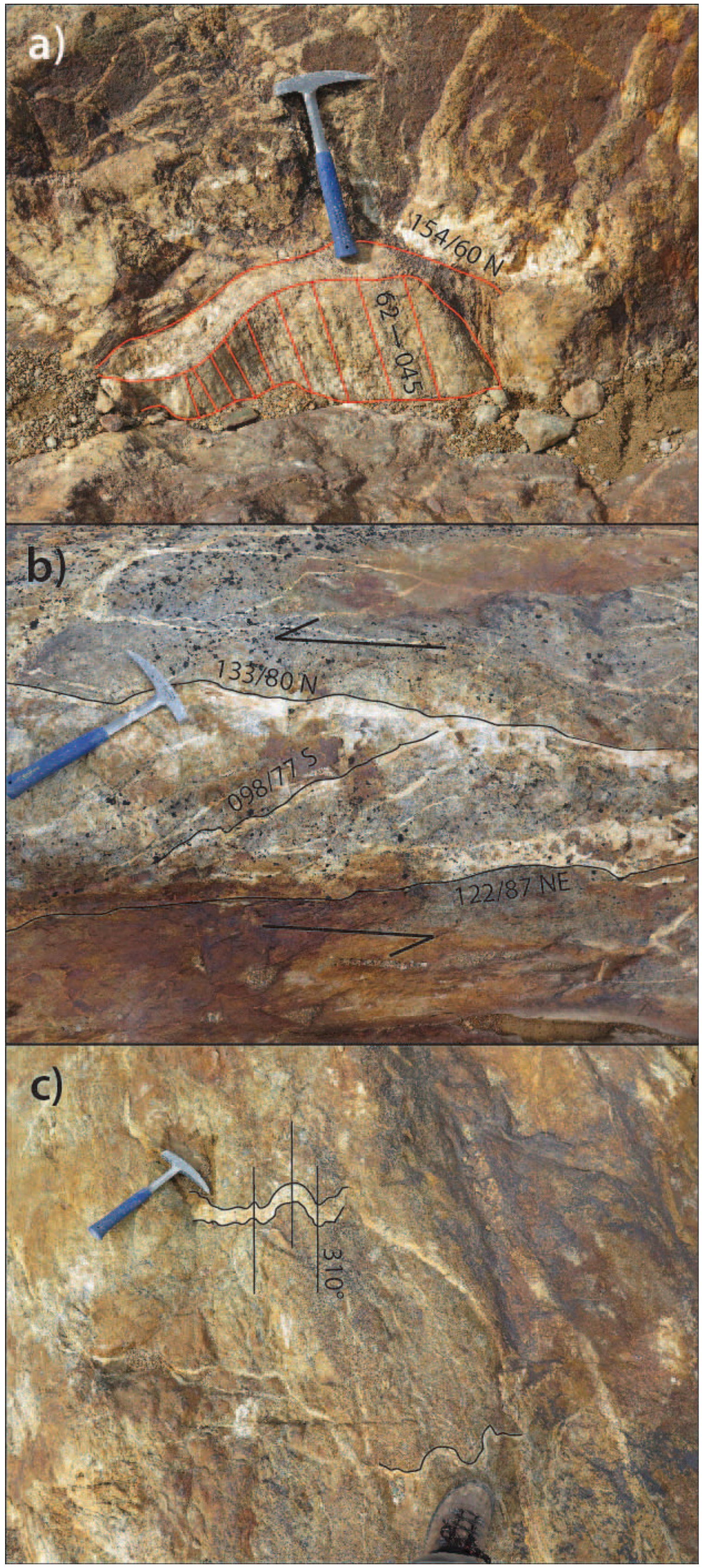

Figure 3.6 a) Fibrous quartz vein within fault with quartz lineations oriented close to dip-direction of fault plane. Rock hammer for scale. b) Quartz-carbonate veins and vein breccia along fault planes as well as S-fabric between fault planes. Fault sense is sinistral. Rock hammer for scale. c) Disharmonic folding of quartz-carbonate veins. The axial planes of the folds trend approximately 310°. Rock hammer for scale.

which tends to crop out poorly on surface due to preferential erosion.

3.1.1 Electrum mineralization

Electrum mineralization is not observed in outcrop due to weathering and gossan formation on the surface. However, it can be seen in multiple locations underground (Figures 3.4-3.10). In some cases, electrum-bearing veins were brecciated and original vein geometries were destroyed. Other electrum-bearing veins are intact and preserve their primary structural context. Below, I review some of the specific settings in which large (visible >4 mm) accumulations of electrum were found in clean exposures in the underground workings of the Brucejack mine.

Figures 3.4-3.11 show photos of electrum in specific settings. Figures 3.4c and Figure 3.7a show electrum located within or very proximal to large quartz-carbonate stockwork zones. Here electrum can be present in reworked quartz-carbonate vein clasts within vein stockwork or co-deposited within a primary vein phase. Electrum is also present in more continuous veins and sheeted veins that are not part of large intense stockwork zones (Figures 3.7b-3.10). These veins do not contain brecciated clasts of electrum-bearing veins, but rather electrum is always co-deposited within a primary vein phase.

Electrum can be cross-cut by later syntaxial quartz veins or vein phases (Figure 3.8), indicating that vein formation continued for some time after some electrum precipitation or deposition. At most locations where electrum has been deposited in situ within the vein, a thin layer (1-3 mm) of comb quartz forms a mostly continuous barrier between the wallrock and the mineralization. Where electrum is in contact with wallrock, electrum-bearing quartz-carbonate veins usually cross-cut older pyrite veins or blebs within the wallrock (Figure 3.9). Visible electrum texture is usually dendritic but can be flattened into vein foliation, especially when the host vein contains sericite selvages (Figure 3.10).

Along with sericite, electrum-bearing quartz-carbonate veins also contain pyrite and in places, base metal sulphides such as galena, sphalerite, chalcopyrite and Ag sulphosalts. Veins with significant base-metal sulphide mineralization (vein 2) are visible underground and can

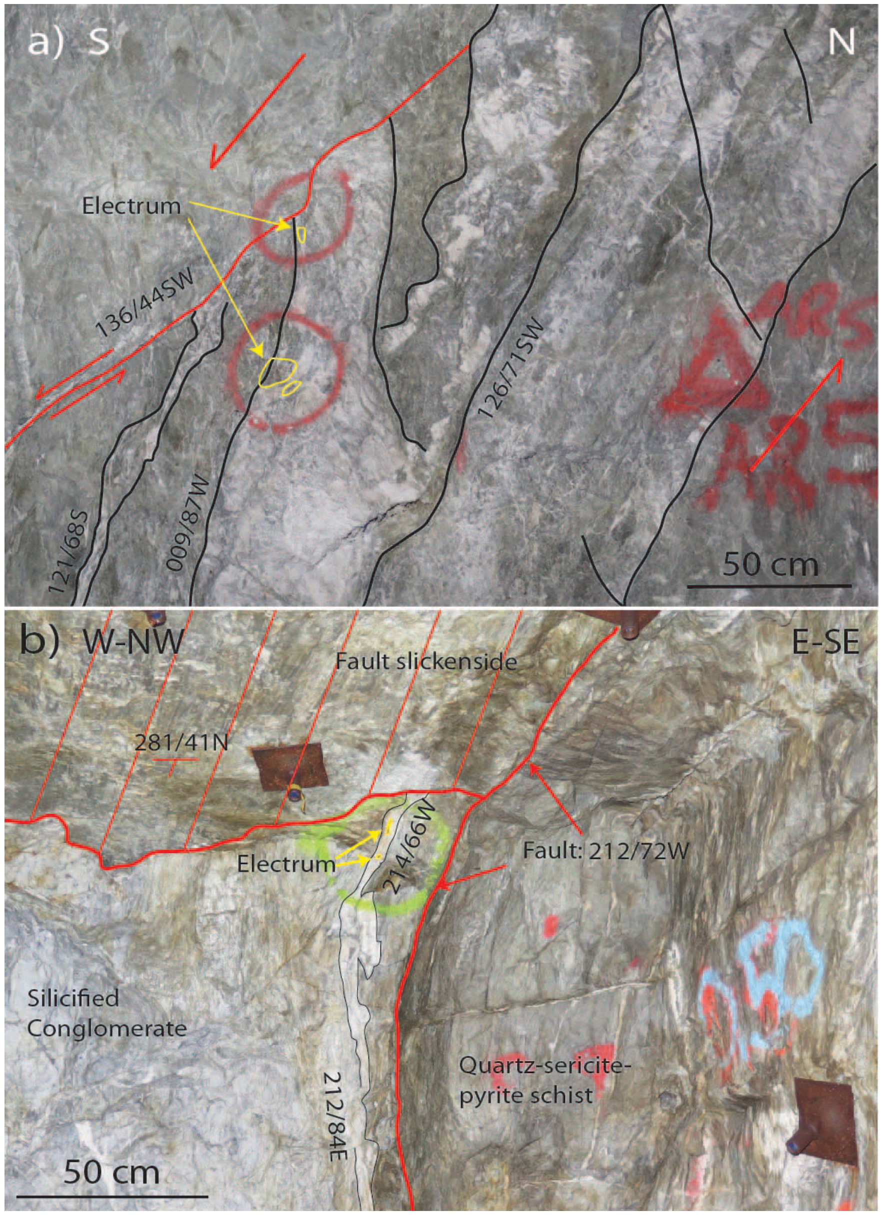

Figure 3.7 a) Photograph of 1.7 m wide electrum-bearing quartz-carbonate vein stockwork exposure within Domain 20. View faces to the west. Electrum bearing grey quartz (highlighted in yellow) is cut by later milky white quartz-carbonate veining and breccia. Electrum was observed to be contained within grey quartz clasts. Several phases of brecciation are exposed and highlighted with black outline. Red line indicates fault with apparent normal motion as indicated by S-fabric with orientation of 310°/86°S. Normal motion on Domain 20 stockwork zone is inferred. b) Photograph of electrum-bearing quartz-carbonate vein and fault exposure. Sample of electrum labelled in photo is seen in thin section in Figure 3.16b, d, e, f and Figure 3.22. Photo looks N-NE. Electrum bearing vein is banded, contains base metal sulphides and is located at the edge of, and cuts, silicified conglomerate. It is subparallel to a steep fault with approximately 2 m apparent dextral offset. Slicken-lineations plunge 61° indicating dip-slip motion of approximately 4.1 m. Fault indicated at top of photo forms roof of underground drift at this location. Thrust motion is inferred from slicken-surface texture and nearby thrust faults visible in the underground workings with similar orientation. Slicken-lineations are parallel to fault slicken-surface dip. Electrum bearing vein either cross-cuts or is parallel to wallrock foliation of 184/85E.

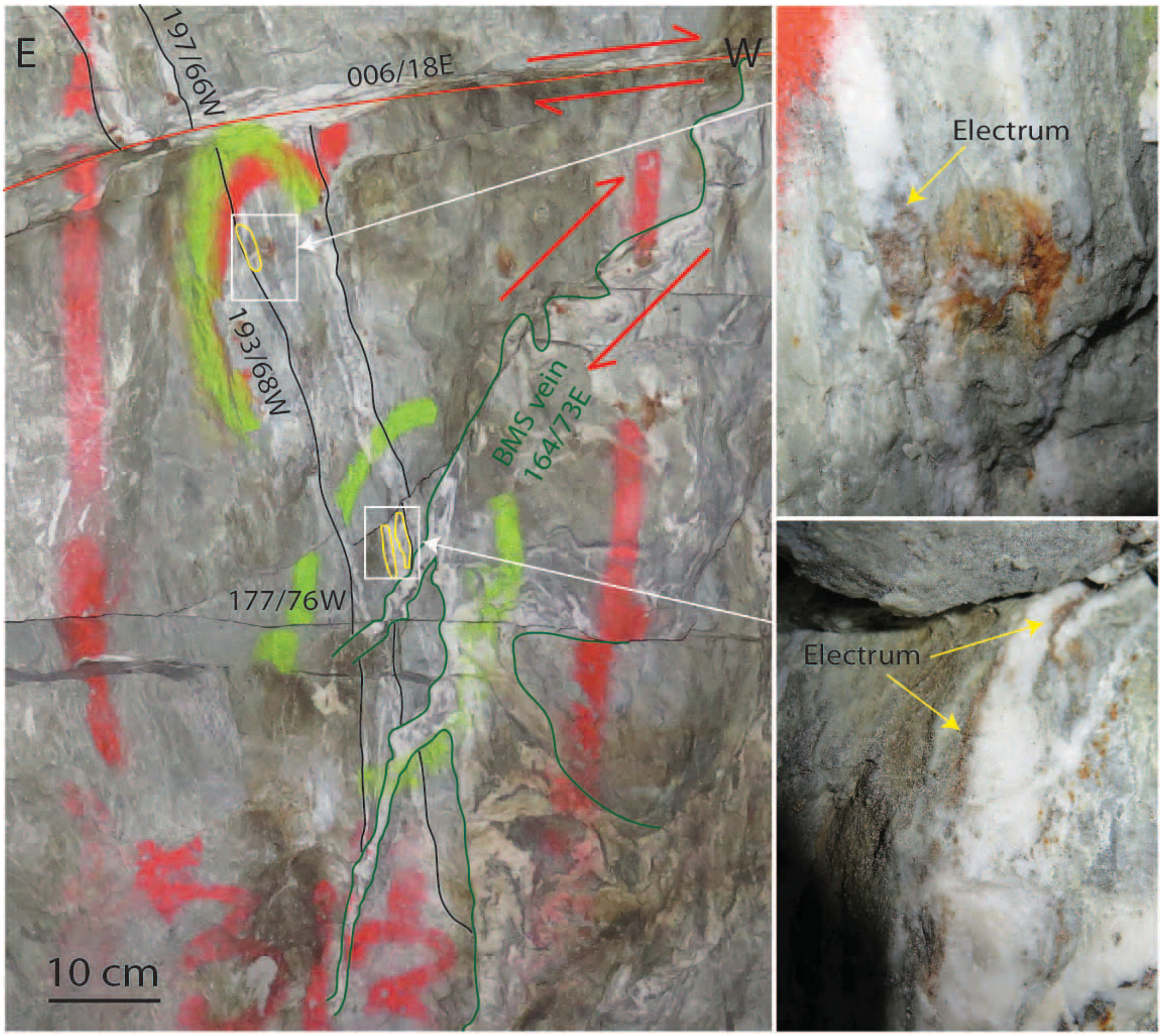

Figure 3.8 Photograph of electrum-bearing quartz-carbonate vein exposure. Photo looks to the south and shows 10 cm wide banded vein with electrum mineralization highlighted in yellow. This banded vein is cross-cut by base metal sulphide (BMS) bearing quartz-carbonate stockwork with west and up-dip verging folds which in turn is cross-cut by a shallowly dipping fault with apparent dextral motion. Insets show electrum mineralization in detail. Top inset shows denditritic electrum in centre of vein with 2-3 mm of comb quartz between wallrock and electrum. Bottom inset shows electrum separated from wallrock by 2-3 mm of comb quartz as well as a quartz-carbonate in the centre of the vein.

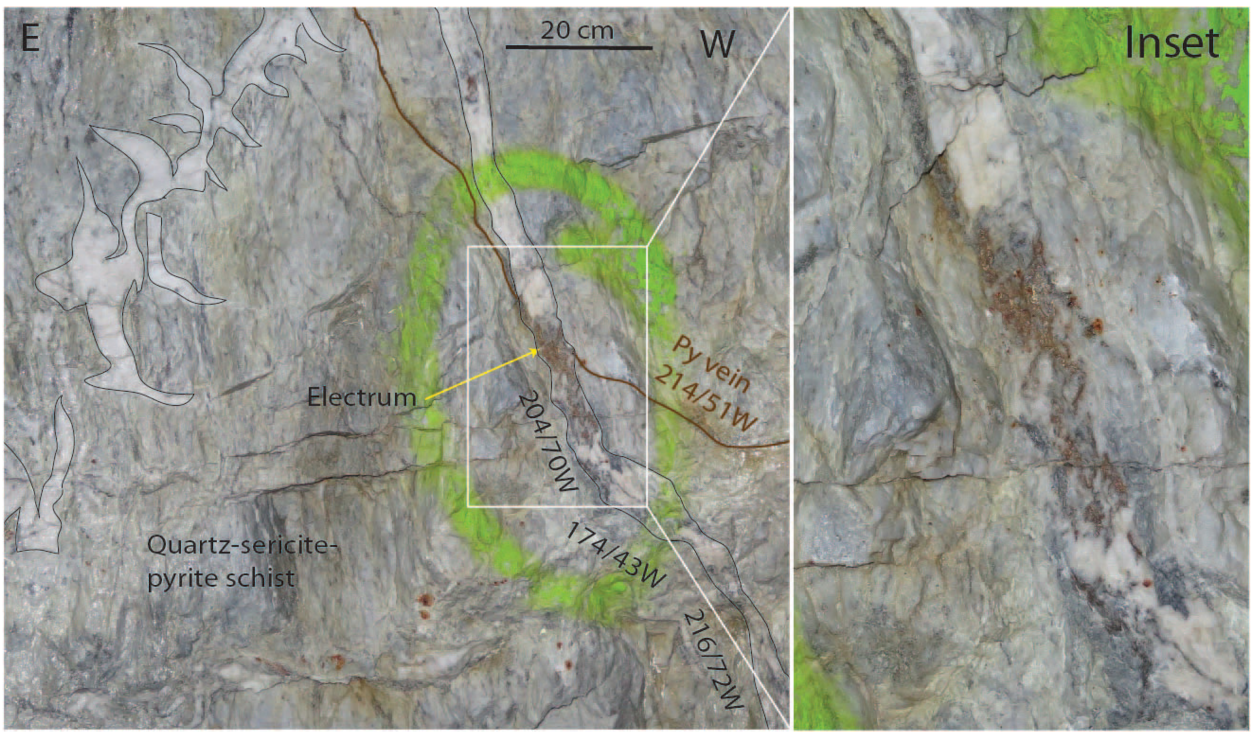

Figure 3.9 Photograph of electrum-bearing quartz-carbonate vein exposure. Photo looks towards south. 5-10 cm wide electrum bearing quartz-carbonate vein is shown at various orientations. Where this vein cross-cuts an earlier pyrite vein (vein 0) there is significant electrum. A fracture defined by en-echelon sigmoidal quartz veins cross-cut both the electrum bearing quartz-carbonate vein and the pyrite vein further up the wall. Inset shows detail of dendritic electrum mineralization within quartz-carbonate vein.

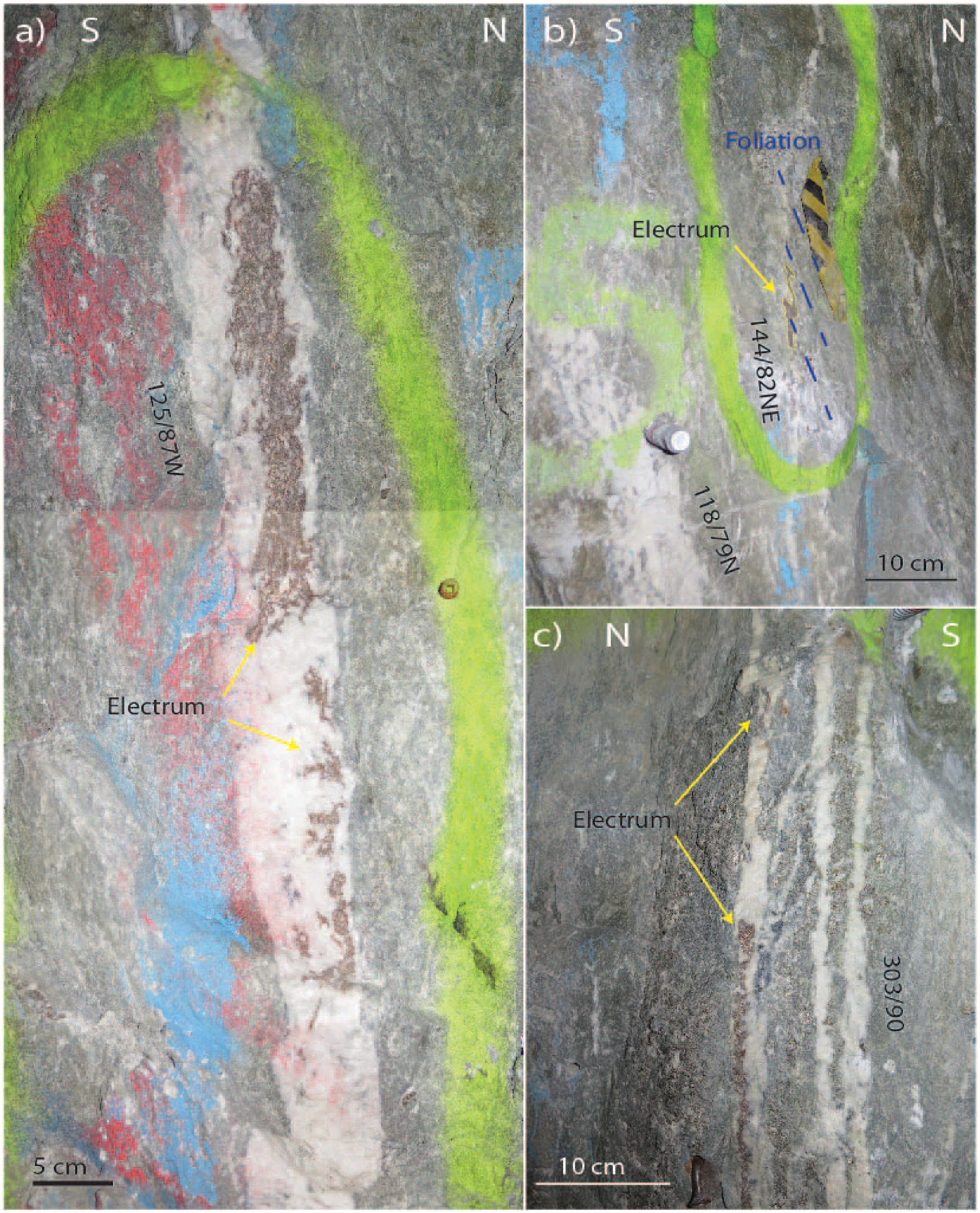

Figure 3.10 Photographs of electrum-bearing quartz-carbonate vein exposure. a) 5 cm wide quartz-carbonate vein with significant electrum mineralization. 2-3 mm of quartz-carbonate separates wallrock from dendritic electrum with interstitial quartz-carbonate. View is to the west. b) Electrum mineralization in 1-2 cm wide vein that is cross-cut by a larger quartz-carbonate vein at bottom of photo. Electrum is folded and is flattened into the foliation. Note comb quartz growth between wallrock and mineralization. This vein is part of a set of 0.25-1 m spaced 1-5 cm wide quartz-carbonate veins trending 120°-140°. View is to the west. c) Photograph of vertical, sheeted 10 cm wide electrum-bearing quartz-carbonate vein. Electrum mineralization is concentrated on the north side of the vein with 1-2 mm of comb quartz between wallrock and electrum. The wallrock and vein selvages contain significant pyrite mineralization. View is to the east.

be tabular and continuous over tens of metres. If electrum is present within these veins, it tends to have a more silvery lustre than electrum bearing veins with little or no base-metal sulphide mineralization. As noted by previous workers (Board and McNaughton, 2013; Jones, 2013; Tombe, 2015), these base-metal sulphide veins cross-cut veins containing darker, more golden electrum (Figure 3.8).

Mineralized vein phases have been deformed by later faulting and folding. Quartz-carbonate veins and stockwork are cut by later vein breccia (Figure 3.7a) and planar faults (Figures 3.4, 3.7b, and 3.8). Deformation of veins affected electrum textures by flattening dendritic electrum into foliation of folded veins (Figure 3.10b). Wider, more continuous and planar base-metal sulphide veins still exhibit folding, which in one case is congruous with apparent motion on cross-cutting faults (Figure 3.8). Electrum also occurs within fault gouge and in one spectacular case, forms lineations on a fault slicken-surfaces. Here, sinistral dip-slip motion has been accommodated along a N-S fault that formed along a very high-grade, electrum-bearing manganoan calcite-quartz vein (vein 3, Figure 3.11).

Eleven orientations of visible primary electrum-bearing quartz-carbonate veins were measured in the underground workings of the Brucejack deposit (Figure 3.12). Six of these strike west-northwest with a steep dip either to the northeast or southwest. These orientations fit well with the veins measured in map area 2 (Figure 3.5b), as well as with those measured at exposures of domain 20 in the underground workings of the Brucejack deposit (Figure 3.4b). Four of the veins strike north-northeast and dip steeply to the northwest (one exception dipped very steeply to the east). These orientations could correlate with the subset of steeply dipping north trending veins described in map area 1 (Figure 3.2b) or a small subset of northwest dipping veins observed in map area 2 (Figure 3.5b). The remaining electrum-bearing quartz-carbonate vein measured was vertical and strikes towards 78°. The number of orientations measured is not sufficient to provide a meaningful statistical evaluation, however, they are similar in that they all dip very steeply.

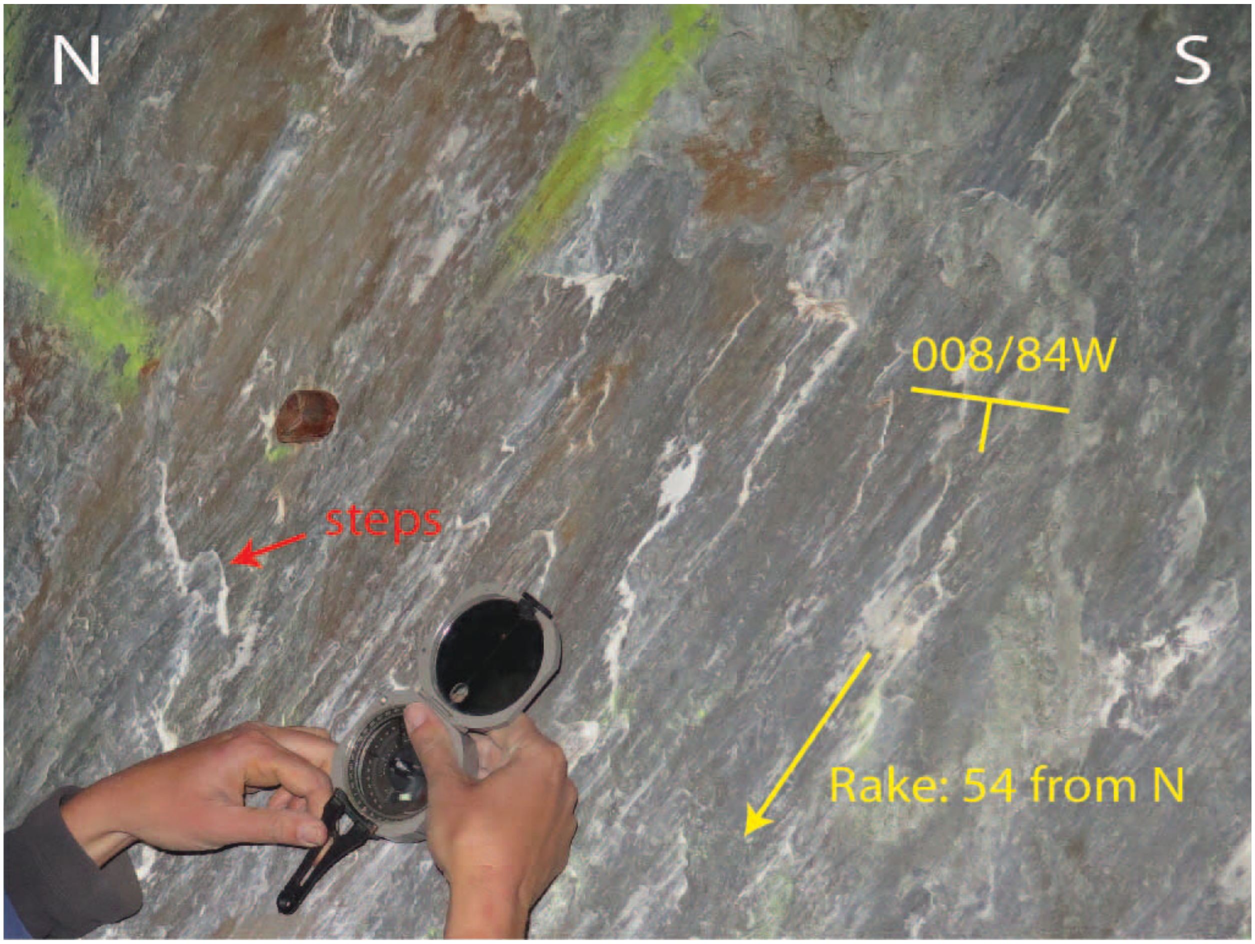

Figure 3.11 Photograph of electrum smeared slicken-line exposure in the underground workings at Brucejack. This fault has formed along a pre-existing carbonate-quartz vein with extremely high-grade electrum mineralization. Lineations and step kinematic indicators indicate sinistral-east side down dip-slip motion. View is to the east and Brunton compass for scale.

3.2 Optical microscopy

Quartz-carbonate veins and vein stockwork systems were analyzed in thin section in order to try and establish any micro-scale characteristics that set apart mineralized veins from barren veins. I describe quartz phases in the stockwork veining at Brucejack in order to test whether quartz may have recrystallized from an amorphous phase, and whether this is related to electrum mineralization. Samples from Brucejack were cut into small blocks at McGill University and sent to Wagner Petrographic in Linden, Utah, USA or Vancouver Petrographic in Langley, British Columbia, Canada for thin section preparation.

Quartz textures are widely varied but observations show quartz can be grouped into 5

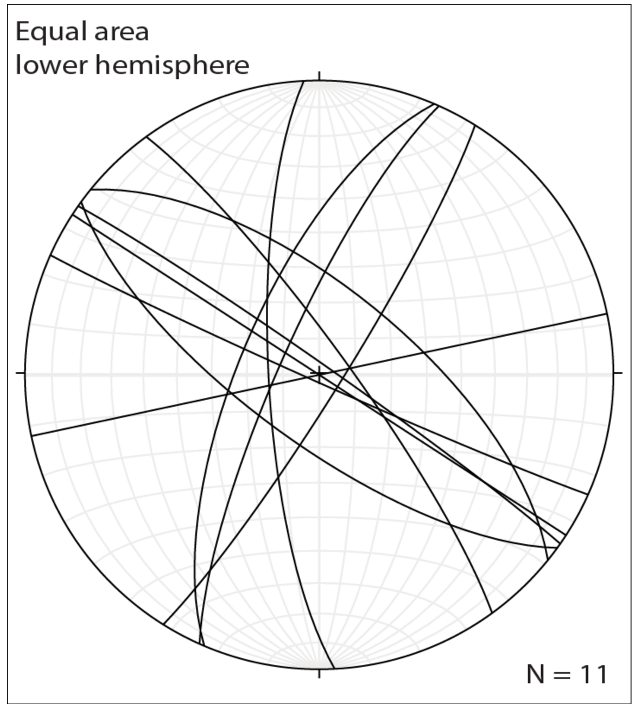

Figure 3.12 Equal-area stereonet projection of visible electrum bearing quartz-carbonate veins which outcrop in the underground workings of the Brucejack deposit.

different categories (Table 3.1). Vein types 1 and 2 contain four of these quartz types (phases A-D) while those veins related directly to later fault formation (veins 4 and 5) have their own distinct quartz textures (phase E). Quartz within predominantly carbonate vein 3s was not described here due to the relative rarity of this vein type and the lack of samples containing quartz.

Coarse grained quartz ($\sim$ 1 mm) within veins 1 and 2 either occurs as phase A or B (Table 3.1). Phase A quartz shows typical comb textures (e.g., Dong et al., 1995) with quartz nucleation and growth outwards from both wall rock and breccia clasts (Figure 3.13). Both the wall rock and the breccia clasts have undergone significant silicification providing a favourable nucleation point for quartz (formation of syntaxial or epitaxial veins) (e.g., Okamoto et al., 2010; Bons et al., 2012). With distance away from the nucleation point (e.g., wallrock or clast interface) the quartz grain size increases, known as an elongate-blocky texture (e.g., Bons et al., 2012). Within vein 1 breccia phases, it is common to see bladed phase A quartz crystals that have a euhedral termination at a common distance away from the wallrock. After this common distance, space has been filled with very fine grained silica (phase C),

Quartz type	Description	Vein occurrence	Figure
Phase A	Coarse grained, bladed, and euhedral and contain euhedral growth zonation marked by inlcusions	Veins 1 and 2	Figures 3.13, 3.15bcd
Phase B	Coarse, blocky and anhedral to euhedral and contain euhedral growth zonation marked by inlcusions	Veins 1 and 2	Figures 3.13abd and 3.15ac, and 3.14abc
Phase C	Very fine grained, subhedral, and cherty and associated with fine grained calcite and sericite	Veins 1 and 2	Figures 3.15d, and 3.14d
Phase D	Electrum related, fine grained, anhedral with lower inclusion density than surrounding quartz	Veins 1 and 2	Figure 3.16
Phase E	Elongate ribbons and major fractures with chlorite and sericite	Veins 4 and 5	Figure 3.17

Table 3.1 Description of different quartz textures observed using optical microscopy at Brucejack

calcite and sericite, or in some cases large anhedral quartz (phase B). Within larger vein 1 and vein 2 phases, obvious vugs are not present and several-mm sized blocky quartz crystals dominate (phase B). Commonly, there is intergranular calcite, fine grained quartz (silica), and minor sericite between between phase A and B quartz (Figure 3.14c). Phase B quartz occurs in larger bull quartz veins and is typified by a blocky geometry, and subhedral to euhedral grain boundaries. A major difference between this phase and phase A is the lack of an obvious nucleation point for crystal growth. Within blocky quartz, grain boundaries may seem euhedral at millimetre scales but are convolute and wavy when examined at a higher magnification, similar to grain boundary migration textures described by Passchier and Trouw (2005).

Both phase A and B quartz have opaque or high birefringence inclusions that can occur in three types of arrays: hexagonal concentric arrays (Figure 3.15b, c, d), linear arrays that can cross several grain boundaries that may represent healed fractures (Figure 3.15a, b d), or with sufficient density that only a preferential alignment of their long axis can be discerned

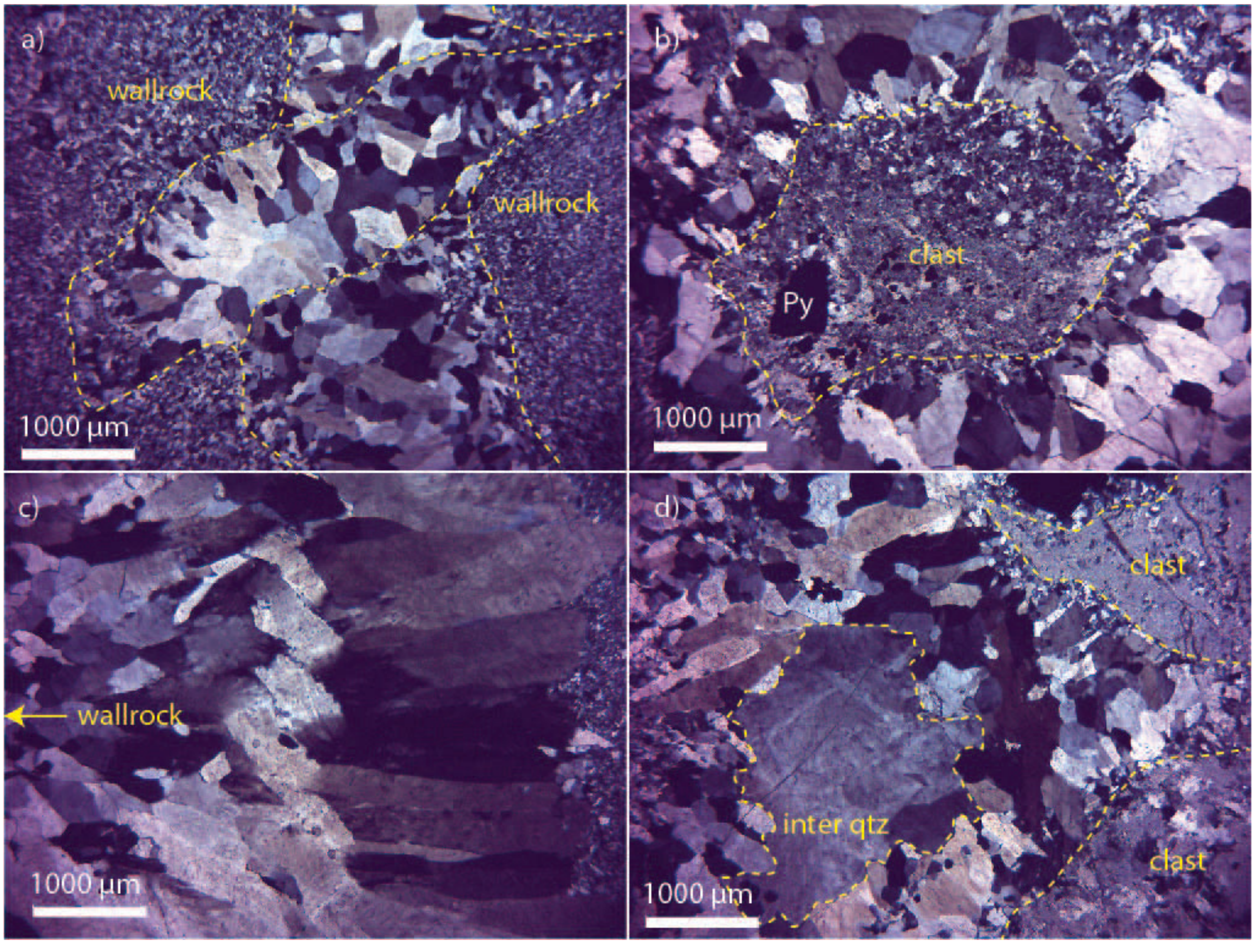

Figure 3.13 Photomicrographs of quartz-carbonate vein textures from vein 1 and vein 2. All photos are in XPL. a) Cross-cutting quartz-carbonate veins showing elongate-blocky syntaxial quartz texture (phase A) with growth nucleated on vein walls and progressing towards centre of vein. Wallrock is completely silicified. b) Quartz-sericite-pyrite altered clast surrounded by radiating quartz growth (phase A). c) Phase A comb quartz texture with increasing quartz grain size away from nucleation site (left). Large elongate-blocky quartz crystals with euhedral termination at right, where what may have been open space now contains fine grained quartz+calcite+sericite+pyrite (phase C). d) Large anhedral quartz with hexagonal banding and irregular extinction pattern is shown to occupy space between quartz growing radially from different clasts.

(Figure 3.15b). In some cases they can show increased density within a euhedral core of the crystal with the outer regions (overgrowths) relatively lacking inclusions or vice versa. Inclusions within the hexagonal bands can become sufficiently dense that they coalesce into a single patch of calcite or sericite. These hexagonal arrays are cut by grain boundaries. Figure 3.15a, b shows annealed quartz veins with a distinctly different density of inclusions cut across many crystals within thin section samples. These veins have the same extinction as the quartz grains they cross-cut. They are not perfectly linear and occur in arrays at 2 or

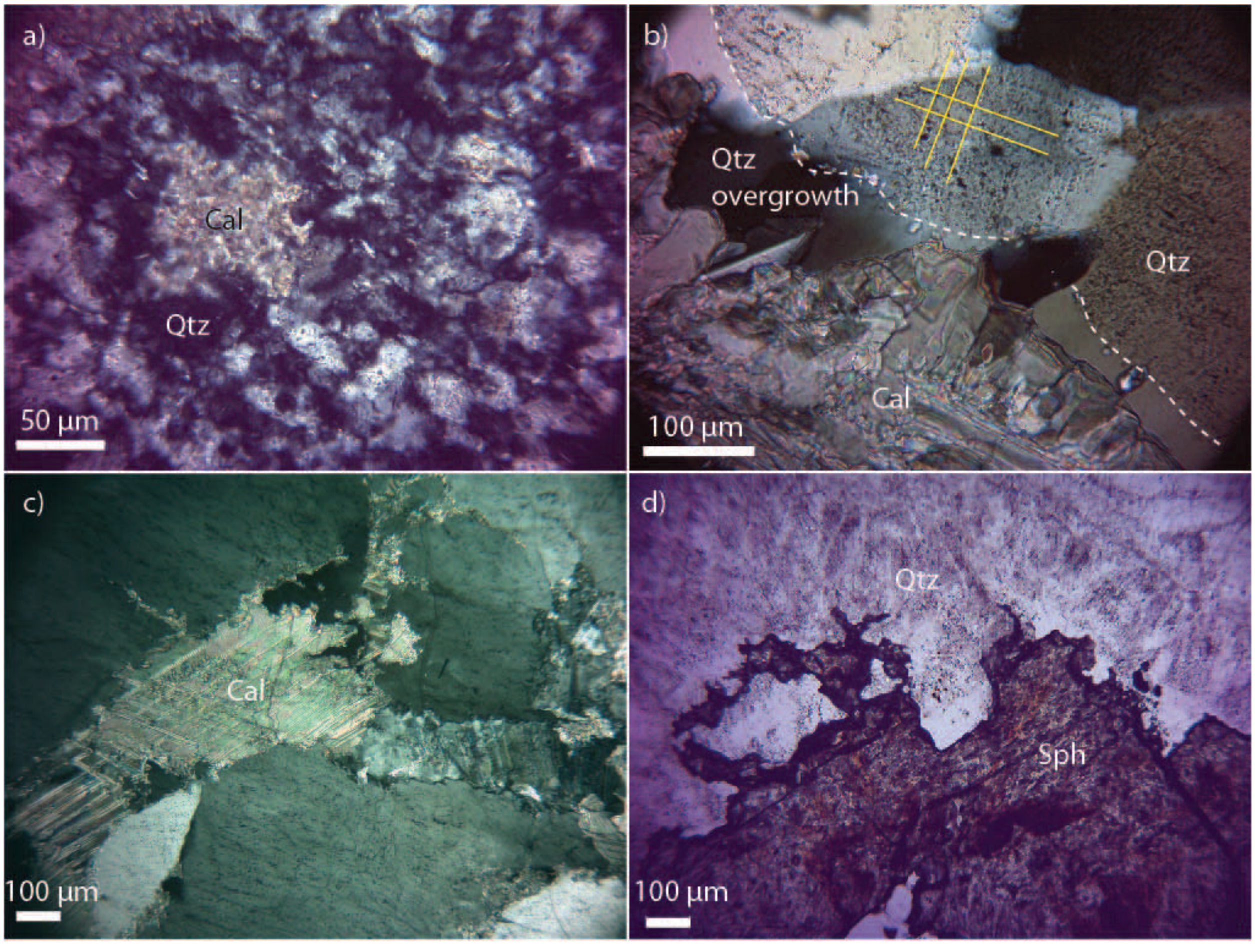

Figure 3.14 Photomicrographs of quartz-carbonate vein textures from vein 1 and vein 2. All photos in XPL. a) Phase C, fine grained quartz (Qtz) + calcite (Cal) with minor sericite within a dilational jog (see text for detailed description). b) Grain boundary between quartz and calcite. Quartz replacement of calcite is delineated by inclusion density boundary. Inclusions within quartz grains show similar geometry to calcite twinning. c) Interstitial calcite and quartz between coarse quartz grains (phase A and B). Calcite shows a highly tortuous grain boundary with quartz and its growth penetrates into the larger quartz grains. Interstitial quartz has a complex extinction pattern and all grain boundaries are very irregular. d) Interstitial sphalerite (Sph) in the middle of a syntaxial quartz vein. The quartz at the grain boundary with sphalerite displays the same relative lack of inclusions that is seen at grain boundaries where quartz replaces calcite and may indicate quartz replacement of sphalerite.

3 regular orientations. The longer veins are wavy and have an irregular lager spacing than shorter more linear sets. Figure 3.14b, d show that grain boundaries between some quartz crystals are marked by areas with lower inclusion densities than the rest of the crystals. This occurs both at grain boundaries between two adjacent quartz crystals, or within quartz at the grain boundary with another mineral such as calcite or sphalerite.

Within coarse grained phase A and B quartz, various sizes and shapes of subgrains exist.

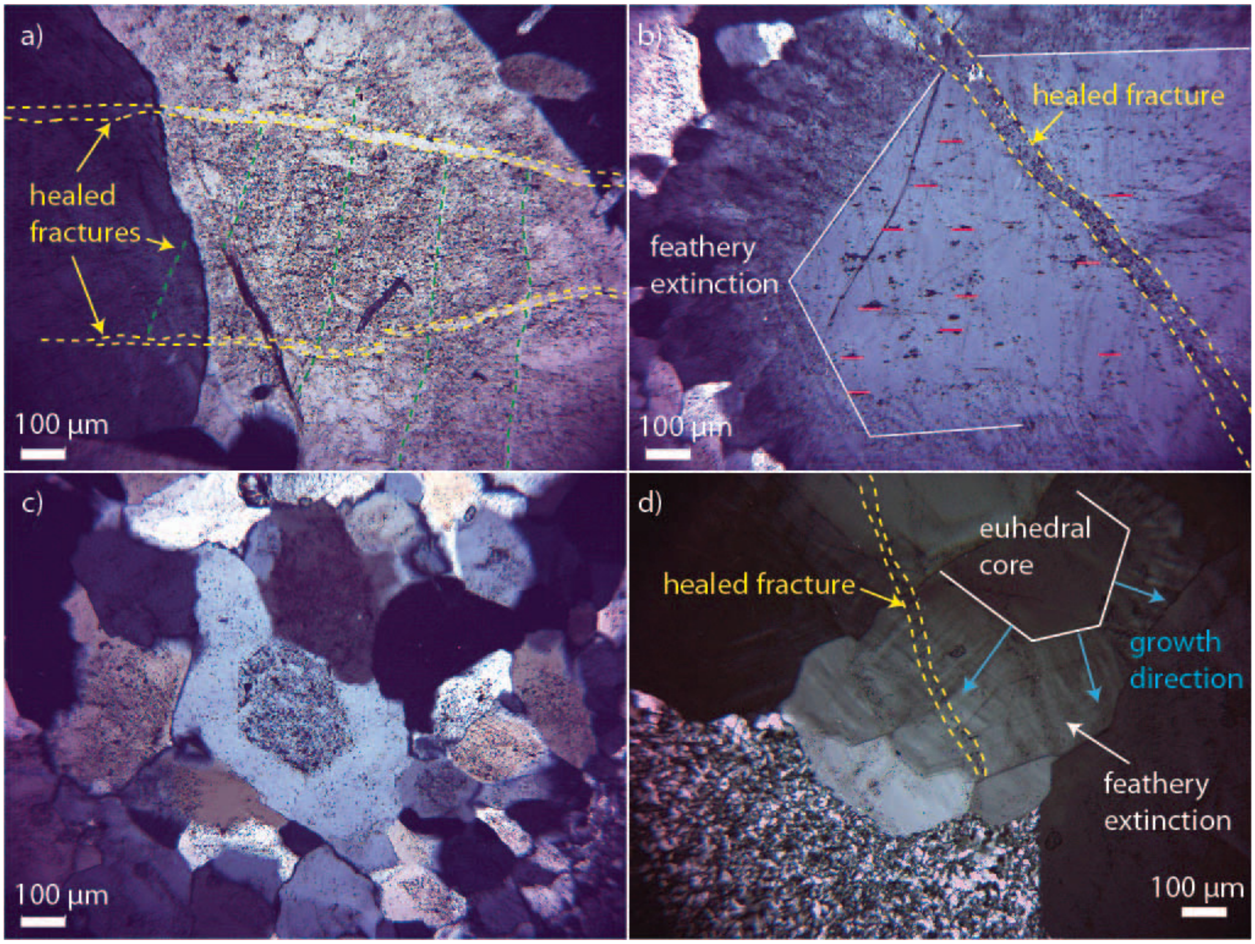

Figure 3.15 Photomicrographs of quartz-carbonate vein inclusion textures from vein 1 and vein 2. All photos in XPL. a) Quartz grain showing two sets of low inclusion density linear veins with same extinction as surrounding phase B quartz. b) Quartz grain with lower inclusion density euhedral core bounded by overgrowth on outer rim that has feathery extinction pattern and a higher inclusion density. Healed fractures with a higher inclusion density cross-cut the quartz grain from the top-middle to the bottom-right of the image. Solid inclusions within the centre euhedral core of the crystal show a fabric (marked in red). c) Blocky quartz grain (centre) with hexagonal high inclusion density core and lower inclusion density overgrowth on rim. d) Quartz grains with euhedral core defined by hexagonal inclusion array. Rims show feathery extinction. Transversing the grain boundary are healed fractures marked by linear bands of inclusions. Fine grained interstitial microcrystalline phase C quartz can be seen at the bottom-left of photo.

There a few exceptions where sharp euhedral smaller subgrains of quartz exist but the majority are subhedral to anhedral. Euhedral subgrains can be quite large ($\sim$100 μm) and appear in the centre of large phase A and B quartz crystals. Smaller subgrains can be elongate and radiate from hexagonal inclusion bands to form a feathery or flamboyant extinction textures (e.g., Okamoto et al., 2010) (Figure 3.15b, d). Others are irregular and form a texture similar to mosaic quartz and tend to be grouped on one particular side of a crystal. There are instances where a large number of subgrains are located at triple junctions between quartz grains (in two dimensions) along with interstitial fine-grained quartz or calcite+sericite (Figure 3.15d). Although subgrains commonly form during ductile deformation (e.g., Passchier and Trouw, 2005), their presence within the samples from Brucejack is not accompanied by other direct evidence of strain. This may indicate that they formed from another process (e.g., Dong et al., 1995).

Multiple veins and vein breccias have localities where vein phases consist of phase C, fine microcrystalline quartz+calcite+sericite+pyrite. This phase occurs commonly in the centre of veins where there is a dilational jog or where there is extra space in a vein breccia. This phase also occurs interstitially between quartz grains. Phase C shows distinctly different textural features than the coarse grained quartz (Figure 3.14d). Grain boundaries are difficult to distinguish in XPL and have high tortuousity, and the grains are 5 to 50 μm in diameter. There are numerous inclusions throughout the fine grained quartz without the regular hexagonal and linear patterns seen in some of the coarser grains. Inclusions overlap between grain boundaries suggesting that they predate the present quartz crystals. Within larger regions of microcrystalline quartz, larger anhedral quartz crystals with diameters ranging from 100-1000 μm in diameter are observed. Grain boundaries with surrounding very fine grained quartz are similarly tortuous. Fine subgrains with distinct extinction angles (but no grain boundary in plain polarized light) are visible within the middle of these larger anhedral grains. Like the finer grained quartz, numerous predominantly solid inclusions exist within these quartz grains whose distribution lack identifiable geometric patterns.

Figure 3.14(b, c, d) shows the interstitial spaces between larger phase A and B quartz. Interstitial space can be filled by phase C quartz, calcite, and sulphides such as sphalerite. The boundaries between quartz and the interstitial material are unique in that the quartz right at the boundary is devoid of, or contains a much lower concentration of inclusions. The boundaries between the quartz and the interstitial material are tortuous and in many cases show quartz penetration into the interstitial material (Figure 3.14b, d). However, in some cases where calcite is present in between quartz grains, it penetrates into larger quartz grains (Figure 3.14c). Where quartz growth has penetrated into calcite, inclusions within the larger quartz grains have a geometry that is similar to calcite twinning (Figure 3.14b) suggesting that quartz may have replaced calcite. Where inclusion-free quartz occurs near grain boundaries, later overgrowth of quartz into calcite may also have occurred. The textures described above show that both quartz and calcite replaced each other at different times, or in different locations, at Brucejack.

Electrum mineralization is observed to occur within vein 1, 2 and 3 types. Two thin sections with visible electrum mineralization were observed, both of which contained dendritic interstitial electrum within vein type 1 (Figure 3.16). Both samples contained significant amounts of calcite that occurs as inclusions within quartz and large (>1 mm) anhedral crystals that are usually proximal to electrum mineralization (Figure 3.16a). Calcite in both samples has an interstitial texture similar to phase C quartz+sericite+calcite seen in other samples. Pyrite is associated with some of the electrum mineralization in one sample where electrum occurs directly adjacent to or as inclusions within subhedral pyrite grains. Patches of sericite are observed alongside electrum but do not have the same consistent spatial correlation as calcite.

Two distinct types of quartz can be seen in the electrum-bearing quartz-carbonate vein samples. The first, which is usually peripheral to dendritic electrum, is coarser phase B quartz with rare phase A quartz, which are common in all observed vein 1 and 2 generations. The second quartz phase, which is observed to be only adjacent to dendritic electrum, is finer grained phase D quartz. Figure 3.16 shows that phase D quartz has tortuous grain boundaries that are non-distinct and extinction patterns that give it a mottled appearance under cross-polarized light. Variations in grain size correlate with the amount of interstitial electrum that is present. Areas with a greater amount of electrum have an increased quartz grain size (up to 200 μm) between the branching electrum networks compared to areas of less electrum (5-50 μm) (Figure 3.16c, d). Inclusion densities within phase D quartz vary and

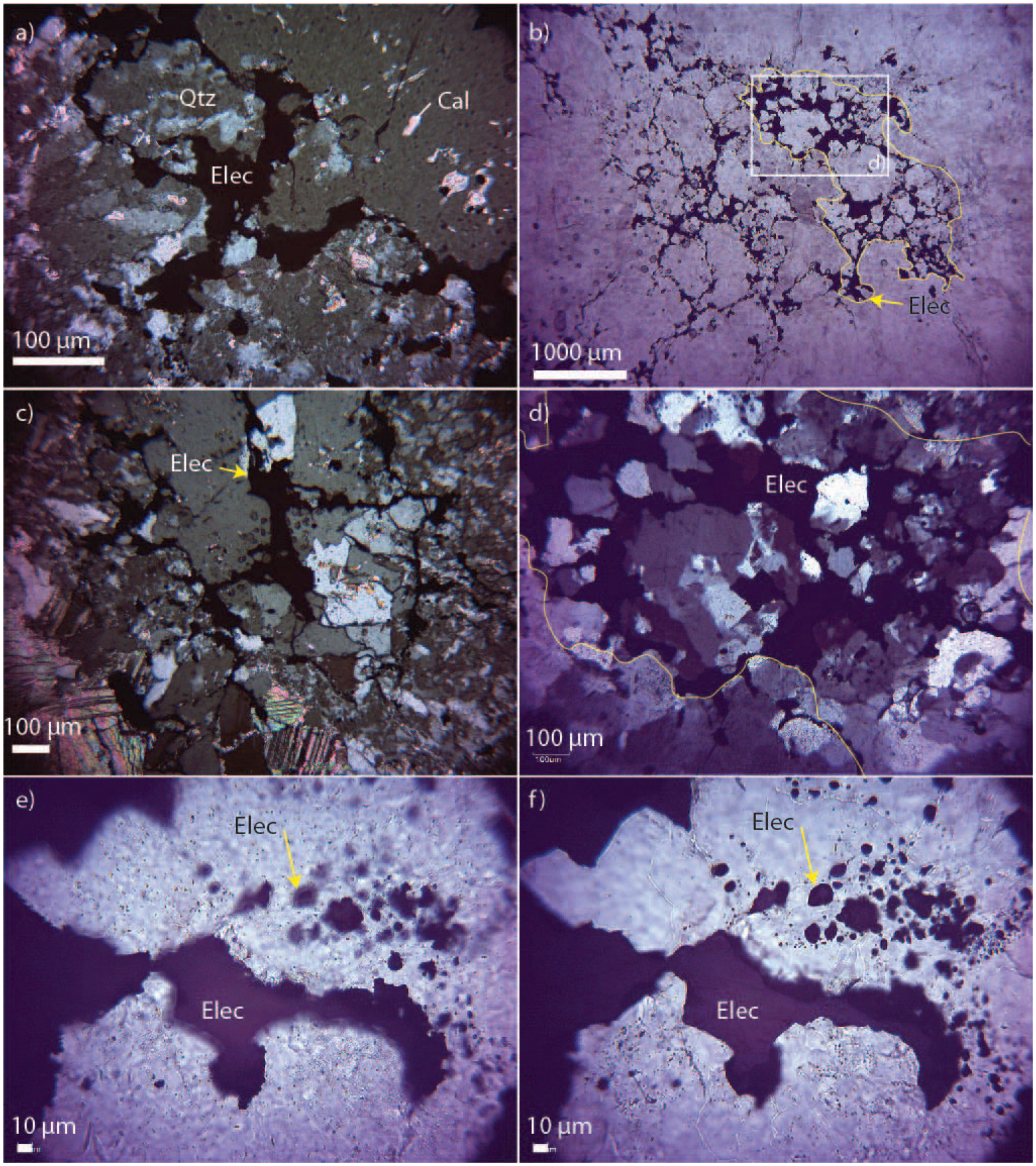

Figure 3.16 Photomicrographs of electrum-bearing quartz-carbonate veining (vein 1). a) Dendritic electrum (Elec) within fine grained, mosaic phase D quartz (Qtz) containing calcite (Cal) inclusions (XPL). b) Dendritic electrum within quartz-carbonate. Yellow line outlines an area of phase D quartz with lower inclusion density. White box indicates position of (d). This sample is taken from the labelled electrum in Figure 3.7b (PPL). c) Dendritic electrum with phase D quartz showing increase grain size and decreased inclusion abundance with proximity to abundant electrum mineralization (XPL). d) Inset shown in (b) showing lower inclusion density and phase D quartz textures (XPL). e) Tortuous electrum-quartz grain boundary with the front of the slide in focus. Small spherules of electrum are located just above and to the right of interstitial electrum. This sample is taken from the labelled electrum in Figure 3.7b (PPL). f) Same photo as (e) with back of slide in focus showing relatively straight grain boundaries. (PPL).

tend to be less abundant when in close approximation to electrum, especially within quartz between electrum branches. Where the mineralogy of inclusions was observed, they consist of sericite and calcite.

Grain boundaries between electrum and quartz have both very tortuous and relatively straight segments. Convolute boundaries display a tortuousity with an amplitude of 5-10 μm. Straight boundaries tend to mimic the grain boundaries of the surrounding grains which in most cases are quartz. These boundary textures can change with a change in focus of the microscope from the front to the back of a slide (Figure 3.16e, f). At a few locations proximal to the electrum grain boundary, small spherules of electrum with a diameter <15 μm are located within quartz (Figure 3.16e, f). Electrum within a wider array of vein types need to be examined before these features can be described as ubiquitous for all electrum mineralization at Brucejack, but these observations provide an example of textures associated with high-grade Au (electrum) within vein 1 phases.

Quartz-carbonate veins associated directly with faults (vein 4) display quartz textures indicative of strain (phase E). Both quartz crystals and their extinction patterns are elongate parallel to measured fault lineations. Where elongate quartz is observed, it is wavy and has progressive undulose extinction that gives it a ribbon texture (Figure 3.17a). However, the patterns are not consistent throughout a sample. Some areas have distinct ribbon quartz while other areas have a blocky texture with a much weaker fabric although most of the coarser grained quartz displays undulose extinction. Along the boundaries of larger quartz crystals there are small new grains and subgrains that resemble those formed by bulging recrystallization, a process of crystal plastic deformation between temperatures of ~250°-400°C (e.g., Poirier and Guillopé, 1979; Stipp et al., 2002; Passchier and Trouw, 2005). While inclusions are abundant in quartz in these samples, they do not form the same hexagonal arrays seen in the the vein 1 and 2 samples. However, there are cross-cutting veins with lower inclusion densities that cross-cut multiple grain boundaries and that are perpendicular to the elongate orientation of the ribbon quartz. Fault-related veins contain sericite and Fe-oxide

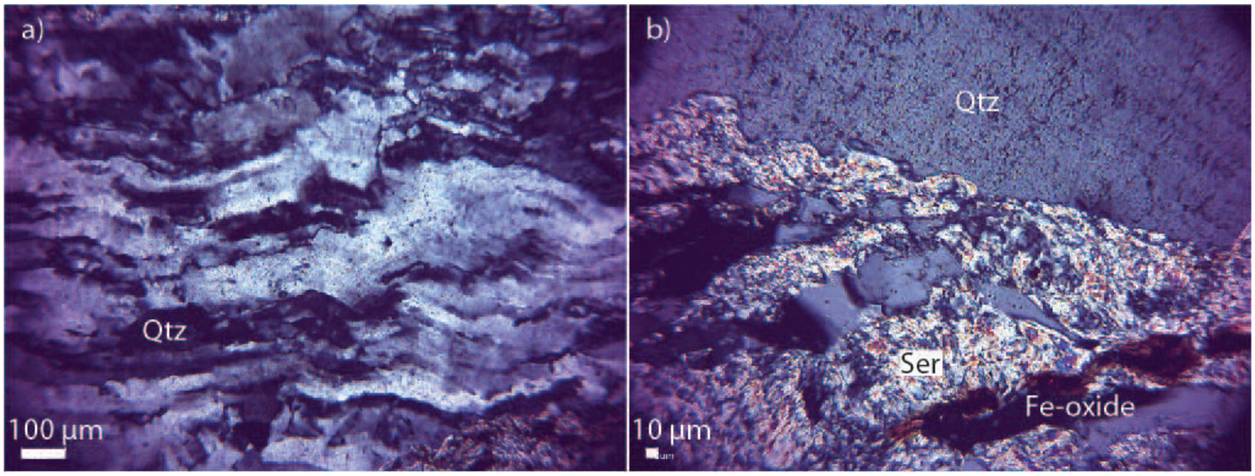

Figure 3.17 Photomicrographs of quartz (phase E) and sericite textures from fault related vein 4. a) Ribbon quartz (Qtz) elongate in direction parallel to fault lineation (XPL). b) Sericite (Ser) and Fe-oxide alteration with associated quartz showing low density of inclusions relative to adjacent large quartz crystal (XPL).

that is proximal to finer grained quartz. Quartz within sericite contains lower inclusion density than larger adjacent coarse-grained quartz (Figure 3.17b).

In summary, five different quartz phases (Table 3.1) are observed within the different vein types (Table 2.1) at the Brucejack deposit. Quartz phases A-C are present in vein types 1 and 2; however, quartz phase D is only seen in electrum bearing vein types 1 and 2. Quartz phase E is only seen in quartz-carbonate veins directly related to faulting (vein types 4 and 5). Observations of feathery extinction and microcrystalline aggregates of quartz (mosaic quartz) in all electrum bearing vein generations are indicators of recrystallization from an amorphous silica phase.

3.3 Electron microscopy

In order to examine samples from Brucejack in greater detail, several samples were analyzed using electron microscopy. Higher resolution than optical microscopy can be achieved because of the difference in wavelength between an electron beam and a beam of visible light. Whereas the visible spectrum has a wavelength between 380-750 nm, an electron beam has a wavelength, depending on accelerating voltage, of $\sim$ 0.0087-0.0037 nm (Williams and Carter, 1996). Observed precious metal nanoparticles are on the scale of 10's of nanometers (e.g., Reich et al., 2006; Hough et al., 2011; Scott et al., 2012), therefore a wavelength of the same scale is needed to observe them. Both scanning electron micrscopy (SEM) and transmission electron microscopy (TEM) were used to analyze surface textures and internal structure of quartz-carbonate vein samples.

SEM

To contrast different mineral phases within a sample, backscattered electron (BSE) images were obtained from a scanning electron microscope. These images show incident electrons that have been reflected, or backscattered, from a specimen. The fraction of electrons that are reflected back depends on the the atomic numbers of the atoms within the specimen. Thus, if a part of the sample has atoms with a higher atomic number then it will backscatter more electrons and appear brighter in the image (Lloyd, 1987). This makes BSE useful for imaging Au due to its high atomic number.

One thin section taken from exposed electrum bearing quartz-carbonate stockwork in the underground workings of Brucejack (Figure 3.7b and Figure 3.16b, d, e, f) and a thin section provided by Pretium Resources taken from drill core (Figure 3.16a , c) were used to make initial SEM observations on electrum textures. Observations were made on these samples using a FEI Inspect F-50 FE-SEM with EDAX Octane Super 60 mm^2 SDD and TEAM EDS Analysis system at the McGill Facility for Electron Microscopy Research (FEMR). This sample was also sent to Fibics Inc. in Ottawa, Canada, where a detailed back scattered electron image of the entire slide provided by Pretium was made at a resolution of 100 nm/pixel using a Carl Zeiss Sigma HD VP field emission SEM. Fibics Inc. took 1517 images and stitched them together using ZEISS Atlas 5 imaging software and uploaded the stitched photo onto a browser-based viewer. Higher resolution images of small subregions within this sample were also made at a resolution of 10 nm/pixel and included as links within the browser-based viewer in order to view sections of the sample at a higher resolution.

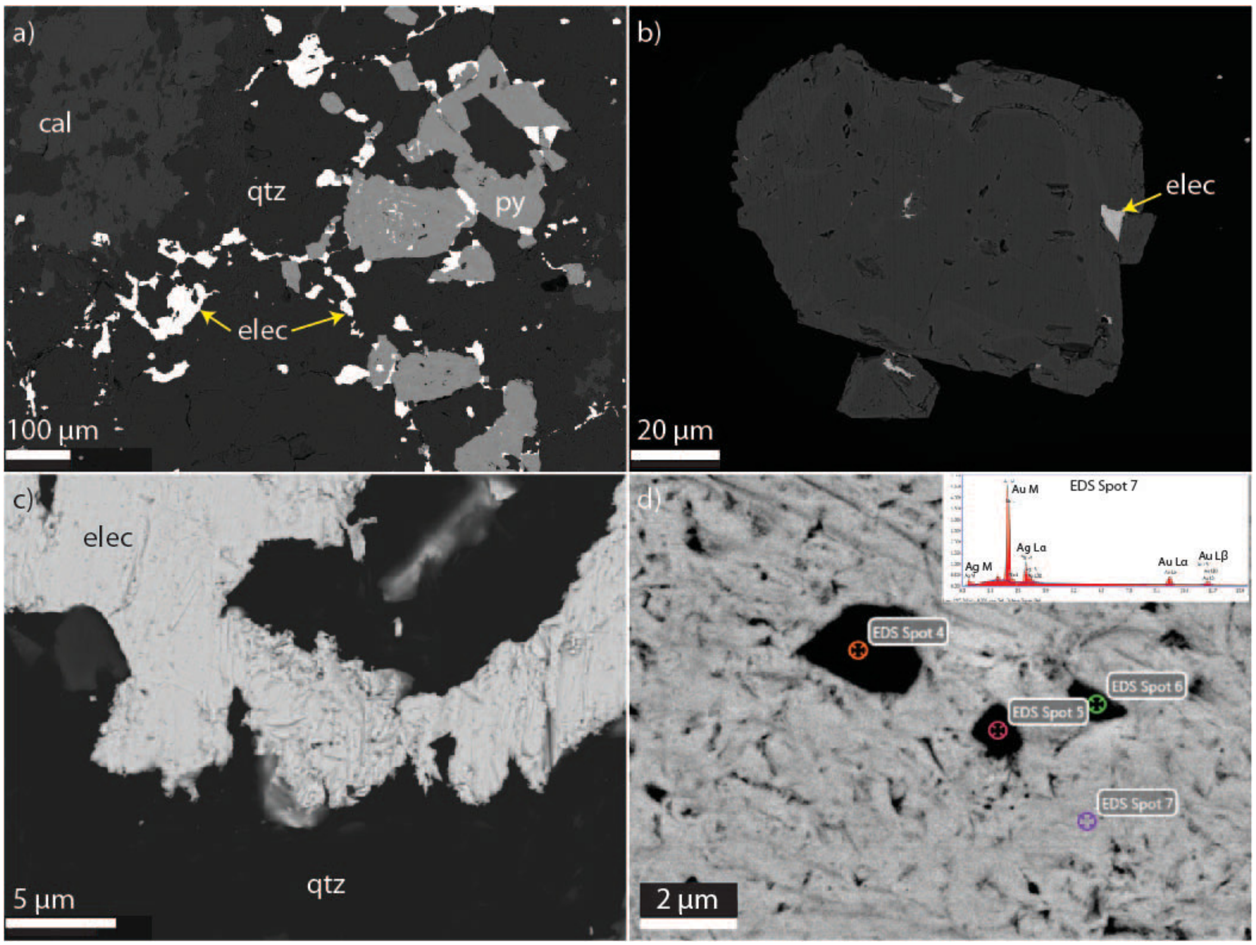

Figure 3.18 Back scattered electron (BSE) images from electrum bearing quartz-carbonate veins at Brucejack. All images are from thin section shown in Figure 3.16a, c. a) Electrum (elec) located interstitially between quartz (qtz) and calcite (cal) and electrum located at the surface and as inclusions within pyrite (py). b) Pyrite grain with electrum inclusions. Different shading within the pyrite may indicate zonation. c) Electrum within quartz showing bulbous grain boundary. Area of electrum affected by slide polishing can be seen. d) Image of porous electrum. Inset at top right shows EDS spectrum of EDS Spot 7.

BSE images show that electrum occurs as coarse dendritic networks and blebs predominantly within quartz and some calcite, as well as finer blebs and inclusions within and on the surface of pyrite grains (Figure 3.18). Coarse blebs and dendritic networks can be up to 400 μm wide and are usually confined to interstitial space within quartz. Although calcite is usually present where electrum mineralization occurs, only in a few examples is the electrum in contact with calcite. Electrum associated directly with pyrite is usually finer grained with surface blebs being $\sim$10-50 μm, and electrum inclusions within pyrite tending to be smaller ($<$10 μm). Electrum associated with pyrite looks to occupy fractures and cavities within the pyrite crystals. Also, a slight variation in shade within the BSE images shows zonation within the pyrite that is usually very irregular and resembles an agglomeration of fragments (Figure 3.18b).

As seen in optical microscopy observations of thin sections, the grain boundaries between either pyrite or quartz and electrum show two distinct textures. Figure 3.18c shows that they can be relatively smooth with a slight curve and punctuated by sharp points usually at an obtuse angle. They can also be tortuous and bulbous or botryoidal, with many embayments and protrusions on the scale of $<$1 μm with even smaller scale protrusions visible on these. The electrum itself is porous and hosts inclusions usually ranging in diameter from 100 nm to 2 μm (Figure 3.18d). Inclusions are shown with EDS spectra to consist of silica (Figure 3.19a) and pyrite. The EDS spectra for the electrum from this sample shows that it is composed of $71 \pm 9\%$ Au, $22 \pm 9\%$ Ag, and $7 \pm 8\%$ Nb (Figure 3.18f). EDS spectra done across different electrum masses or grains indicates that their relative Au-Ag ratio is constant throughout a single mass (Figure 3.19b), but as reported by Jones (2013), can be variable between samples.

TEM

While SEM provides a high resolution image of a material's surface, it does not provide information on the internal crystal structure. In order to probe the structure, electrons must be transmitted through a thin sample. The interactions between the electrons and the

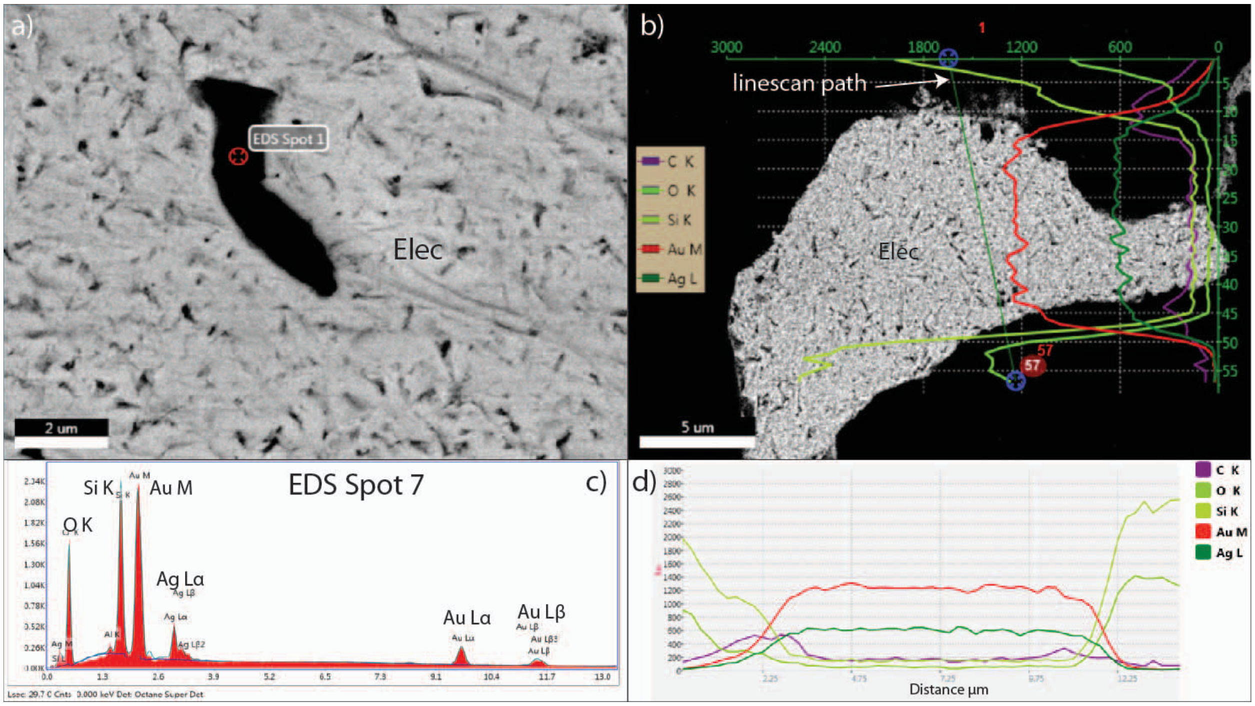

Figure 3.19 Back scattered electron (BSE) images of electrum from the Brucejack. These observations were made on thin section in Figure 3.16b, d, e, f. a) Inclusion of silica within electrum (Elec) as shown by EDS measurement at EDS Spot 1. b) EDS linescan across electrum grain. Linescan path shown in dark green. 57 measurements of relative amounts of C, O, Si, Au, and Ag were made at 200 nm intervals. c) EDS spectra for EDS Spot 1 in (a). Spectra shows both Si and O peaks as well as Au and Ag, which could be contamination from surrounding electrum due to EDS spot size being larger than inclusion. d) EDS linescan graph showing EDS measurements of relative amounts of C, O, Si, Au, and Ag as function of distance across electrum grain shown in (b). Note the relatively consistent Au:Ag ratio across the electrum grain.

structure within the sample are then imaged and the intensity of the electron beam passing through a sample gives a bright-field TEM image. The amount of scattering the electron beam undergoes is a function of sample thickness, atomic number, and crystal structure complexity. By moving the imaging plane, a diffraction pattern can also be imaged. A dark-field TEM image is obtained by adjusting the aperture within the TEM to only allow electrons which have only be reflected at a certain angle through. This allows imaging of specific crystal structures (Williams and Carter, 1996).

In order to image an electron beam passing through a sample the sample must be very thin, usually 100-200 nm (Wirth, 2004). To prepare such a sample (termed a foil), a focused ion beam (FIB) mill is used to cut, thin and lift a small portion of a thin section or other sample under the observation of an SEM. The process using a FIB to prepare foils for TEM use is fully described in Giannuzzi and Stevie (1999) and Wirth (2004). Samples to be analyzed were sent to the McGill University FEMR to be prepared by a trained technician using a FEI Helios Nanolab 660 DualBeam FIB-SEM. TEM observations were made on a FEI Tecnai G^2 F20 200 kV Cryo-STEM with EDAX Octane T Ultra W / Apollo XLT2 SDD and TEAM EDS Analysis System also located at the McGill University FEMR.

TEM analysis of samples from Brucejack was done on foils from two thin sections of quartz-carbonate vein (vein 1a) containing no electrum, and two thin sections of electrum bearing quartz-carbonate vein. One electrum-bearing sample was obtained from Pretium Resources as previously described, and the other was sampled from the electrum bearing vein visible in Figure 3.7b and Figure 3.16b, d, e, f. The purpose of this analysis was to: search for evidence of amorphous silica precipitation such as inclusions of amorphous silica phases within quartz or structures of amorphous silica phases such as opal, and to search for precious metal nanoparticles.

The first observation made was the appearance of large elliptical patches of amorphous silica within some of the FIB foils. Selected area electron diffraction (SAED) of this area revealed no crystalline structure, but areas surrounding the amorphous patches consisted of crystalline quartz (Figure 3.20a). This elliptical area also shows a lighter colour than the rest of the sample. However, EDS results show it is composed of silica similar to the rest of the sample. Because of the increased electron beam intensity passing through this region, it can be deduced that the sample here is thinner and potentially the amorphization occurred during the FIB milling process. Furthermore, after a crystalline quartz area was analyzed, that area was also observed to be amorphous (Figure 3.20b), indicating that the electron beam destroys the crystal lattice structure of quartz. In some cases, damage could be seen in less than 30 seconds while multiple TEM images were taken, each image showing progressively more damage. This complicates the search for amorphous silica.

Figure 3.20 shows foils taken from quartz-carbonate veins that did not have any visible electrum mineralization. The quartz within these veins was seen to be all crystalline (except

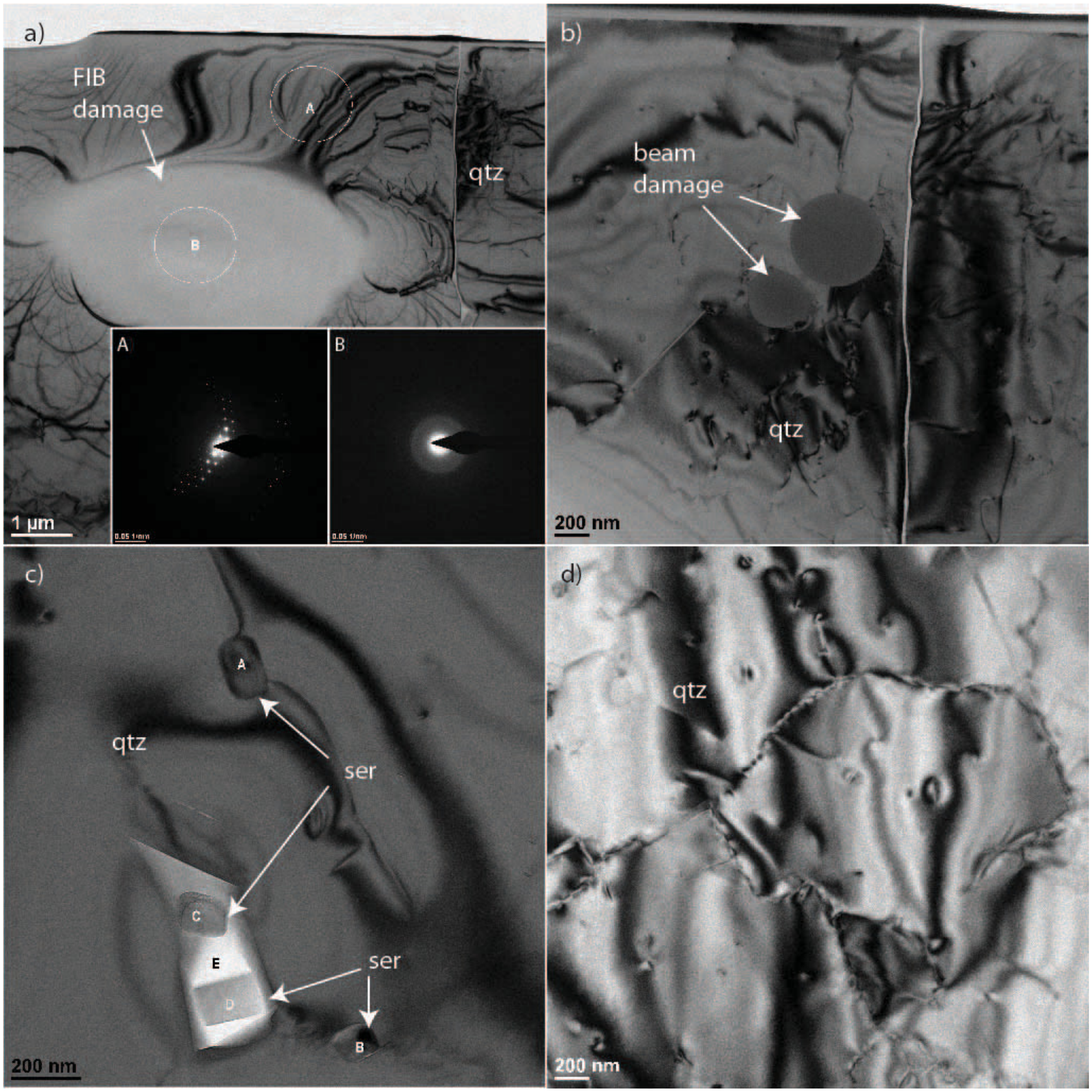

Figure 3.20 Bright-field TEM images of samples of quartz-carbonate vein 1a from the Brucejack. a) Image showing overview of FIB foil of quartz-carbonate vein thin section. Selected area electron diffraction (SAED) patterns of areas A and B are shown in inset highlighting the elliptical region of amorphous material caused by FIB damage in the centre of the TEM image (B). Thickness and bend contours can be seen as black arcuate bands within the surrounding sample. b) Image showing beam damage in quartz. c) Image of sericite inclusions in quartz. Thickness and bend contours can be seen emanating from and surrounding inclusions. d) Image showing 2 μm diameter quartz grain within quartz-carbonate vein. Dark lines are thickness and bend contours.

for beam damaged zones), and lacked a high density or preferred orientation of dislocations within the quartz crystals. Contour and thickness bands, which are a result of different refraction of electrons due to changes in sample thickness or a bending or warping of the sample (Williams and Carter, 2009), only occur in crystalline material and can be seen in both quartz samples. These emanate from and surround areas of FIB damage, as well as inclusions. The 2 μm sized grain depicted in Figure 3.20d is part of an area of microcrystalline quartz+calcite+sericite (quartz phase 3) in a vein 1a, taken from the underground workings of the Brucejack deposit (seen in Figure 3.14d). At the top-right and top-centre of this grain are boundaries with $\sim$120° intersections and at centre is a small $\sim$100 μm inclusion with an unknown composition.

Figure 3.21 shows TEM images of a foil taken from the thin section provided by Pretium Resources containing electrum-bearing quartz-carbonate (Figure 3.16b). An image of the entire FIB foil is shown in Figure 3.21a. Although there are numerous thickness and bending contours, there are relatively few dislocations within the quartz seen surrounding the electrum. As in the barren quartz samples, these emanate and surround holes within the foil and inclusions (Figure 3.21a). Detailed bright-field TEM images at high magnification show that some of the quartz within this sample contains relict spheres (of silica) that are 2-5 nm in diameter (Figure 3.21b). Dark-field TEM imaging (Figure 3.21c), shows one region of quartz with alternating crystal lattice structures within a 100 nm wide band. Elsewhere, dark-field TEM indicates a relatively consistent crystal structure.

The electrum quartz grain boundaries at this high level of magnification are very sharp except at one instance near the edge of the foil. Figure 3.21d shows $\sim$50 nm wide, 100-200 nm long protrusions with rounded edges. EDS measurements at spots on these protrusions yield spectra indicating a composition of electrum and silica. The surrounding silica at this location has a much less consistent pattern with a mottled appearance when compared to the quartz in the rest of the sample. Figure 3.21e, f show the occasional presence of 10-20 nm dark spheres located within quartz near the electrum quartz grain boundary. These occur in a location where the FIB foil is very thin. The spheres have a crystalline structure that is occasionally radiating. EDS spectra indicate that they consist of Ag and silica, although the

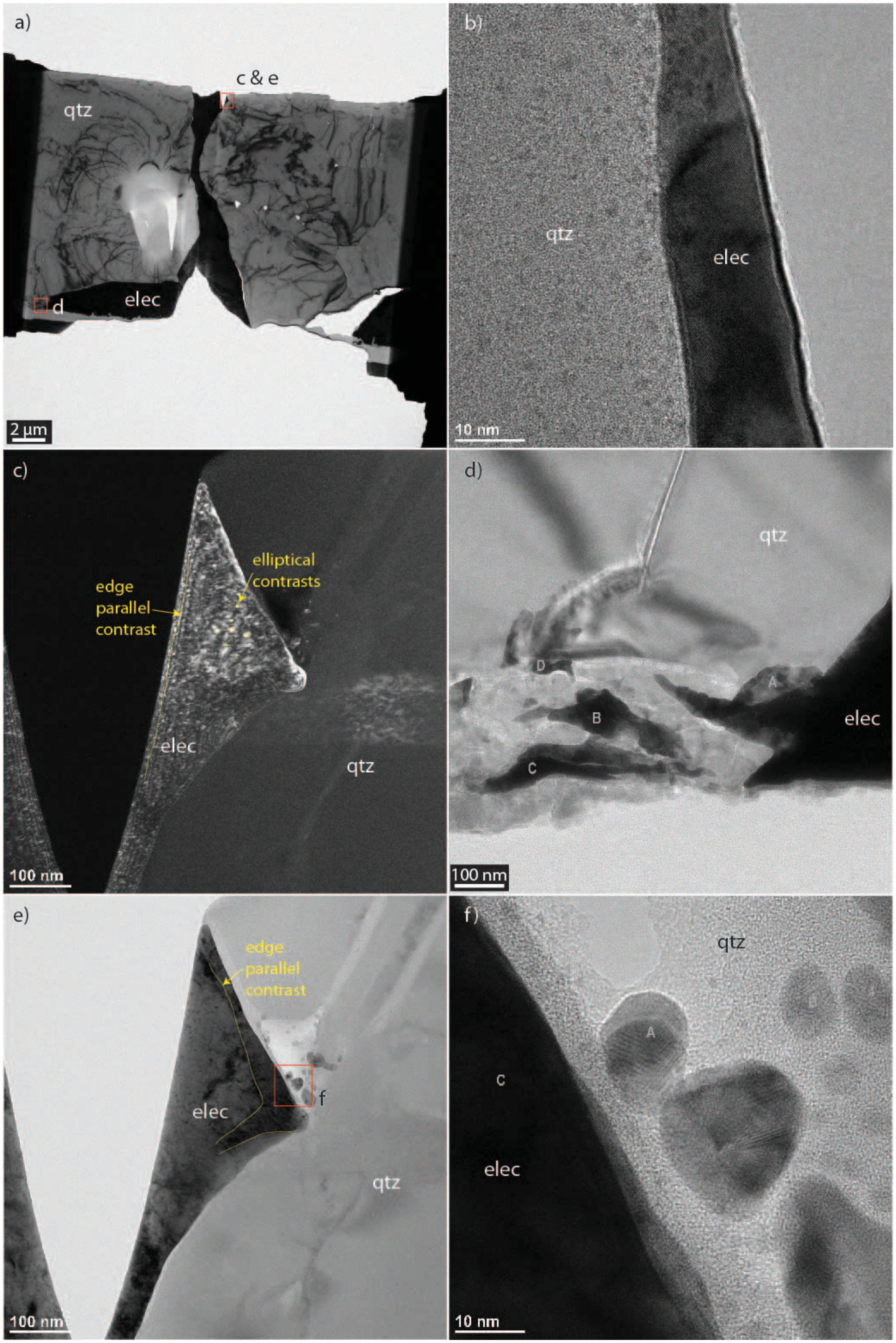
a)
c & e
qtz
elec
d
2 µm
b)
qtz
elec
10 nm
c)
elliptical contrasts
edge parallel contrast
elec
qtz
100 nm
d)
qtz
D
A
B
C
elec
100 nm
e)
edge parallel contrast
elec
f
qtz
100 nm
f)
qtz
A
C
elec
10 nm

Figure 3.21

Figure 3.21 (Previous page) TEM images of sample of electrum bearing quartz-carbonate vein from Brucejack. FIB foil imaged is taken from thin section shown in Figure 3.16a, c. a) Bright-field TEM image of entire FIB foil taken from thin section shown in Figure 3.16a, c. Electrum (elec) can be seen in black cutting through the centre of the foil and along the bottom left. An area of FIB damage within quartz (qtz) is present to left of the electrum in the centre of foil. Locations of photos c,d, and e are shown in red. b) Detailed bright-field TEM image of quartz electrum grain boundary showing small relict spheres (2-3 nm diameter) within the quartz. c) Dark-field TEM image from location shown in (a) highlighting the change in crystal orientation within the electrum (see text for discussion). d) Bright-field TEM image showing quartz electrum grain boundary. Elongate protrusions of electrum that are made up spherical particles can be seen below A, and at C and B. This image is taken from the edge of the foil at location f in (a). e) Bright-field TEM image of of (c). Note small spheres along the top right of the boundary as well as the brightness contrast within the electrum. Location of photo e shown in red. f) Detailed bright-field TEM image of spheres seen in (d). EDS spectra indicate that the spheres (A and B) consist of Ag. Note crystalline pattern within the spheres.

silica signal may derive from the surrounding quartz.

At the μ scale, bright-field TEM imaging of the electrum cutting through the centre of the slide depicts the electrum as a consistent black mass. However, at higher magnification, detailed bright-field TEM (Figure 3.21e and Figure 3.22) and dark-field TEM (Figure 3.21c) show a more complicated internal structure. Bright-field images (Figure 3.21e) show that the electrum has irregular dark spots that coalesce to make darker zones that can be up to 100 nm across as well as linear zones of darker shading running parallel with the quartz-electrum grain boundary. Dark-field TEM shows that the electron refraction through the electrum varies considerably, with edge parallel brightness contrasts running along the left edge of the electrum where there is a hole in the foil and alternating bright and dark spots on the scale of 5-20 nm throughout the middle of the electrum mass.

Figure 3.22 shows electrum containing nanoparticles. The FIB foil imaged in Figure 3.22a is composed of crystalline quartz along the bottom and right that is cut by a hole that stretches from the middle left to the top right. Electrum can be seen as the dark material along the edge of this hole and as the dark mass in the top left of the foil. Detailed bright-field imaging of the electrum along the edge of the hole is shown in Figure 3.22b. Here, dark spheres ~3-12 nm in diameter can be seen to make up the electrum mass, and the edges of the electrum along the hole are bulbous. The diameters of bulbous protrusions are between 50-200 nm, which is similar to those seen in SEM images of electrum in Figure 3.18c. Detailed bright-field TEM imaging of the dark spheres within the electrum shows that the spheres

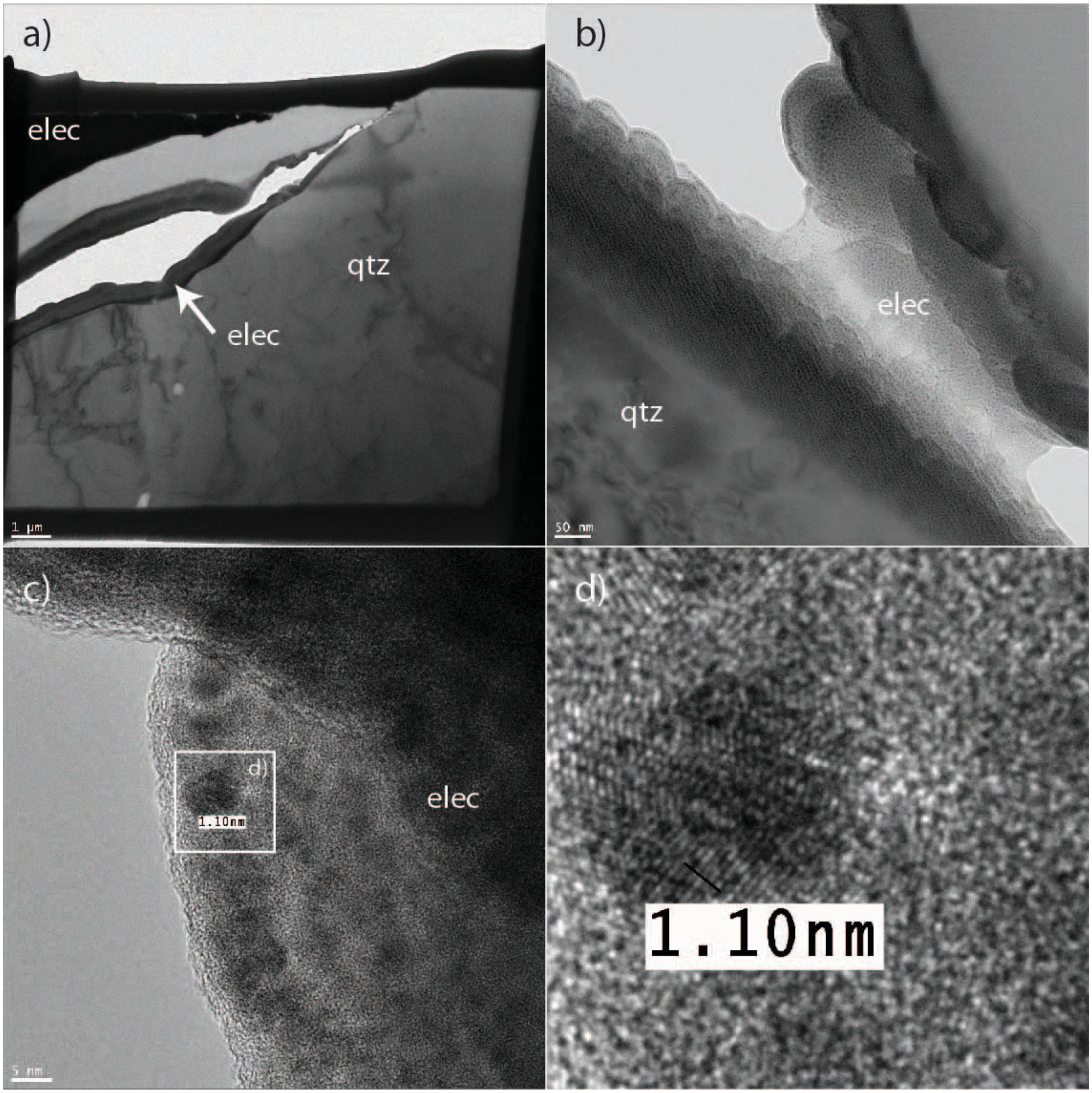

Figure 3.22 a) Bright-field TEM imaging of entire FIB foil taken from electrum bearing quartz-carbonate vein thin section shown in Figure 3.16b, d, e, f. Dark mass in top left hand corner is electrum. Cutting though the foil from the middle left to the top right is a hole with electrum along the edges. b) Detailed image of electrum along edges of the top right portion of the hole in (a). Small dark spheres give the electrum a spotty appearance at this scale. Boundaries along the hole are bulbous with a diameter from 50-100 nm. c) Detailed image of electrum containing mall dark spherules ∼3-12 nm in diameter. Location of (d) shown. d) Image of electrum sphere shown in (c) showing crystal lattice structure. The dark bar 1.10 nm long shows a crystal lattice spacing of ∼0.22 nm (1.10 nm / 5 lattice planes) in this projection plane.

have a crystalline lattice (Figure 3.22c, d). The lattice spacing here was measured in the viewing plane and determined to be 0.22 nm (1.10 nm / 5 lattice planes), while in another nanoparticle the same type of measurement yielded a spacing of 0.24 nm. The crystal lattice of each nanoparticle was observed to change orientation within the lighter interstitial material between each sphere. Accurate EDS measurements on individual spheres and interstitial spaces was not possible as the beam size was generally larger than the diameter of the spheres. Therefore, it was not possible to determine if different spheres had different ratios of Au to Ag.

Several key observations were made on samples from the Brucejack deposit. SEM revealed that electrum exists as both dendritic networks and fine blebs and inclusions associated with quartz and/or pyrite. Electrum was seen to have botryoidal or relatively straight grain boundaries and was porous and contained silica and pyrite inclusions. Bright-field TEM analysis found evidence for amorphous silica precipitation as small ghost spheres of silica in crystalline quartz adjacent to electrum. Ag nanoparticles adjacent to electrum were also observed. Bright-field and dark-field images revealed that the electrum consists of ellipsoidal crystalline nanoparticles $\sim$3-12 nm in diameter. Examination of crystal lattice orientations in dark-field images also suggested variations in lattice orientation on the few-nm scale within some areas of adjacent quartz crystals.

CHAPTER 4

Observations: Dixie Valley

Quartz veins and vein stockwork systems related to the Stillwater fault zone (SFZ) in Dixie Valley, Nevada were examined at the two previously described localities, the Mirrors, and the Dixie Comstock mine. Field observations and sample collection occurred in March 2015 and samples were analyzed by optical microscopy and transmission electron microscopy (TEM) at McGill University.

4.1 The Mirrors

Field observations made at the Mirrors locality and surrounding outcrop reveal a complex fault system with multiple phases of slip and hydrothermal activity. Occurrence of cryptocrystalline silica, easily scratched with a knife, that could represent amorphous silica precipitation, is evident on fault surfaces and within fault breccia. Initial observations at the Mirrors locality indicate a significantly lower volume of stockwork veining and vein breccia than seen at the Brucejack deposit.

Although the entire footwall outcrop area of the Mirrors is mapped as Jurassic gabbroic and dioritic rocks (Page, 1964), multiple lithologies are observed. Amygdaloidal basalt, granodiorite, and ropey lava flows all outcrop within 1 km of the Mirrors locality. Within the hanging wall, no crystalline rocks were observed. It consisted of a pervasively silica-altered matrix-supported conglomerate/breccia. As noted by previous workers, there is a continuum between cemented talus and fault-brecciated rocks (Power and Tullis, 1989; Caine et al., 2010). Abundant rounded clasts suggest that this unit consists of a fault-brecciated cemented talus. To the south of the main Mirrors outcrop, vuggy silica crops out within the talus slope. This could be a zone of intense alteration (high sulphidation, low pH leaching) or of rhyolitic ash flow tuffs (e.g., Vikre, 1994).

The observed fault geometry of the SFZ (Figure 4.1) matches the description by Caine et al. (2010). The fault core consists of variably silicified fault breccia that is largely clast-supported. The breccia is poorly sorted, has sub-angular clasts, and is cemented with a fine-grained light yellow silicified matrix containing limonite and calcite. The clasts are generally silicified and contain hematite. Zones of silicified gouge are likely the matrix-supported pods described by Caine et al. (2010). These contain clasts of silica+hematite+limonite+epidote altered rocks with a few relict textures that resemble the granodiorite found within the crystalline footwall. Clasts are from 1 mm to 10 cm in diameter, are sub-rounded and exhibit low to medium sphericity. The matrix also consists of fine-grained silica with minor limonite and calcite. Within the matrix-supported pods, discrete, fairly planar slip surfaces form on their contacts betwee clast-supported breccia and within the pods themselves. These are the slip surfaces that form the smooth, reflective, silicified surfaces known as the Mirrors. These surfaces range from 1 mm to several cm thick. Some slip surfaces within the matrix-supported breccia/conglomerate are more poorly developed and do no exhibit a shiny crystalline surface. These contain pits where clasts have might have been plucked out of the matrix or, were formed by the dissolution of calcite. The well-developed mirrors are generally aligned parallel to the SFZ (striking NE, dipping approx. 40° SE). However, small variations in strike,

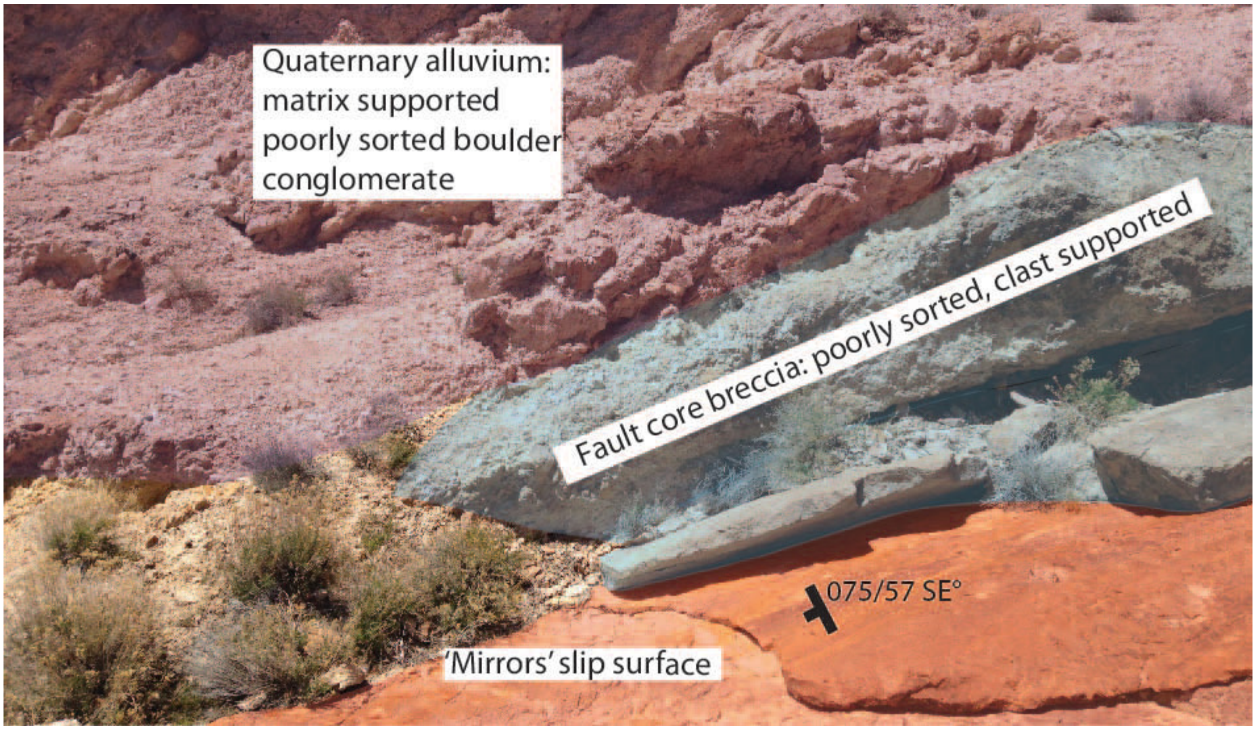

Figure 4.1 Photograph of Stillwater fault zone outcrop at the Mirrors, Dixie Valley, Nevada.

multiple surfaces (that can intersect), as well as differing orientations of kinematic indicators all indicate that multiple slip events were responsible for their formation. Intersecting fault planes without obvious cross-cutting relationships were also observed indicating that a single slip event likely occurred on more than one plane. Within the footwall of the mirrors surfaces are two vein generations. One, variably oriented, dark red, iron carbonate set, and another with a light blue to translucent beige lustre and consistent orientations. The iron carbonate veins are multiphase with anastomosing bands of iron carbonate separated by small slivers and pods of cryptocrystalline silica.

Outside of the fault core is the damage zone described by Caine et al. (2010). Here, a decreasing fracture intensity (10 major fractures/m to 1 major fracture/m) is observed with increasing distance away from fault core. Multiple brittle faults occur with similar orientations to the main SFZ. Associated with these fractures are angular breccias, and veins with cryptocrystalline silica. In some cases the cryptocrystalline silica is creamy white and filling irregular fractures in the country rock, while in other cases, crystalline comb quartz can be seen coating clasts in breccia and filling fractures. Calcite fills pore space within many of these breccias. Some slip surfaces here have silica coating, but they lack the shiny mature smooth lustre of the mirrors. Further into the footwall, normal faults juxtaposing crystalline rock contain a 0.2-1 m wide anastomosing fault core with silicified gouge and matrix supported fault breccia but no 'Mirrors-like' slip surfaces.

4.2 Dixie Comstock mine

Increased stockwork quartz-carbonate veining, compared to the Mirrors, is observed within the breccia and fault zone at the Dixie Comstock mine. Here, significant silicified fault breccia outcrops on surface. Fault breccia show multiple phases of veining with intense pink silicification along with hematite+epidote±ankerite±limonite alteration of clasts, vug-coating quartz veins, and late phase interstitial calcite. Iron oxide alteration of clasts is more pervasive on clast rims. Large clasts of previously formed breccia are contained within this breccia indicating multiple fracture events. Within the largest fault breccia unit, zones of the most intense alteration contain tabular breccias with clasts composed of older vein chips. There are also weathered surfaces ($\sim$ 6 cm thick) that resemble smooth silica-coated slip surfaces striking north-northeast, dipping 40° E. Beneath these surfaces is fine-grained silicified gouge that contains cryptocrystalline silica veins. The surfaces, thought to be old mirrors-like slip surfaces upon initial observation, can be oriented perpendicular to the main fault plane. Fault zones oriented parallel to the SFZ occur in the footwall away from the Stillwater range front. Here they have a similar geometry and size as the footwall normal faults seen at the Mirrors locality. Gouge within these fault zones contain quartz veins that pinch and swell. Within narrow zones they contain massive, white cryptocrystalline white silica, and where they swell, they contain euhedral vug-coating quartz.

4.3 Optical microscopy

Samples of quartz veins, breccias, and silica-coated slip surfaces associated with the SFZ in Dixie Valley were analyzed using optical microscopy in order to describe quartz and/or silica textures that may be associated with amorphous silica precipitation and recrystallization. Samples were cut into small blocks at McGill University and sent to Wagner Petrographic in Linden, Utah, USA or Vancouver Petrographic in Langley, British Columbia, Canada for thin section preparation.

4.3.1 The Mirrors

Thin sections were made from hand samples taken from slip surfaces and cataclasite within the SFZ at the Mirrors locality, as well as veins and breccias within the damage zone in the footwall of the SFZ. Detailed description of the slip surface samples are presented first, then those of various samples from the damage zone.

Slip surface

The Mirrors fault slip surfaces appear as layer of vitreous quartz <0.5 cm in width (Figure 4.2). This layer contains a network of quartz surfaces with the same crystal preferred orientation (CPO)(Figure 4.3a, b). Where calcite, and other minerals such as Fe-oxide are more abundant in this layer, the CPO quartz networks are less obvious but are still observed. These areas may coincide with darker orange and red parts of the mirrors slip surface with the increased Fe-oxide abundance giving them their colour (Figure 4.2). Figure 4.3a shows the CPO network consists of major, subparallel, anastomosing surfaces, between 0-15° steeper in apparent dip, than the actual fault slip surface. Figure 4.3b also shows lesser surfaces that are almost orthogonal to, and connect the major planes. Between the CPO surfaces is microcrystalline quartz and interstitial calcite. In some areas, low birefringence planes within the vitreous quartz layer are more shallow dipping than main mirrors slip surface (Figure 4.3b). These low birefringence surfaces are composed of microcrystalline quartz or opal as no

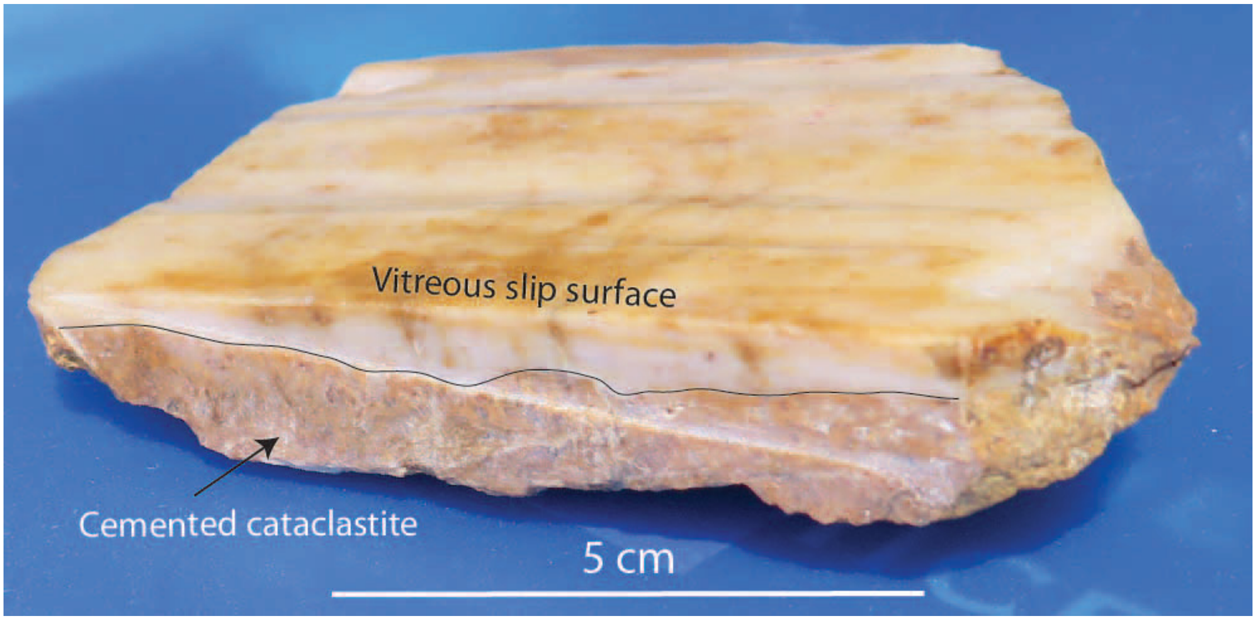

Figure 4.2 Photograph of hand sample from a slip surface within the SFZ at the Mirrors locality.

grain size could be determined at the highest magnification on the microscope.

Cataclasite

Directly beneath the vitreous quartz slip surfaces, there is a sharp contact with cemented cataclasite (Figure 4.2). This matrix-supported breccia contains clasts of Fe-oxide (hematite+limonite), larger quartz grains, and older breccias with a similar composition. The quartz grains have tortuous grain boundaries and at these boundaries, there are subgrains with the same diameter as quartz grains in the matrix (~10 μm) (Figure 4.3c). The cemented cataclasite also has multiple surfaces that are parallel to the main slip surface. These surfaces separate the matrix supported breccias into bands with different Fe-oxide, quartz, and calcite modal abundances as well as zones with different clast to matrix ratios. In most cases the matrix is microcrystalline quartz+Fe-oxide+calcite+sericite. Grains of all minerals within the matrix rarely exceed 10 μm in diameter.

The microcrystalline quartz-supported breccias are cross-cut by Fe-oxide altered carbonate veins and carbonate cemented breccias (Figure 4.3c,d). Within this breccia matrix, calcite shows a bimodal grain size distribution. Figure 4.3d shows blocky, coarser grained calcite

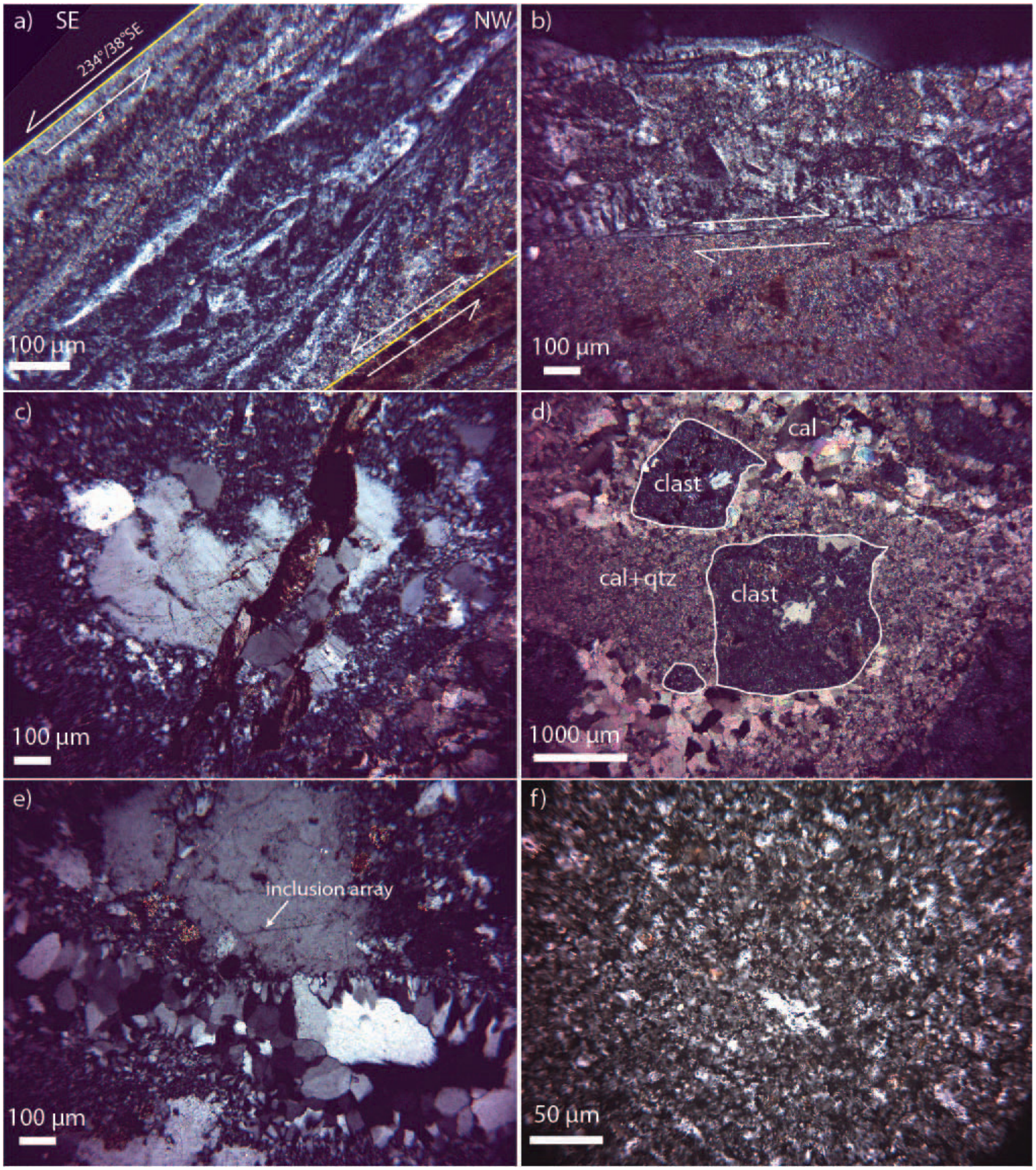

Figure 4.3 Photomicrographs of samples from the Mirrors. a) Cross section of Mirrors slip surface showing translucent quartz layer with network of quartz with the same CPO. Top slip surface with orientation is the surface of the Mirrors seen in outcrop (XPL). b) Translucent quartz layer from the Mirrors slip surface showing both the quartz CPO network and surfaces of low birefringence fine grained quartz (XPL). c) Cemented cataclasite directly beneath quartz networks in the Mirrors slip surface. Many of the clasts consist of quartz with subgrains at the boundaries that are the same diameter of the microcrystalline quartz matrix. Fe-oxide + calcite veins cross-cut the cataclasite (XPL). d) Calcite cemented breccia from the Mirrors footwall showing bimodal calcite grain size distribution (XPL). e) Syntaxial quartz vein with interstitial anhedral quartz cross-cutting cataclasite containing coarse quartz grains with hexagonal inclusion array (XPL). f) Microcrystalline quartz+Fe-oxides+calcite+kaolinite within mode 1 fracture in the footwall of the Mirrors slip surface (XPL).

(100-200 μm) occurring in patches with little to no deformation twins and finer grain calcite (<50 μm) that is intermixed with microcrystalline quartz. The clasts within the calcite cemented breccias consist of microcrystalline quartz supported breccia.

Damage zone

Several samples of breccias, as well as veins, were taken from within the footwall of SFZ at varying distances away from Mirrors slip surface. Some breccia samples resembled the cemented cataclasite seen directly beneath the vitreous surfaces at the Mirrors. However, some breccia samples show a coarser grained matrix of quartz where there is a higher clast density and in many cases there is quartz nucleation on the clast and radial growth away from the clast surface. In some cases, radially growing comb quartz crystals have euhedral termination similar to the phase A quartz seen at Brucejack. The remaining space in the matrix is filled with calcite or exists as open vugs. Clasts consist of Fe-oxide and clay altered wallrock, coarser quartz grains, or older cataclasite. The coarse quartz grains have the same texture as described before, with subgrains at their boundaries being of similar size to those of microcrystalline quartz in the matrix. They are different however, in that some of these coarser quartz clasts can contain inclusions arranged in linear or hexagonal arrays (Figure 4.3e). These grains tend to occur in areas of samples with a wider distribution of grain size and a lesser number of angular clasts. Therefore, they may have originated as quartz grains within the host rock.

Cherty, cryptocrystalline silica veins form within tension gashes, and continuous fractures in crystalline wallrock in the footwall of the SFZ. In thin section these veins are revealed to be composed of microcrystalline quartz, fine grained Fe-oxides and interstitial calcite (Figure 4.3f). Microcrystalline quartz in these veins shows similar textures to phase C and phase D quartz at Brucejack. Grain boundaries are interpenetrating and torturous and resemble mosaic quartz textures (e.g., Figure 1.4 Lovering, 1972; Saunders, 1990; Dong et al., 1995). These veins appear as either a single phase within a fracture or several phases along faults.

The single phase veins have a consistent pattern and grain size distribution across the entire vein with quartz grains rarely exceeding 10 μm (Figure 4.3f). Different phases within fault veins can be differentiated via grain size where the larger grain-size phases tend to be nearest to the vein wall. The boundaries between the phases have flow textures with many of them following embayments within wall rock (e.g., Figure 4.4d).

Thin section observations at the Mirrors outcrop on the Stillwater fault zone in Dixie Valley show several quartz textures. The two key textures observed are that of the CPO networks on the Mirrors slip surface and the mosaic quartz observed in tension gashes in the footwall of the Mirrors. As amorphous silica was previously found in a sample from the slip surface (Figure 1.5c; Rowe et al., 2012), and the mosaic quartz texture is indicative of recrystallization from an amorphous silica phase (Lovering, 1972; Saunders, 1990; Dong et al., 1995), these samples were further investigated using electron microscopy to look for nanoscale textures indicating an amorphous origin.

4.3.2 Dixie Comstock mine

Several samples of quartz veining and vein stockwork in fault breccia, were taken from the Dixie Comstock mine. Compared to the samples from the Mirrors locality, these samples have coarser grained euhedral quartz and less Fe-oxide and calcite mineralization.

Euhedral quartz within these breccias tends to nucleate on fine grained to microcrystalline quartz intermixed with Fe-oxides, calcite and clays. Coarse quartz growth occurs as comb quartz growing either into vugs or linear fractures, with quartz grain size increasing away from the nucleation point similar to phase A quartz at Brucejack (Figure 4.4). Coarse-grained quartz (100-200 μm) has euhedral crystal termination when growing into vugs that can be still open or filled with calcite (Figure 4.4a). If the open space has been entirely filled with coarser grained quartz, the quartz becomes blocky (similar to phase B quartz) within the centre. These blocky quartz crystals show a feathery extinction pattern in many cases (Figure 4.4b). Euhedral quartz has numerous inclusions which are usually aligned radially in the

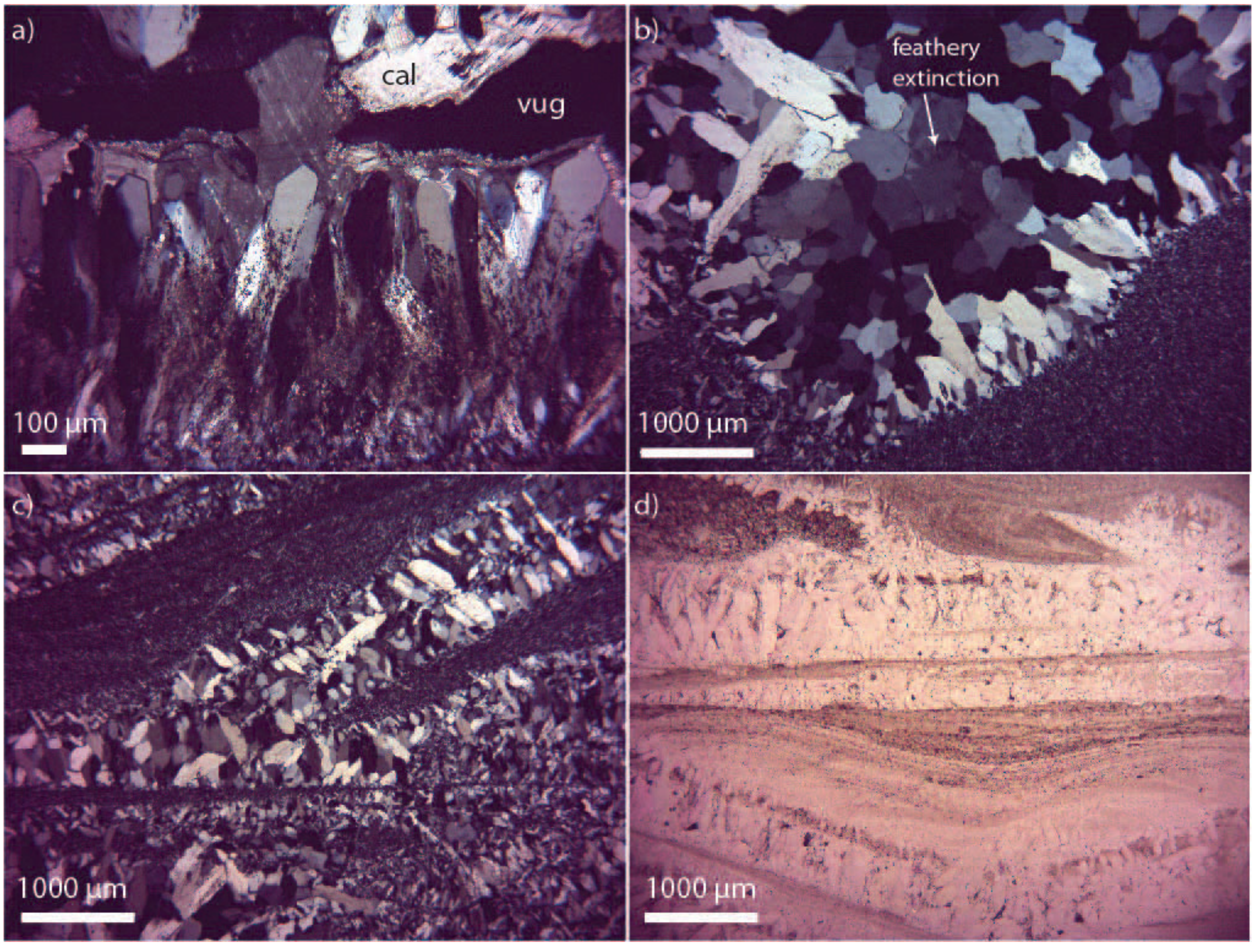

Figure 4.4 Photomicrographs of samples from the Dixie Comstock Mine. a) Euhedral comb quartz growing into vug partially filled with calcite (cal). Inclusion density decreases towards vug (XPL). b) Vug filled with blocky quartz with centre quartz grains exhibiting fleathery extinction (XPL). c) Tabular quartz breccia with syntaxial comb quartz growing within linear fractures (XPL). d) Tabular quartz breccia showing banding of microcrystalline quartz and interstitial fine grained quartz between coarse quartz grains and at centre of vug at top left (PPL).

direction of quartz growth (i.e., towards the centre of the vug or vein). Inclusion density is greatest near the base of the quartz crystals and it dramatically drops off towards the euhedral termination (Figure 4.4a). This occurs wherever there are vugs, but if quartz crystals are terminated, inclusion density may remain the same throughout the entire crystal.

Microcrystalline quartz from which euhedral quartz nucleates can have a relatively consistent grain size (<20 μm) with occasional quartz grains reaching up 50 μm in diameter. Other areas of microcrystalline phase have grain sizes that are consistently larger (<100 μm). In the vein chip breccias, linear banding of the microcrystalline quartz shows phases of different grain sizes. This banding texture is similar to that seen at the Mirrors, with banding following embayments (Figure 4.4d). Within these breccias, interstial space between coarser quartz grains is filled with fine grained quartz+calcite+Fe-oxides and clay. Fine grained quartz boundaries are non-distinct and tortuous, and the texture resembles the very fine grained quartz seen at the Mirrors locality and at Brucejack (quartz phases C and D).

4.4 Electron microscopy

To properly compare quartz and potential amorphous silica between Brucejack and Dixie Valley samples, TEM observations were also conducted on two samples from the Mirrors outcrop. Preparation was conducted in the same manner as the Brucejack samples and observations were also made at the McGill FEMR. FIB foils were taken from vitreous microcrystalline quartz with CPO networks observed directly on the Mirrors slip surface (Figure 4.3a, b), and from cryptocrystalline quartz within veins in the footwall of the Mirrors slip surface (Figure 4.3f).

Figure 4.5 shows bright-field TEM images of the FIB foils from the two samples. Quartz from both the slip surface and tension gashes in the footwall of the Mirrors is seen to be made up of nano-microcrystalline quartz grains that can be <100 nm in diameter. Microcrystalline kaolinite was also observed with microcrystalline quartz in the footwall sample. Figure 4.5a shows distinct subhedral to euhedral grains that are largely dislocation free forming a polygonal mosaic aggregate (e.g Bestmann et al., 2012). Both the sample from the fault slip surface (Figure 4.5b) and the footwall (Figure 4.5c) show relict textures of silica nanoparticles. Detailed images reveal that the crystalline quartz contains darker spherules or ellipsoids that are ∼5-15 nm in diameter. They are contained within a matrix of quartz that appears lighter in the bright-field TEM images. Most of the areas show that many of the spheres are not in contact with each other and that the spacing between them is fairly consistent (∼2-5 nm). SAED images show that the quartz, including both spheres and matrix is crystalline. The crystallographic orientation of quartz is either homogenous across spherules and matrix, or varies between spherules. In microcrystalline quartz from the slip surface, changes in lattice plane orientation occur at quartz grain boundaries and dislocations (Figure 4.5b). This also occurs in microcrystalline quartz from the footwall tension gashes, but in some areas spherules each have a different lattice plane orientation (Figure 4.5c). The clearly visible relict spherules in both samples of microcrystalline quartz are ubiquitous throughout both of the FIB foils and thus can be assumed to be representative of the the nano-microcrystalline quartz from which the FIB foils were taken (Figure 4.3a, b, f).

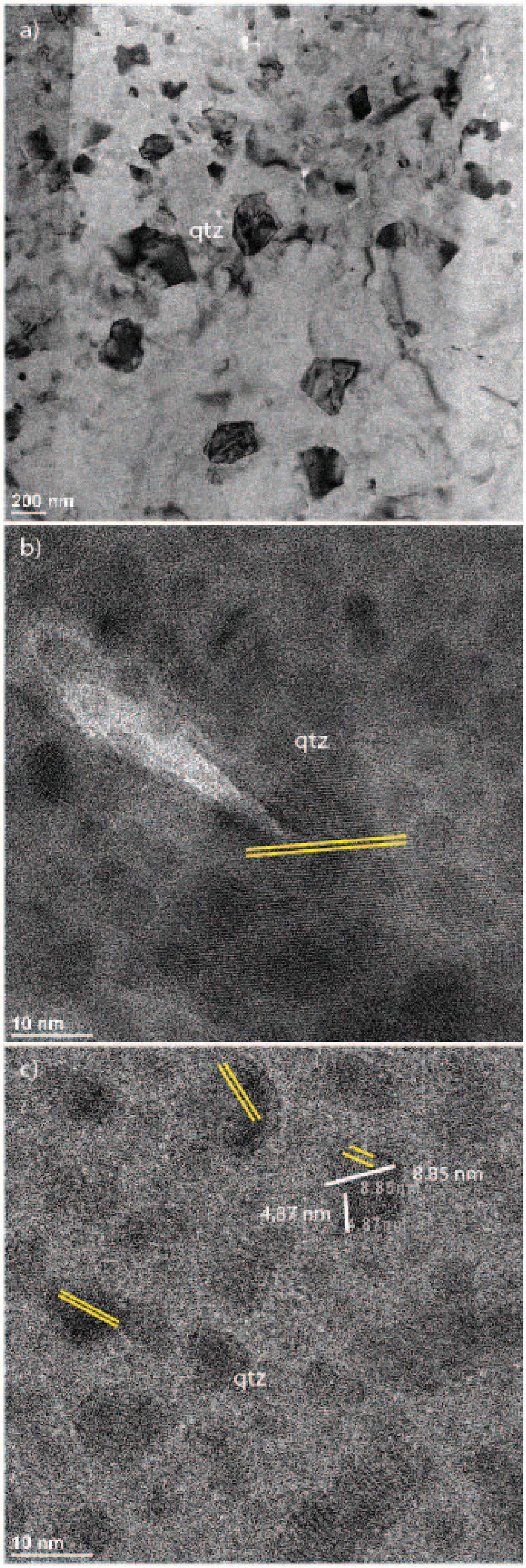

Figure 4.5 Bright-field TEM images of samples of quartz-carbonate veins from Dixie Valley, Nevada. a) Nano-crystalline quartz grains forming a polygonal mosaic aggregate within vitreous quartz layers from the Mirrors slip surface. b) Image of quartz from Mirrors slip surface showing spherules and matrix with a consistent lattice plane orientation (yellow lines). The origin of the bright spot in the middle of the image is unknown. c) Image of spherules within microcrystalline quartz within tension gashes in the footwall of the Mirrors. Yellow lines show that each spherule has a different lattice plane orientation. White lines show the dimensions of spherules within quartz..

CHAPTER 5

Discussion and conclusion

Observations of veins and faults at Brucejack and Dixie Valley are presented at all ranges of scale, from nanometre to metre. All of these are used to discuss the three questions presented in the introduction of this document:

1. **Is there textural evidence for the deposition of Au nanoparticles?**
2. **Are there specific structural trapping sites for Au nanoparticles and amorphous silica precipitation?**
3. **Is there evidence of long distance transport of Au nanoparticles?**

Using the framework provided by answering these questions, I examine the possibility that colloidal transport played a role in the formation of extremely concentrated and very high Au grades found in epithermal Au-Ag deposits like Brucejack. With this, and the structural setting of the deposit in mind, a general model for colloidal transport and its role in the formation of an epithermal precious metal deposit is proposed.

5.1 Textural evidence of precious metal nanoparticles

Direct observations of precious metal nanoparticles and indirect evidence supporting their existence within electrum can be seen at the Brucejack deposit. However, no observations of visible electrum were made at or within samples from Dixie Valley.

One instance of electrum at Brucejack is directly observed to consist of nanoparticles (Figure 3.22) with a similar size and shape to Au, Ag and electrum nanoparticles that have been prepared and observed in the laboratory. Giersig and Mulvaney (1993) prepared Au colloids with an average particle diameter of 14.1 nm, which is slightly larger than those seen at Brucejack (3-12 nm). Au nanoparticles prepared by Scott et al. (2012) and electrum particles prepared by Guisbiers et al. (2015) vary in size from 4-10 nm and are consistent with the electrum nanoparticles seen at Brucejack. High resolution bright-field TEM images of experimental electrum and Au nanoparticles all indicate a crystalline structure (Whetten et al., 1996; Scott et al., 2012; Guisbiers et al., 2015). Lattice spacing between planes in Au particles is indicated to be 0.235 nm by Whetten et al. (1996), while Scott et al. (2012) shows a measurement of 0.24 nm between lattice planes (Figure 1.3d). These measurements are in agreement with the two measurements made on the Brucejack electrum nanoparticles of 0.22 nm and 0.24 nm and are only slightly greater than the lattice spacing of Ag nanoparticles (0.21 nm, Bindhu and Umadevi, 2013). Due to beam size limitations, observed nanoparticles within electrum at Brucejack could not be determined to be a mix of Ag nanoparticles and Au nanoparticles or just electrum nanoparticles. Because of the consistent Au:Ag ratios seen in linescan EDS measurements (Figurelinescan), if there is a mixture of Au and Ag nanoparticles, their spatial distribution is likely homogenous.

Ag nanoparticles are also observed within electrum bearing quartz-carbonate veining immediately adjacent to electrum (Figure 3.21e, f). These Ag nanoparticles have the same approximate radius and appear to have a similar lattice spacing as synthesized Ag nanoparticles (Mock et al., 2002; Bindhu and Umadevi, 2013). Their location within quartz, immediately next to the electrum grain boundary, could imply an association with electrum. Experiments by Rivas et al. (2000), preparing Ag-coated Au and Au coated-Ag nanoparticles, show that when a colloid containing both metals is produced, two different types of nanoparticles can be produced depending on the Au:Ag ratios. They show that with a Au:Ag ratio of 54:46, separate Au and Ag nanoparticles are formed, while at a higher ratio (85:15), composite bimetallic nanoparticles are produced. It is possible that with the electrum ratios at Brucejack, two separate phases of nanoparticles may have formed, thus providing a source for the observed Ag nanoparticles. Additionally, recent work by Burke (2016) suggests leaching of Ag from electrum due to its higher solubility (e.g., Krupp and Weiser, 1992), may deposit Ag particles near the edge of electrum. Samples where this occurs show a corresponding Ag depletion near the edge of the electrum grains (Burke, 2016). However, electrum analyzed at Brucejack is shown to have a constant Au:Ag ratio (Figure 3.19b). This analysis however took place where there were no Ag nanoparticles and further analysis of regions where these nanoparticles are present may help determine their origin.

Electrum was directly observed to be made up of nanoparticles at one location where high resolution imaging was made in an area of the foil thin enough to to discern electrum nanopartices. High resolution bright-field observations of other electrum masses (Figure 3.21) were made at locations where the foil was too thick and individual particles could not be isolated. However, there are several other observations of electrum at Brucejack that could indicate that it exists as an aggregation of nanoparticles. These include: dendritic electrum mineralization, differing crystallographic orientation within electrum masses, botryoidal electrum surfaces, and nanoscale electrum rods.

Dendritic electrum mineralization

Dendritic electrum has been described in natural examples and cited as evidence for colloidal Au transport in epithermal vein deposits (Figure 1.3c; Schoenly and Saunders, 1993; Saunders and Schoenly, 1995; Saunders, 2012). These authors conclude that branching fractal networks represent the pattern of aggregation of Au nanoparticles. That is, if Au nanoparticles are present, they will coagulate in a predictable dendritic manner, and that due to its fractal nature, this geometry will be represented at larger scales (Weitz and Oliveria, 1984; Weitz et al., 1985; Lin et al., 1989). Hand specimens (Figure 1.1), in-situ electrum (Figures 3.8, 3.9, 3.10a), and thin sections (Figure 3.16) show a distinct branching pattern of electrum within quartz-carbonate vein samples. The presence of this texture could therefore be used as evidence for precious metal nanoparticle coagulation from a sol; however, several observations are inconsistent with this hypothesis. Firstly, optical microscopy shows that dendritic electrum is located within interstitial space between quartz grains (Figure 3.16b, c, e, f). Some of the observed grain boundaries between quartz and electrum are straight with distinct corners that resemble either intersections between quartz crystals (Figure 3.16f, 3.21). This suggests that this pattern is controlled by quartz and not the dendritic coagulation of Au nanoparticles. Also, the quartz-carbonate vein stockwork at Brucejack has seen at least one phase of deformation (Board and McNaughton, 2013; Jones, 2013) that has faulted and folded quartz-carbonate veins (e.g., Figure 3.3, 3.4a, 3.7). Fractal dendritic networks of electrum would be deformed during this tectonic history. Evidence of this occuring at Brucejack exists in the form of electrum flattened into foliation (Figure 3.10b) and electrum that has been smeared along fault planes (Figure 3.11). If amorphous silica was co-precipitated with Au as hypothesized, then recrystallization into quartz would also alter electrum textures (Herrington and Wilkinson, 1993). These factors indicate that there is a possibility that the observed dendritic networks observed at Brucejack are not primary textures and therefore do not inform the question of nanoparticle deposition. Nevertheless, dendritic electrum is ubiquitous within high-grade Au samples at Brucejack, except where electrum has been visibly deformed (Figure 3.10b, 3.11) or it is within a clast (Figure 3.4c, 3.7a), and it may indicate that before recrystallization, a similar precursor texture existed.

Crystallographic orientation

Figure 3.21c, e show dark-field and bright-field TEM images of the same location, and depicts electrum as non-homogenous masses with varying brightness when contrasted to most of the neighbouring quartz. Bright-field TEM images are a function of the percentage of incident electron beam that is transmitted through the sample. Contrast changes may indicate a change in composition or a change in crystal complexity due to dislocations or grain boundaries (e.g., Roig et al., 1998). The changes in the bright-field image are most pronounced close-to and parallel-with the electrum-quartz boundary and are interpreted to be caused by changes in thickness or deformation as a result of proximity to this boundary. There are however, small contrasts within the centre of the electrum mass which would not be affected by this. Dark-field TEM shows a clearer contrast within the electrum, representing changes in crystallographic orientation, that is pronounced throughout the entire sample (Figure 3.21c). The observation of 5-20 nm bright spots with irregular to spherical shapes are evidence that this mass is an aggregation of individual particles (e.g., Pearce et al., 2015a), instead of a single grain.

Botryoidal surfaces

Optical microscopy, and SEM imaging of electrum-bearing quartz-carbonate from Brucejack shows that a tortuous interface commonly appears along segments of the electrum-quartz grain boundary. Botryoidal textures, are observed in natural Au samples using SEM, and are thought to be an aggregation of Au nanoparticles (e.g., Figure 1.3a, 5.1a; Herzig et al., 1993; Hough et al., 2011; Reith et al., 2012). Botryoidal surfaces of supergene Au grains imaged by Reith et al. (2012) have embayments and protrusions on the scale of $\sim$1 μm with even smaller spherical protrusions ($\sim$100 nm) located on the larger protrusions (Figure 5.1a). Some of the embayments and pits within these samples are explained to come from Au dissolution (Figure 5.1a; Reith et al., 2012). These scales are very similar to the tortuous grain boundaries between quartz and electrum in the sample from Brucejack (Figures 3.16e, f, 3.18c). Though these also may be from dissolution of electrum or quartz, the similarities between these grain boundaries could provide some evidence that these electrum masses are

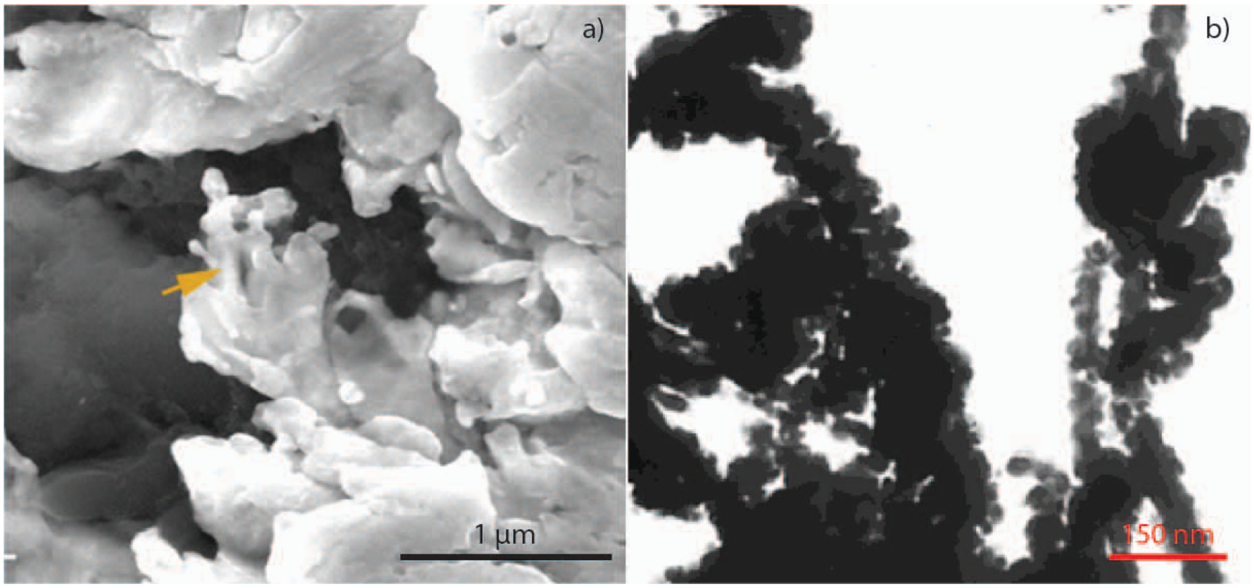

Figure 5.1 a) Botryoidal texture and dissolution texture of Au grains comprised of nanoparticles from stream sediments near Arrowtown, Central Otago, New Zealand. Modifed from Reith et al. (2012). b) Laboratory produced Ag (with 0.3% Au) nanoparticle aggregation showing chains and rod like protrusions. Modified from Rivas et al. (2000).

composed of nanoparticles.

Electrum nanoparticle rods and chains

In addition to the natural aggregations of precious metal nanoparticles imaged by SEM, nanoparticles of Ag (with 0.3% Au) have been seen to assemble in rods or chains in the laboratory (e.g., Figure 5.1b; Rivas et al., 2000; Jana et al., 2001). TEM images of predominantly Ag nanoparticles rods show that they can be several 100 nm in length and 30-150 nm across (Figure 5.1b). TEM images of electrum-quartz grain boundaries from the Brucejack sample show mostly straight grain boundaries, which could be due to the location of the FIB foil. However at one spot, 200-300 nm long, 50-100 nm wide rods of electrum are visible (Figure 3.21d). These rods or protrusions have rounded edges and emanate from a larger electrum mass. Though they are not the same length of the chains of nanoparticles that are commonly synthesized in the lab, they are similar in size and shape to morphologies of Ag (Figure 5.1b) that are aggregation of nanoparticles. Also, close observation reveals a botryoidal texture with spherical particles being visible (Figure 3.21d) indicating that the rods and protrusions seen at Brucejack are composed of nanoparticles as well.

The observation of electrum masses made up of nanoparticles and of Ag nanoparticles near an electrum-quartz grain boundary indicates at least the presence of some precious metal nanoparticles within electrum-bearing quartz-carbonate veining at the Brucejack deposit. In addition to this, different crystallographic orientations within electrum masses, botryoidal surfaces of electrum, and the presence of nanoscale electrum rods also indicate that the larger electrum masses may be an aggregation of smaller nanoscale particles. This does not, however, show that Au/electrum has been transported in a suspension, as it may have precipitated from solution as nanoparticles in situ. As the stability of Au nanoparticles has been shown to be enhanced by the presence of a silica sol, an association between Au/electrum with amorphous silica may suggest that nanoparticles at least had the potential to be transported a significant distance within a hydrothermal system.

5.2 Structural traps

The depositional settings of the Brucejack and Dixie Valley sites were determined to validate the comparison between the two sites and to help establish how deposit structure plays a role in precipitating and/or trapping precious metal nanoparticles within epithermal deposits. Fluid flow within both deposits was channeled along faults and fractures associated with an extensional fault system, while at Brucejack, later stage veining is also localized along faults formed in a compressional setting. Visible electrum-bearing veins at Brucejack show no obvious structural traps at outcrop level, but extensional veining related to earthquake rupture, or hydrofracture may act as traps at the deposit scale.

5.2.1 Structural setting of quartz-carbonate vein stockwork

Map Area 1

The vein systems seen in map area 1 (Figure 3.1), and in the underground workings (Figure

3.4), of the Brucejack deposit show a textural relationship. Both show a (5-10 m wide) core zone with intense stockwork consisting of several generations of quartz-carbonate veins whose contacts are difficult to discern. Away from this core zone, vein intensity diminishes, with a sharper boundary observed on the north contact (footwall) of the core stockwork. To the south, large, steeply dipping veins with associated stockwork are spaced centimetres to decimetres apart within a region up to 20 m away from the core, in the hanging wall of the stockwork system. These large parallel veins can be seen close to the south contact (hangingwall) of the core zone in both the ~80 m long (strike-parallel) surface map and the ~15 m long (dip-parallel) underground exposure. Measured vein orientations underground and on surface, however, are different (Figures 3.2b, 3.4b), with the underground veins showing a distinct southeast strike compared to the east-northeast strike of those in map area 1. Also, a direct projection of the Domain 20 stockwork system to surface (Pretium Resources Inc., unpublished data, 2015), using both drillhole intercepts and underground measurements, would lie 100 m to the south of map area 1. There is a distinct possibility that the two sites do not expose the same continuous vein system; they may be linked, however, via one of the following three scenarios:

a) The Domain 20 system could branch up dip, meaning that the stockwork seen in map area 1 may represent a northern branch of Domain 20 (Figure 5.2a).

b) To the east of map area 1, an extensive stockwork zone that extends both east and southeast (Figure 3.1) contains en échelon east-trending veins (Figure 3.1). This type of en échelon pattern may also extend downdip from map area 1, causing the stockwork system to step south downdip (Figure 5.2b).

c) The stockwork has been displaced along one or more north-verging thrust faults (Figure 5.2c). Figure 3.3a shows a steeply south-dipping reverse fault cutting the main stockwork zone of Domain 20 underground. Motion is deduced from tension gashes and offsets on tension gashes along a conjugate fault below the main through-going fault plane. Late north-verging thrust faults that could be related to formation of the Skeena fold-and-thrust belt have been mapped elsewhere in underground workings, on surface and using drillholes (Board and McNaughton, 2013; Jones, 2013). Combined northward heave of ~100 m on several of these faults between the outcrop and the exposures in the underground workings may result in an offset between the projected location of Domain 20 and the outcrop in map area 1 (Figure 5.2c).

A number of observations suggest that the stockworks of map area 1 and Domain 20 occupy fault/shear zones. The offset in rock units across the stockwork zone, and the similarities in geometry of the stockwork and surrounding zone of veining to fault-zone cores and damage zones described in the literature (e.g., Chester and Logan, 1986; Smith et al., 1990; Forster and Evans, 1991; Caine et al., 1996) are features that indicate stockwork veining formed along fault zones. In the case of the mapped outcrop, the massive composite quartz vein is the fault core and the surrounding steep veining is the damage zone, with veins appearing to follow fracture sets with apparent strike-slip Andersonian fault geometry (e.g., Caine et al., 2010). Figure 3.2a shows several areas (stations C03, C09, P10) where sets of steeply dipping conjugate veins may exist. Equal-area projection plots of poles to vein orientation from both the underground workings and the surface outcrop show predominantly steep veining, and

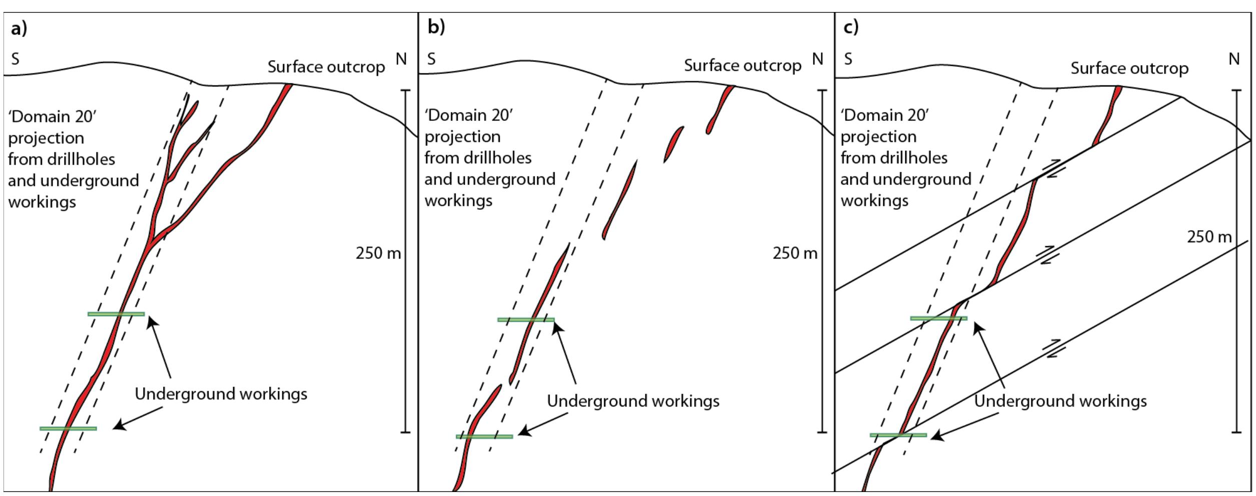

Figure 5.2 Schematic representation of the projection of Domain 20 from underground workings, drillhole intercepts and surface outcrop of stockwork to the north (map area 1), being offset by a) branching stockwork geometry, b) en échelon stockwork veining, or c) north-verging thrust faults.

the range in strike of these veins reflects varied damage-zone fracture geometry. At least one of the exposures of the Domain 20 stockwork system in the underground workings shows an abrupt contact between stockwork and wallrock on the north contact (the foot wall) of the main stockwork zone. On the south (hanging wall) contact, there is an extensive zone of less intense stockwork veining. Similarly, the north contact on the surface map displays a significant drop in stockwork-vein intensity (Figure 3.2a). Here, several large veins are mapped, but vein size and intensity are less than to the south, where 10-20 m of less intense stockwork veining is mapped.

These outcrop patterns show an asymmetry in veining about the core stockwork zone. Asymmetry in damage zones around faults due to asymmetric strain distribution can be a result of lithological or structural contrast across a fault zone (e.g., Aydin and Johnson, 1978; Antonellini and Aydin, 1995; Nelson et al., 1999; Mitra and Ismat, 2001; Clausen et al., 2003; Doughty, 2003; Berg and Skar, 2005). The orientation of the core stockwork zone and the majority of steep subsidiary veins (Figure 3.2b) in map area 1 strike northeast while the main trend of domain 20 on surface (Figure 3.1), and in the underground workings (Figure 3.4b) strike northwest. The core stockwork zone in map area 1 is also wider than other mapped stockwork. Both of these could be a result of core stockwork in map area 1 occupying a dilational jog explaining the different orientation and apparent increased extension. Exposures in the underground workings show areas of brecciation along the contacts of the core stockwork zone (Figure 3.4a, c) that could also be a result of faulting. Clasts within this breccia include quartz-carbonate vein and wallrock, indicating that the fault zone was active during the formation of stockwork vein systems such as Domain 20.

Although the overall geometry of the stockwork in map area 1 is suggestive of shear offset, many of the veins within the stockwork do not show measurable offset across them and are interpreted as opening-mode veins. Syntaxial quartz growth indicates open-space quartz crystallization, which may be evidence of supra-lithostatic fluid pressure (Wilson, 1994; Bons et al., 2012). This syntaxial texture is seen in all orientations of veins, including subhorizontal veins, further supporting the suggestion of (at least transient) extremely high pore pressure. As most of the quartz is syntaxial and euhedral, and there is a lack of observable, consistent offset across veins, it is deduced that quartz-crystal growth did not occur during periods of major slip along faults. Much of the quartz precipitation occurred during periods of static high fluid pressure between slip and fracturing events, or within pressurized fracture networks in the damage zone of the fault. However, cryptocrystalline quartz within some vein cores may also indicate that rapid silica precipitation occurred during changes in temperature or pressure caused by seismic events. As there are many cross-cutting relations between isolated veins, large composite veins and vein breccias containing clasts of quartz-carbonate vein material (including electrum-mineralized veins), it is also deduced that the formation of stockwork veining occurred during multiple seismic events. These seismic events must predate later Cretaceous transpression during emplacement of the Skeena fold-and-thrust belt as stockwork veining is cross-cut by later thrust faults.

Map Area 2

The overall geometry of the main stockwork system, the abundance of faults, macroscopic quartz vein textures, and the host rocks all indicate that much of the stockwork veining mapped in map area 2 contrasts with that which is mapped in map area 1.

Map area 2 (Figure 3.5) contains stockwork veining with an overall northwest strike that is similar to several other stockwork vein systems seen at surface at the Brucejack deposit (Figure 3.1). The overall strike of the veins is also similar to veins in the exposure of Domain 20 in the underground workings (Figure 3.4b, 3.5). One of the reasons the overall trend of this stockwork is different than map area 1 is that map area 2 is not located within a en-échelon segment of the overall stockwork zone; instead it is parallel with the larger map-scale trend (Figure 3.1). The equal-area stereo net in Figure 3.5 shows a high concentration of northwest striking veins that dip steeply to the northeast. This orientation also coincides with electrum-bearing layered quartz-carbonate vein sets mapped within the Brucejack underground workings not associated with Domain 20 (Figure 3.10; Pretium Resources Inc., unpublished data 2015) and thus may be related to these vein sets.

No quartz-carbonate veins >1 m wide and extending along strike for any significant distance (> 5 m) occur within map area 2. Nor is there a major central core of quartz-carbonate stockwork veining. This suggests that this stockwork veining did not form along a major fault-zone with high permeability like that in map area 1. Instead, this could indicate the fractures and subsequent veining in map area 2 were due to more distributed strain over a wider area. Strain localization is known to occur as a fault matures or as strain rate decreases (Meyer et al., 2002; Walsh et al., 2003). The lack of: a major >5 m wide stockwork core within map area 2, large zones of stockwork breccia, and large subsidiary veins mapped outside the main stockwork core, may indicate that veining here did not form within a major fault zone with large displacement. However, there are indications that many of the observed veins are related to shear.

Thirteen faults with orientations were mapped and measured within map area 2 and unlike map area 1, many of the veins in the area exhibited textures indicating formation during shear (Figure 3.6a, b). This indicates that a significant amount of vein formation within this outcrop occurred during fault movement. Ribbon quartz and undulose extinction, seen in thin section (Figure 3.17), as well as slickenfibres and S-fabrics seen in outcrop (Figure 3.6a, b), indicate that these veins were not opening mode alone (e.g., Hodgson, 1989; Bons et al., 2012). This could be the reason behind lesser vein widths in this outcrop area. Tension gashes and slickenline orientations indicate that the major thrust faults in map area 2 show, top-to-the north vergence with several conjugate thrusts also observed. This vergence correlates with thrust faults seen in the underground working of Brucejack that cross-cut electrum-bearing stockwork such as Domain 20 (Figure 3.4a). Consequently, it is assumed that the thrust faults within map area 2 coincide with the same compressional deformation that lead to similarly oriented thrust faulting in the underground workings. This would indicate that all of the fault related veins seen in map area 2 are classified as vein generation 4, which post-dates electrum mineralization.

Although many of the veins are associated with thrust motion and oblique slip, they probably overprint earlier electrum-bearing stockwork veining. Drilling has recovered significant Au grades within quartz-carbonate veins within and adjacent to map area 2 (Pretium Resources Inc., unpublished data, 2015). As much of the observed veining is related to later fault slip, the structural setting of this map area should not be used as the structural setting for electrum-bearing stockwork vein emplacement. Instead, as the electrum bearing vein phases are documented to contain opening mode textures such as syntaxial comb quartz, and some are related to wide fault zones (map area 1), a structural setting with horizontal extension is required. Even if hydrofracture and/or extreme pore pressure are responsible for mode 1 fractures, these would be oriented horizontal in a compressional setting (i.e., σ_3 is vertical). Across the VOK zone, steep veins strike east-northeast (Map area 1, Figure 3.1b), or northwest (Map area 2 and domain 20, Figure 3.5b and 3.4b). Assuming Andersonian faulting, this indicates that apparent extensional axis was horizontal and in a north-northeast to northeast direction and that σ_3 is also in these directions. As Meyer et al. (2002) and Walsh et al. (2003) note, strain becomes more localized during a fault zone's evolution. As Domain 20 contains brecciated clasts of electrum-bearing quartz-carbonate, it may represent the later localized fault zone in an extensional setting. More widely spaced, smaller, ribbon veins with primary, in situ electrum deposition, may represent opening mode cracks forming earlier on in an extensional setting when strain was more distributed.

Dixie Valley comparison

The general structural setting of electrum bearing quartz-carbonate vein stockwork at Brucejack is similar to that of Dixie Valley. Power and Tullis (1989); Vikre (1994); Caine et al. (2010) show that quartz and quartz-carbonate veining at the Mirrors locality and the Dixie Comstock mine was emplaced during extension. Both of the locations of Domain 20, shown in map area 1 and the underground workings at Brucejack (Figure 3.1a, 3.4a), and the Dixie Comstock mine (Figure 2.3), are at jogs on a major fault zone. These could be dilational jogs allowing for increased extension and permeability. Observations of fault zones with a distinct fault core with slip surfaces (Figure 4.1), and damage zone at the Mirrors, as well as recycled quartz-carbonate breccias at the Dixie Comstock mine are consistent with their setting within a major fault zone (Power and Tullis, 1989; Vikre, 1994; Caine et al., 2010). Silica altered breccia clasts, with radial comb quartz growth rims, and later interstitial carbonate is common to the Dixie Valley locations as well as Brucejack. Similar fluid inclusion homogenization temperatures from different quartz and calcite stages at Dixie Comstock (160°-210° C, Vikre, 1994) and Brucejack (∼160° C, Tombe, 2015), confirm similar environment at least in temperature and potentially depth of the hydrothermal systems. Different mineral phases, such as barite, seen at Dixie Valley, could reflect a purely meteoric origin of hydrothermal fluids (Vikre, 1994). Although similar quartz phases are present at Dixie Valley and Brucejack, Vikre (1994) show that the majority of the Au was deposited within the initial stage of hydrothermal mineralization. High-grade Au at Brucejack is located within the centre of veins commonly with syntaxial comb quartz separating it from the wallrock. This suggests that very high-grade electrum at Brucejack was not deposited in the initial hydrothermal phase. Electrum associated with pyrite (Figure 3.18a, b) could be within the initial phase and this suggests that Dixie Comstock and Brucejack may have similar precursor systems. Very high-grade Au mineralization is however absent at Dixie Comstock and therefore there may be no need for a colloidal transport model there to explain observed Au grades.

5.2.2 Timing and setting of electrum deposition

Examination of electrum mineralization in the underground workings of the Brucejack deposit does not show that it occurs within any one type of vein orientation or within dilational jogs. Subsequently there are no recognized, consistent specific high-grade electrum deposition settings across the deposit. Two types of electrum occurrences are observed, one that is primary within the vein (~78% of occurences), and the other as recycled, brecciated electrum-bearing quartz-carbonate clasts that are seen in Domain 20. The latter of these settings does not provide insight into the structural setting of electrum deposition as it was inherited from older vein systems that have been reworked into the present vein geometry. Therefore, deducing the original setting of electrum precipitation in these cases is not possible. However, examination of electrum deposited *in situ* in quartz-carbonate veins does reveal important information.

All of the electrum bearing veins contain syntaxial quartz growth, and in most cases (10 out of 11 documented primary occurrences underground), a layer of syntaxial comb quartz separates the electrum bearing phase of the vein from the wallrock. Here, two cases are possible: electrum is only deposited in a later phase of veining, or that the barren syntaxial quartz growth is a result of amorphous silica recrystallization with nucleation on the wallrock. The former case represents a crack-seal mechanism for vein formation from fracturing and subsequent mineral precipitation/deposition events (e.g., Ramsay, 1980; Urai et al., 1991; Bons et al., 2012). In the case of Brucejack, where at least one layer of elongate-blocky quartz separates the electrum from the wallrock, at least one prior fracturing event is required before the onset of electrum mineralization. If the syntaxial quartz was a result of recrystallization nucleating on the wallrock, then a single fracturing event and subsequent depressurization may have formed an amorphous phase and recystallization into quartz towards the centre of the vein would push any impurities towards the centre.

In the instance that electrum is in contact with the wallrock (Figure 3.9), the electrum-bearing vein cross-cuts an earlier pyrite vein (vein 0). In this case electrum deposition may have occurred due to the charge of pyrite. Pyrite is usually a n-type semiconductor but when it contains As (arsenian pyrite) it switches from a n-type to a p-type semiconductor (e.g., Bockris and Reddy, 1973; Möller and Kersten, 1994). The most important difference between these two semi-conductors is that a positive charge density accumulates on the contact of a p-type while a negative charge density accumulates on the contact of a n-type (Möller and

Kersten, 1994). Experimental work by Möller and Kersten (1994) show that Au grains also accumulate on the surface of p-type semiconductors from a fluid containing Au in solution and as a colloid. Recent wavelength-dispersive spectroscopy (WDS) measurements show that zones of pyrite at Brucejack contain up to ~3.3 weight % As (D. McLeish, personal communication, July 10, 2016). This would enable pyrite to act as p-type semiconductor allowing Au nanoparticles with a negative surface charge (e.g., Frondel, 1938; Saunders, 1990) to adhere to pyrite that is cross-cut by fractures containing hydrothermal fluids with colloidal Au. Electron flow from the p-type semiconductor to the Au may then allow the Au grain itself to attract more Au nanoparticles.

Instances of electrum mineralization being cross-cut by later syntaxial quartz-carbonate veining (Figure 3.8) indicate that the mineralization was not a later isolated event. Instead, the electrum mineralization is considered to have formed both early in the development of the stockwork (as it exists within clasts in Domain 20), and coeval with the stockwork development. Faults and quartz-carbonate filled fractures associated with visible shear (e.g., Figure 3.4a, 3.7, 3.8, 3.11) cross-cut and deform visible electrum bearing quartz veins, confirming compressional deformation post dates observed electrum mineralization.

The goal of determining whether there are specific local structural traps for nanoparticle accumulation was not met. Either these structural traps are on a larger scale than what could be observed in underground exposure, or another mechanism for the concentration of Au nanoparticles must be invoked in order to achieve such localized high concentrations. However, an extensional structural setting was determined for electrum bearing quartz-carbonate stockwork veining at Brucejack. Large stockwork systems are a result of hydrothermal fluid flow and vein precipitation within larger stockwork systems (e.g., Domain 20) and likely post-date earlier veining containing primary high-grade electrum mineralization. These earlier veins are more dispersed and are interpreted to form during mode 1 fracturing during early development of faults within an extensional setting when strain was more distributed. Mode 1 fracture and depressurization may have acted as a deposit scale trap for Au nanoparticles.

5.3 Amorphous silica

Finding amorphous silica at Brucejack is complicated by the fact that it will have recrystallized to quartz over the deposits ~180-190 million year old geologic history. Textures indicating that quartz had an amorphous precursor phase must be established. The observations made at Dixie Valley are specifically used in order to compare quartz textures of a site with known amorphous silica deposition with those of Brucejack.

5.3.1 Dixie Valley

At the Mirrors locality in Dixie Valley, amorphous silica has been observed on the Mirrors slip surface (Figure 1.5; Rowe et al., 2012). The formation of the (now mostly quartz) slickensides is debated, with Power and Tullis (1989) preferring continuous, low strain deformation, while Caine et al. (2010) prefers pressure drop due to coseismic dilatancy and supersaturation of fluids. Another possibility is that pre-existing quartz on the slip surface was amorphosed and formed a gel during slip due to friction (Hayashi and Tsutsumi, 2010; Bestmann et al., 2012; Nakamura et al., 2012; Kirkpatrick et al., 2013). While the mechanism described by Caine et al. (2010) explains the formation of amorphous silica within mode 1 fractures in the footwall of the Mirrors, the friction model is a more suitable explanation for amorphous silica formation on the fault plane itself. Silica on the fault plane may have a hydrothermal source, but the orientation of the plane does not lend itself to dilation and depressurization which would cause precipitation of an amorphous phase. Instead, it lends itself to the frictional amorphization of pre-existing hydrothermal or primary quartz. The quartz CPO networks (Figure 4.3a, b) within the vitreous quartz layer on the slip surface of the Mirrors (Figure 4.2) have planes that are aligned in a manner that is kinematically consistent with the slip observed on the Stillwater fault zone (SFZ). The Mirrors fault surface dips between 40°-55° in outcrop, ~5°-20° shallower than an ideal Andersonian normal fault (i.e., 60°-70°). Major planes of aligned CPO within the vitreous band of quartz which are 0°-15° steeper than the fault surface are at an orientation that better reflects an Andersonian faulting regime. This indicates that the stress field on the fault could have influenced the recrystallization of quartz, while the lack of displacement across these CPO planes, combined with a low abundance of dislocations within microcrystalline quartz grains (Figure 4.5a), could indicate that the quartz did not crystallize during a time of high strain rate (e.g., Kirkpatrick et al., 2013). Similar structures observed in the fault slip surface of the Corona Heights fault in San Francisco, California have been interpreted to form during recrystallization of a silica gel formed during fault slip (Kirkpatrick et al., 2013). This leads to the conclusion that the vitreous quartz on the slip surface at the Mirrors, where amorphous silica has been observed (Figure 1.5 Rowe et al., 2012), recrystallized from an amorphous silica gel formed by frictional wear of quartz on the fault slip surface.

Cryptocrystalline silica observed in tension gashes and more continuous veins in the immediate footwall to the Mirrors slip surface, could also represent precipitation of amorphous silica. Thin section observations of mosaic textures within microcrystalline quartz (Figure 4.3f) indicate very rapid precipitation of quartz and/or amorphous silica (e.g., Lovering, 1972; Williams et al., 1985; Saunders, 1990; Dong et al., 1995; Herdianita et al., 2000; Lynne et al., 2005; Lee, 2007). Caine et al. (2010)'s The model of amorphous silica formation put by coseismic dilatancy and pressure drop resulting in supersaturation of fracture filling fluids with respect to silica (Caine et al., 2010), would be a reasonable explanation for amorphous silica formation within mode 1 fractures. Microcrystalline quartz flow textures similar to those seen at the Dixie Comstock mine (e.g., Figure 4.4c, d), could also indicate the precipitation of an amorphous gel that had a chance to flow before it recrystallized to quartz.

Thin section observations at the Dixie Comstock mine also suggest amorphous silica formation. Evidence of quartz recrystallization from amorphous silica in the form of feathery extinction textures (e.g., Figure 1.4; Adams, 1920; Sander and Black, 1988; Dong et al., 1995) is seen in blocky quartz surrounded by syntaxial comb quartz (Figure 4.4b). The surrounding comb quartz can be interpreted to have grown towards open space (Bons et al., 2012), thus suggesting that the location of the feathery quartz may have represented a vug where an amorphous silica phase eventually precipitated. Microcrystalline quartz observed within veins and breccias at Dixie Comstock has flow textures (Figure 4.4c, d) similar to what is seen in veins at the Mirrors. As previously explained, this could also indicate the flow of previously precipitated silica particles in a gel before recrystallization to microcrystalline quartz.

Earlier work (Figure 1.5; Rowe et al., 2012) documents, and optical microscopy observations support, the presence of amorphous silica or quartz recrystallized from amorphous silica at Dixie Valley. More compelling evidence of its existence (i.e., relict textures) can be seen using electron microscopy. The ∼10 nm spheres seen in bright-field TEM images of microcrystalline quartz samples from the Mirrors slip surface and mode 1 veins and tension gashes in the footwall of the Mirrors (Figure 4.5b, c, d) resemble opal crystallites imaged by Graetsch (1994); Elzea and Rice (1996). Opal crystallites imaged by Elzea and Rice (1996) have diameters between 12-32 nm. Although this is slightly larger than what is seen at the Mirrors (∼5-15 nm, Figure 4.5b, c, d), the size ranges overlap. Non-crystalline opal phases have been described as stacked spheres of silica with water filling the interstitial spaces (silica gel) (Jones et al., 1964; Florke et al., 1973; Graetsch, 1994). Though the Mirrors samples are crystalline quartz, their possible precursor as a silica gel could lead to the relict textures visible in TEM images. The lighter interstitial spaces between the spheres now contain crystalline quartz that likely formed during dehydration of the silica gel or opal phase and recrystallization to quartz. A higher number of crystal defects within the recrystallized opal crystallites, or a higher density would result in the darker colour in bright-field imaging. These observations may provide insight into the process of opal dehydration and recrystallization to quartz with interstitial quartz crystallization nucleating on opal crystallites.

The presence of relict textures of opal crystallites within microcrystalline quartz at the Mirrors is good indicator of an amorphous precursor phase. It indicates that microcrystalline quartz in other samples with textures similar to those described in the samples from the Mirrors (Figure 4.3 a, b, f) also have recrystallized from an amorphous silica phase.

5.3.2 Brucejack

Although the quartz-carbonate stockwork veining at Brucejack has seen multiphase deformation and up to lower greenschist facies metamorphism, textures suggesting recrystallization from amorphous silica (e.g., Figure 1.4; Dong et al., 1995) are observed. Optical microscopy reveals two quartz textures shown in Figure 1.4 that may indicate recrystallization from a precursor amorphous phase. Those are feathery (Figure 3.15b, d), and mosaic (Figure 3.14a and 3.16a-d) quartz. Flamboyant extinction may also be present but its similarity to feathery extinction makes it difficult to distinguish. While ghost spheres have not been reported in thin section, distributions of inclusions and impurities that cross grain boundaries do exist. TEM observation of electrum bearing quartz-carbonate veins may indicate relict textures of opal crystallite spheres.

Phase A and phase B quartz (Table 3.1) contain grains with feathery extinction patterns (Figure 3.15b, d), a texture thought to form from the precipitation of amorphous silica on pre-existing quartz grains (Figure 1.4; Adams, 1920; Sander and Black, 1988; Dong et al., 1995). Dong et al. (1995) describes this texture as resulting from recrystallization of amorphous silica nucleating on the crystal resulting in small subgrains radiating away from the old grain boundary (delineated by inclusions). This would entail two phases of silica deposition, the first resulting in quartz crystals and then a later phase of amorphous silica precipitation. This would also suggest that feathery quartz would be fairly ubiquitous in samples where it is observed if both phases are present. This however is not the case as it can be completely surrounded by phase A and phase B quartz without this pattern. It is possible that only in a certain percentage of crystals, is the feathery extinction preserved, while most samples undergo complete recrystallization, or that it only exists where there was sufficient open space for later phase fluids to accumulate. In this case, quartz grains were formed in an earlier vein phase, then fractured providing space for a second phase of fluid flow and silica formation. Some evidence, such as feathery extinction, indicates that this second phase formed an amorphous silica phase. Recrystallization of the amorphous silica to quartz may have been aided by the presence of crystalline quartz, by providing a growth nucleation point (e.g., Okamoto et al., 2010), and the process resulted in coarse, blocky, phase A and phase B quartz.

Phase C and phase D quartz (Table 3.1; Figure 5.3a, b) both show microcrystalline mosaic textures that fit well with the description of mosaic quartz which is thought to be a product of recrystallization of massive chalcedony or amorphous silica (Figure 1.4; Lovering, 1972; Saunders, 1990; Dong et al., 1995). Similar textures are seen within microcrystalline quartz observed at the Mirrors outcrop in the extensional veins located in the footwall of the Mirrors fault slip surface (Figure 5.3c). Both examples have highly tortuous, interpenetrating quartz grain boundaries and complex extinction patterns and are associated with microcrystalline calcite and clay minerals (sericite at Brucejack, kaolinite at the Mirrors). Figure 5.3 shows that quartz grain sizes within the Brucejack samples are visibly larger, which may be a result of quartz at Brucejack being older, more deformed and altered, thus allowing for more recrystallization. Microcrystalline grains of calcite and clay minerals within the samples are randomly distributed, and if they are not a product of wallrock alteration, their small grain size and distribution suggests that they precipitated out of solution quickly and at the same time as silica. Inclusions within phase C quartz at Brucejack that overlap grain boundaries suggest they were trapped before the quartz grain boundaries were formed establishing that some recrystallization must have taken place. Also, micrometre-scale subgrains observed within larger phase C quartz grains suggests that the large grains are a product of recrystallization with the original extinction of the subgrain domain persisting (e.g., Dong et al., 1995). The observations that suggest quick precipitation and recrystallization are consistent with amorphous silica formation (e.g., Steefel and Van Cappellen, 1990; Okamoto et al., 2010). The similarities of the Brucejack phase C quartz with microcrystalline quartz from the Mirrors where relict opal crystallites have been observed also shows that there was an amorphous precursor phase for quartz.

Phase C and phase D quartz are usually observed to be a later phase within the quartz-

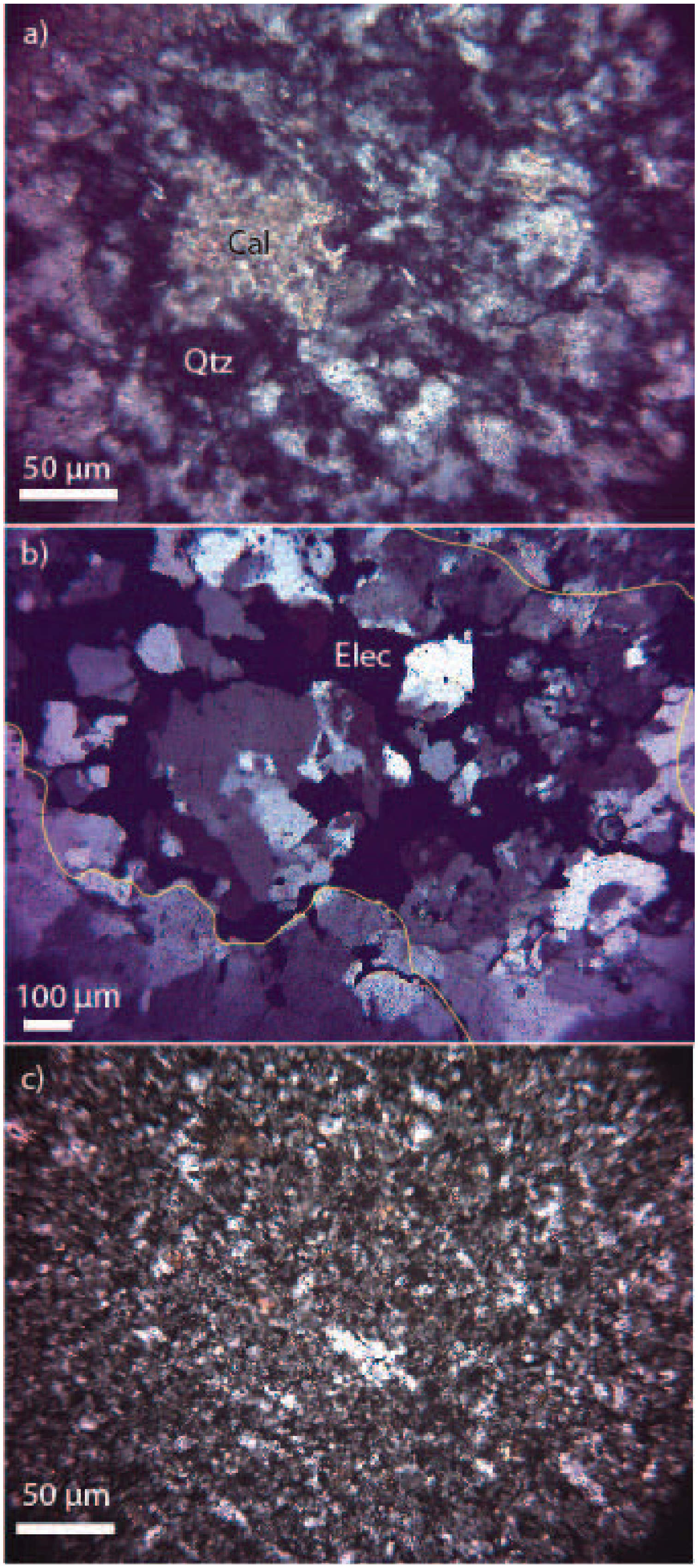

Figure 5.3 Comparison of microcrystalline quartz textures seen at the Mirrors and Brucejack. a) Phase C quartz (+ calcite + clay) from Brucejack showing a mosaic texture (e.g., Figure 1.4a Dong et al., 1995). b) Phase D quartz (+ calcite) within the yellow outline from Brucejack with associated electrum (Elec). Boundaries here show similar mosaic texture but grain size is larger than phase C quartz. c) Microcrystalline quartz (+ calcite + clay) from an extensional vein in the footwall of the Mirrors slip surface showing mosaic texture and much smaller grain size than phase C and D quartz from Brucejack. This quartz contains relict silica spherules inidcating it recrystallized from an amorphous phase.

carbonate veins at Brucejack. Phase C quartz was observed in vugs within breccias and small dilational sites where phase A quartz separated it from the wallrock or clasts (e.g., Figure 3.13c). Electrum associated phase D quartz was also usually separated from the wall rock by phase A or B quartz (Figure 3.8, 3.10a, c, 3.16b, d). Electrum does come in contact with wallrock in Figure 3.9, however, no samples were taken here for thin section analysis so it could not be determined if the phase D quartz here was also in contact with wallrock. This could imply that the microcrystalline quartz (phase C and D) is a later phase of veining at Brucejack, filling vugs, interstitial spaces and the centre of pre-existing veins, where dilation induced depressurization (e.g., Weatherley and Henley, 2013), may have induced silica super-saturation.

Electrum associated with phase D quartz may have aided in the recrystallization of amorphous silica. This could establish a connection between electrum and amorphous silica at Brucejack, as Pol et al. (2003) shows that Au nanoparticles adhered to silica grains would increase recrystallization rate and potentially drive the growth of larger crystals. This may be the reason that phase D quartz tends to have a larger grain size where it is associated with larger masses of dendritic electrum (Figure 5.3b).

Relict spheres seen in TEM images of quartz adjacent to electrum (Figure 3.21b) could be similar to the relict opal crystallites observed in microcrystalline quartz at the Mirrors outcrop. They are, however, much smaller (2-3 nm) and much less consistently spaced, not resembling the opal packing as closely as the Mirrors samples. This could be due to relict textures being increasingly obscured through deformation and metamorphism within the much older Brucejack samples. Dark-field imaging of quartz adjacent to electrum shows some areas where crystal lattice structures differ on the scale of a few-nm (Figure 3.21c). This also could be a result of a relict nanoparticles within quartz. The textural evidence from electron microscopy is not ubiquitous throughout observed microcrystalline quartz and could be obscured by recrystallization. However, these textures combined with previously discussed textures observed in thin sections using optical microscopy, suggest that microcrystalline quartz associated with electrum at Brucejack did initially exist as amorphous silica.

5.4 Colloidal tranport model

The observations made on samples, outcrop, and underground exposure of electrum bearing quartz-carbonate stockwork help answer the questions posed in the introduction and establish whether colloidal transport of Au, or electrum, aided in the formation of very high-grade Au mineralization at Brucejack. Although no local specific structural setting for instances of visible very high-grade Au can be seen at Brucejack, a setting where stockwork veining is hosted within faults and fractures seeing multiple slip events is established. Analysis of opening mode veins indicates that the tectonic setting had a major extensional component in a N-S direction. Secondly, by comparing evidence of quartz recrystallization from an amorphous silica phase at Mirrors outcrop in Dixie Valley, Nevada, with vein textures at Brucejack, quartz that is related to electrum (phase D) is likely to have recrystallized from an amorphous silica phase. The association of amorphous silica with electrum allows for a method of trapping Au nanoparticles during rapid silica precipitation, and it also offers a more efficient transport method as a silica-protected Au sol (e.g., Frondel, 1938). Lastly, the observation of electrum within quartz-carbonate veins at Brucejack reveals that large dendritic electrum masses are agglomerations of individual nano-scale grains, or particles. These observations suggest that colloidal transport played a role in high-grade, concentrated Au mineralization at Brucejack. Colloidal transport, along with other transport mechanisms such as solution and vapour, therefore must be must be considered when developing deposit models for high-grade epithermal Au deposits.

Figure 5.4 shows the schematic model of colloidal Au transport envisioned for the Brucejack deposit. The numbers shown in the Figure 5.4a, b represent steps in temperature and Au solubility that will be discussed here. In Figure 5.4a, a magmatic intrusion within an arc provides an auriferous hydrothermal fluid source (e.g., Pereira and Dixon, 1971; Mitchell and

Bell, 1973; Sillitoe, 2000; Müller et al., 2002). Fluid flow towards surface may be channeled by pre-existing faults and fractures. At depth and high temperatures (#1, ~500°C), Au is complexed with Cl^- in solution and can be above 1000 ppb (Figure 5.4b; Williams-Jones et al., 2009), but as fluids drop in temperature towards 350°C (#2), solubility also dramatically drops. Figure 5.4b shows that after this point, Au solubility can either keep dropping or increase with a decrease in temperature due to a switch from Au being complexed with Cl^- to HS^- (Seward, 1973; Williams-Jones et al., 2009). Whether solubility drops or not is a function of the availability of sulphur within the hydrothermal fluid. If sulphur is lost due to the precipitation of sulphide minerals such as pyrite, solubility of Au will continue to drop. If no metals are available in the host rocks for sulphides to form, then S remains available for Au to complex with and the solubility of Au will increase with a drop in temperature (Figure 5.4b, #3; Williams-Jones et al., 2009). At Brucejack, where electrum bearing quartz-carbonate veins cross-cut earlier pyrite veins and QSP alteration (Table 2.1 Board and McNaughton, 2013; Jones, 2013; Tombe, 2015), early pyrite formation may have removed available Fe in the wallrock. This also occurs at nearby higher temperature porphyry deposits (Margolis, 1993; Febbo et al., 2015) indicating a constant [S] throughout the hydrothermal system. This would result in the hydrothermal system at Brucejack having a Au solubility minimum at ~350°C. Homogenization temperatures of ~160°C determined by Tombe (2015) indicate that veins likely formed at temperatures below this solubility minimum (#4). If this is the case, then Au may have precipitated from solution deeper within the hydrothermal system at this solubility minimum (Figure 5.4a, #2).

Precipitation of Au complexed with Cl^- at higher temperature may result in precipitation of nanoparticles at the Au solubility minumum (#2; e.g., Turkevich et al., 1951; Kimling et al., 2006; Ojea-Jiménez et al., 2010; Doyen et al., 2013; Wuithschick et al., 2015). These could then travel upwards with the hydrothermal fluids as a suspension before they coagulate, or, if silica nanoparticles are available, for longer distances as a silica-protected Au sol (Figure 5.4a, #3). Ag, which is present in the Brucejack, deposit can aid in the functionalization of

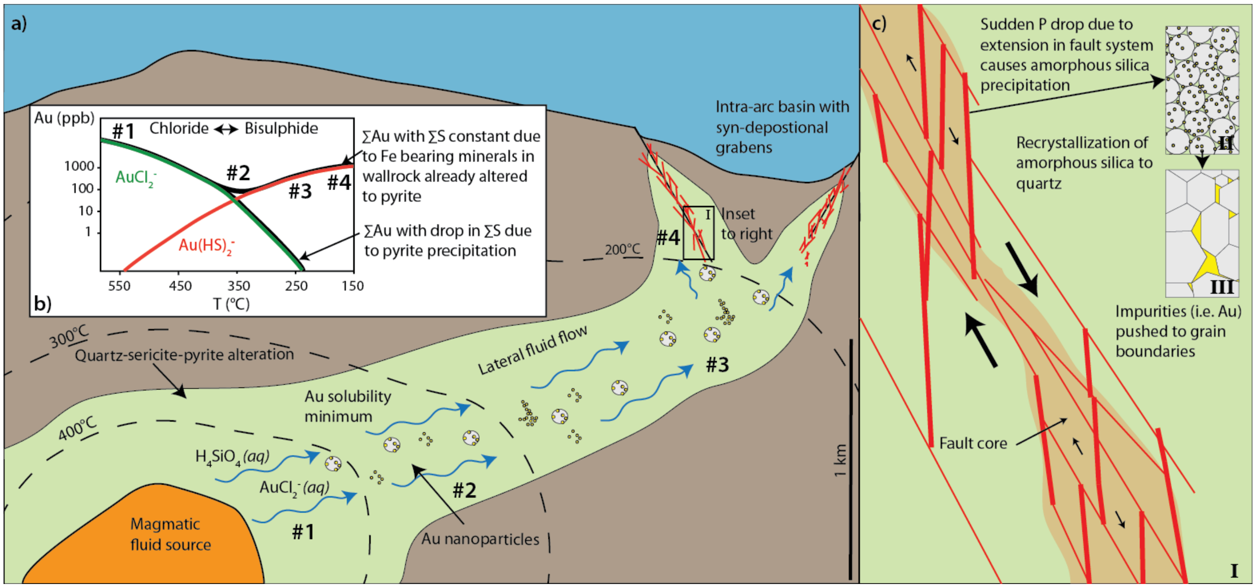

Figure 5.4 a) Schematic model of an auriferous magmatic hydrothermal system from intrusion to surface in an arc setting. Numbers 1-4 correlate to temperatures and Au solubilities shown in (b) and each step is discussed in detail in text. Depth of intrusion, temperature gradient, and location of quartz-sericite-pyrite (QSP) alteration estimated from (Margolis, 1993; Taylor, 2007; Sillitoe, 2010). b) Solubility of Au in hydrothermal fluids with a constant S content, and a drop in S content due to precipitation of sulphides. Adapted from (Williams-Jones et al., 2009). c) Schematic model of a major extensional fault system with dilational jogs representing the epithermal environment where the Brucejack deposit is located (I). Fault motion causes a sudden pressure drop and the precipitation of amorphous silica resulting in trapping of Au nanoparticle-coated silica particles (II). Recrystallization of amorphous silica to quartz pushes Au to grain boundaries (iii). See text for complete description of model.

silica spheres allowing Au nanoparticles to adhere to them (Lim et al., 2003; Kobayashi et al., 2005).

Earthquake rupture may also aid in adhering Au to silica nanoparticles. Pol et al. (2003), use sound waves of a certain frequency to generate free radicals from water molecules that trigger the reduction of $AuCl_4^-$ and precipitate amorphous gold that can adhere to a functionalized silica sphere surface. Earthquake slip has been shown to cause high-frequency shaking in the wake and the advance of propagating fault rupture tips (van der Elst et al., 2012). If there is earthquake rupture at depth, it can provide the depressurization necessary for amorphous silica formation, and high-frequency shaking may release p-waves at the right frequency to adhere Au to silica nano-spheres.

Structural analysis of the Brucejack deposit indicates that electrum bearing quartz-carbonate stockwork veining formed within active fractures and fault zones with multiple rupture events. Brucejack's location within submarine volcano-sedimentary strata of a island arc (e.g., Monger et al., 1982; Nelson and Colpron, 2007; Gagnon et al., 2012; Nelson and Kyba, 2014), indicate that the deposit could have formed within an intra-arc basin (Figure 5.4a). Here, dilational jogs could form within larger normal or strike-slip fault zones. Domain 20 (Figure 3.1a, 3.4a), and the Dixie Comstock mine (Figure 2.3), are both at dilational jogs on their respective fault zones. Earthquake rupture and slip on faults within these stockwork systems could cause the necessary increase in volume and depressurization for amorphous silica precipitation (e.g., Figure 5.4a(#4), c(I); Sibson, 1992; Micklethwaite et al., 2010; Weatherley and Henley, 2013). If there is any Au or Au-coated silica travelling in suspension, it will be trapped within amorphous silica veins (Figure 5.4c(II)). Subsequent recrystallization will force Au nanoparticles to quartz grain boundaries resulting in a dendritic mass of Au (e.g., Figure 5.4c(III); Herrington and Wilkinson, 1993). Also, if Au travelling in suspension cross-cuts an older pyrite vein, or area of pyrite mineralization within the host rock, Au nanoparticles may be attracted to pyrite as previously discussed. As electrum mineralization is occasionally seen where veins cross-cut pyrite (Figure 3.9), and immediately adjacent to pyrite grains within quartz-carbonate veining (Figure 3.18a, b), this could also play a minor role in the deposition of Au at Brucejack.

5.5 Further Research

Although this work establishes a model for colloidal Au transport and deposition, several of the observations made of electrum at Brucejack still need to be explained. First of all, only Au is taken into consideration when looking at solubility within a hydrothermal solution, but at Brucejack, Au is hosted in electrum, a solid solution of both Au and Ag. Ag behaves similar to Au in that it complexes with Cl^- at higher temperatures and HS^- at lower temperatures (e.g., Seward, 1976; Zotov et al., 1986; Gammons and Barnes, 1989; Gammons and Williams-Jones, 1995), and it also can form nanoparticles which can adhere to silica nanoparticles (e.g., Pol et al., 2002). Therefore, it could be that a similar process of colloidal transport is responsible for the Ag contained within electrum. Electrum itself has been shown to form nanoparticles (Guisbiers et al., 2015), but further work needs to be done on constraining how it forms and its stability.

The observation of electrum associated with pyrite within veins, and electrum precipitation where quartz-carbonate veins cross-cut earlier pyrite mineralization can be explained by adsorption or precipitation of Au onto arsenian pyrite. Figure 3.18b shows that the pyrite has different zonations. Elemental mapping showing As contents of these different zones could help understand the different phases of pyrite precipitation and their role in electrum deposition.

This work has shown that large dendritic electrum masses occur as an aggregation of nanoparticles. Their association with relict amorphous silica textures is evidence for colloidal transport, however, the distance at which they have been transported has not been established. Work by Kamenov et al. (2007); Saunders et al. (2008, 2015) using Pb, Re-Os, Cu, and S isotopes to determine whether precious metals were sourced from a different fluid than gangue minerals, is an example of a method that could be used at Brucejack. If electrum is shown to precipitate from different fluids than gangue minerals within the vein, it could be said they precipitated in a different location or under different conditions.

Finally, although colloidal transport can allow for a higher flux of Au though a hydrothermal system, the process of forming the extreme concentrations seen at the Brucejack deposit is still not well understood. Attraction and buildup of nanoparticles due to charge attraction to p-type semiconductor sulphide minerals is a potential way to localize nanoparticle deposition. However, most of the high-grade Au at Brucejack is not observed to cross-cut earlier pyrite mineralization. Therefore, another way to localize deposition of nanoparticles needs to be determined.

5.6 Conclusion

This thesis shows that there is a role for colloidal transport in the formation of high-grade Au, electrum bearing quartz-carbonate stockwork veining at the Brucejack Au-Ag deposit. The observations on the Brucejack deposit and the Stillwater fault zone at Dixie Valley, Nevada have shown that:

1. Major quartz-carbonate stockwork veining at Brucejack (Domain 20) and Dixie Valley formed along a major normal fault zones during multiple seismic events.

2. Electrum bearing quartz-carbonate veining at Brucejack was emplaced in mode 1 fractures during N-S extension.

3. Electrum bearing quartz-carbonate veining at Brucejack contains quartz with textures that are similar to those of quartz at Dixie Valley which has been shown to have recrystallized from an amorphous silica phase.

4. Observed dendritic masses of electrum constituting high-grade Au mineralization at Brucejack consist of an amalgamation of nanoparticles and are spatially related to quartz that recrystallized from an amorphous silica phase.

5. These observations have led to a depositional model for colloidal transport and deposition of high-grade Au within an epithermal Au deposits such as Brucejack. This model hypothesizes that Au nanoparticles precipitated deep within a hydrothermal system. Further work is required to test this hypothesis.

Bibliography

Adams, S. F., 1920. A microscopic study of vein quartz. Economic Geology 15, 623–664.

Antonellini, M., Aydin, A., 1995. Effect of faulting on fluid flow in porous sandstones: geometry and spatial distribution. AAPG bulletin 79 (5), 642–670.

Aydin, A., Johnson, A. M., 1978. Development of faults as zones of deformation bands and as slip surfaces in sandstone. In: Rock Friction and Earthquake Prediction. Springer, pp. 931–942.

Benedetti, M., Boulëgue, J., 1991. Mechanism of gold transfer and deposition in a supergene environment. Geochimica et Cosmochimica Acta 55 (6), 1539–1547.

Berg, S. S., Skar, T., 2005. Controls on damage zone asymmetry of a normal fault zone: outcrop analyses of a segment of the Moab fault, SE Utah. Journal of Structural Geology 27 (10), 1803–1822.

Bestmann, M., Pennacchioni, G., Nielsen, S., Göken, M., De Wall, H., 2012. Deformation and ultrafine dynamic recrystallization of quartz in pseudotachylyte-bearing brittle faults: A matter of a few seconds. Journal of Structural Geology 38, 21–38.

Bindhu, M., Umadevi, M., 2013. Synthesis of monodispersed silver nanoparticles using hibiscus cannabinus leaf extract and its antimicrobial activity. Spectrochimica acta part A: Molecular and biomolecular spectroscopy 101, 184–190.

Board, W., McNaughton, K., 2013. The Brucejack high-grade gold project, northwest British Columbia, Canada. In: Proceedings of NewGenGold Conference, November 26-27, Perth Australia. pp. 177–191.

Bockris, A., Reddy, J., 1973. Modern Electrochemistry. Vol. 2. Plenum Press, New York, pp. 1265–1350.

Bons, P. D., Elburg, M. A., Gomez-Rivas, E., 2012. A review of the formation of tectonic veins and their microstructures. Journal of Structural Geology 43, 33–62.

Boullier, A.-M., Robert, F., 1992. Palaeoseismic events recorded in Archaean gold-quartz vein networks, Val d'Or, Abitibi, Quebec, Canada. Journal of Structural Geology 14 (2), 161–179.

Bozkaya, G., Banks, D. A., 2015. The importance of supersaturated silica deposition for base-metal Au-Ag mineralisation in western Turkey. Turkish Journal of Earth Sciences 24 (2), 99–110.

Bridge, D. J., 1993. The deformed early Jurassic Kerr copper-gold porphyry deposit, Sulphurets gold camp, northwestern British Columbia. Master's thesis, University of British Columbia.

Burke, M., 2016. An electron microscopy investigation of gold and associated minerals from Round Mountain, Nevada. Master's thesis, Miami University - Oxford, Oxford, Ohio.

Caine, J. S., Bruhn, R. L., Forster, C. B., 2010. Internal structure, fault rocks, and inferences regarding deformation, fluid flow, and mineralization in the seismogenic Stillwater normal fault, Dixie Valley, Nevada. Journal of Structural Geology 32 (11), 1576–1589.

Caine, J. S., Evans, J. P., Forster, C. B., 1996. Fault zone architecture and permeability structure. Geology 24 (11), 1025–1028.

Chester, F., Logan, J., 1986. Implications for mechanical properties of brittle faults from observations of the Punchbowl fault zone, California. Pure and Applied Geophysics 124 (1-2), 79–106.

Clausen, J. A., Gabrielsen, R. H., Johnsen, E., Korstgård, J. A., 2003. Fault architecture and clay smear distribution. Examples from field studies and drained ring-shear experiments. Norwegian Journal of Geology/Norsk Geologisk Forening 83 (2).

Cox, S. F., 1995. Faulting processes at high fluid pressures: an example of fault valve behavior from the Wattle Gully Fault, Victoria, Australia. Journal of Geophysical Research: Solid Earth 100 (B7), 12841–12859.

Davies, A., Macdonald, A., Lewis, P., 1994. Stratigraphic and structural setting of mineral deposits in the Brucejack Lake area, northwestern British Columbia. In: Current Research 1994-A. Geological Survey of Canada, pp. 37–43.

Denton, J. M., Bell, E. J., Jodry, R. L., 1980. Geothermal reservoir assessment case study: northern Dixie Valley, Nevada. Tech. rep., Southland Royalty Co., Fort Worth, TX (USA). Natural Resources Dept.

Dong, G., Morrison, G., Jaireth, S., 1995. Quartz textures in epithermal veins, Queensland; classification, origin and implication. Economic Geology 90 (6), 1841–1856.

Doughty, P. T., 2003. Clay smear seals and fault sealing potential of an exhumed growth fault, Rio Grande rift, New Mexico. AAPG bulletin 87 (3), 427–444.

Doyen, M., Bartik, K., Bruylants, G., 2013. UV–Vis and NMR study of the formation of gold nanoparticles by citrate reduction: observation of gold–citrate aggregates. Journal of colloid and interface science 399, 1–5.

Elzea, J. M., Rice, S. B., 1996. TEM and X-ray diffraction evidence for cristobalite and tridymite stacking sequences in opal. Clays and Clay Minerals 44 (4), 492–500.

Erdmer, P., Cui, Y., 2009. Geological Map of British Columbia; BC Ministry of Energy, Mines and Petroleum Resources, Geoscience Map 2009-1, scale 1:1 500 000.

Evenchick, C. A., 1991. Geometry, evolution, and tectonic framework of the Skeena fold belt, north central British Columbia. Tectonics 10 (3), 527–546.

Evenchick, C. A., 2001. Northeast-trending folds in the western Skeena Fold Belt, northern Canadian Cordillera: a record of Early Cretaceous sinistral plate convergence. Journal of Structural Geology 23 (6), 1123–1140.

Evenchick, C. A., Gabrielse, H., Snyder, D., 2005. Crustal structure and lithology of the northern Canadian Cordillera: alternative interpretations of SNORCLE seismic reflection lines 2a and 2b. Canadian Journal of Earth Sciences 42 (6), 1149–1161.

Faber, C., Rowe, C. D., Miller, J. A., Fagereng, Å., Neethling, J. H., 2014. Silica gel in a fault slip surface: Field evidence for palaeo-earthquakes? Journal of Structural Geology 69, 108–121.

Fairbrother, L., Brugger, J., Shapter, J., Laird, J., Southam, G., Reith, F., 2012. Supergene gold transformation: Biogenic secondary and nano-particulate gold from arid Australia. Chemical Geology 320, 17–31.

Febbo, G. E., Kennedy, L. A., Savell, M., Creaser, R. A., Friedman, R. M., 2015. Geology of the Mitchell Au-Cu-Ag-Mo porphyry deposit, northwestern British Columbia, Canada. In: Geological Fieldwork 2014. No. 2015-1. British Columbia Ministry of Energy and Mines, pp. 59–86.

Florke, O., Jones, J., Segnit, E., 1973. The genesis of hyalite. Neues Jahrbuch fuer Mineralogie, Monatsh 2, 82–89.

Fonseca, J., 1988. The Sou Hills: A barrier to faulting in the central Nevada seismic belt. Journal of Geophysical Research: Solid Earth (1978–2012) 93 (B1), 475–489.

Forster, C. B., Evans, J. P., 1991. Hydrogeology of thrust faults and crystalline thrust sheets: Results of combined field and modeling studies. Geophysical Research Letters 18 (5), 979–982.

Fossen, H., 2016. Structural Geology: Joints and Veins, 2nd Edition. Cambridge University Press, Ch. 8, pp. 153–174.

Fournier, R., 1985a. The behavior of silica in hydrothermal solutions. Reviews in Econ. Geol. 2, 45–61.

Fournier, R. O., 1985b. Silica minerals as indicators of conditions during gold deposition. US Geological Survey Bulletin 1646, 15–26.

Frondel, C., 1938. Stability of colloidal gold under hydrothermal conditions. Economic Geology 33 (1), 1–20.

Gagnon, J.-F., Barresi, T., Waldron, J. W., Nelson, J., Poulton, T., Cordey, F., Colpron, M., 2012. Stratigraphy of the upper Hazelton Group and the Jurassic evolution of the Stikine terrane, British Columbia 1 1 ESS Contribution 20120051. Canadian Journal of Earth Sciences 49 (9), 1027–1052.

Gammons, C. H., Barnes, H., 1989. The solubility of Ag 2 S in near-neutral aqueous sulfide solutions at 25 to 300 C. Geochimica et Cosmochimica Acta 53 (2), 279–290.

Gammons, C. H., Williams-Jones, A., 1995. Hydrothermal geochemistry of electrum; thermodynamic constraints. Economic Geology 90 (2), 420–432.

Giannuzzi, L., Stevie, F. A., 1999. A review of focused ion beam milling techniques for TEM specimen preparation. Micron 30 (3), 197–204.

Giersig, M., Mulvaney, P., 1993. Formation of ordered two-dimensional gold colloid lattices by electrophoretic deposition. The Journal of Physical Chemistry 97 (24), 6334–6336.

Graetsch, H., 1994. Silica: physical behavior, geochemistry and materials applications: Structural characteristics of opaline and microcrystalline silica minerals. Vol. 29. Mineralogical Society of America, Ch. 6, pp. 209–232.

Guisbiers, G., Mendoza-Cruz, R., Bazan-Díaz, L., Velazquez-Salazar, J. J., Mendoza-Perez, R., Robledo-Torres, J. A., Rodriguez-Lopez, J.-L., Montejano-Carrizales, J. M., Whetten, R. L., Jose-Yacaman, M., 2015. Electrum, the gold–silver alloy, from the bulk scale to the nanoscale: Synthesis, properties, and segregation rules. ACS nano 10 (1), 188–198.

Hannington, M., Harðardóttir, V., Garbe-Schönberg, D., Brown, K. L., 2016. Gold enrichment in active geothermal systems by accumulating colloidal suspensions. Nature Geoscience 9 (4), 299–302.

Hardardóttir, V., Brown, K., Fridriksson, T., Hedenquist, J., Hannington, M., Thorhallsson, S., 2009. Metals in deep liquid of the reykjanes geothermal system, southwest iceland: Implications for the composition of seafloor black smoker fluids. Geology 37 (12), 1103–1106.

Hastings, D. D., 1979. Results of exploratory drilling northern Fallon Basin, western Nevada. Tech. rep., Rocky Mountain Association of Geologists and Utah Geological Association.

Hayashi, K.-I., Maruyama, T., Satoh, H., 2001. Precipitation of gold in a low-sulfidation epithermal gold deposit: insights from a submillimeter-scale oxygen isotope analysis of vein quartz. Economic Geology 96 (1), 211–216.

Hayashi, N., Tsutsumi, A., 2010. Deformation textures and mechanical behavior of a hydrated amorphous silica formed along an experimentally produced fault in chert. Geophysical Research Letters 37 (12).

Hedenquist, J. W., Henley, R. W., 1985. Hydrothermal eruptions in the Waiotapu geothermal system, New Zealand; their origin, associated breccias, and relation to precious metal mineralization. Economic Geology 80 (6), 1640–1668.

Heinrich, C. A., 2005. The physical and chemical evolution of low-salinity magmatic fluids at the porphyry to epithermal transition: a thermodynamic study. Mineralium Deposita 39 (8), 864–889.

Heinrich, C. A., Driesner, T., Stefánsson, A., Seward, T. M., 2004. Magmatic vapor contraction and the transport of gold from the porphyry environment to epithermal ore deposits. Geology 32 (9), 761–764.

Henderson, J., Kirkham, R., Henderson, M., Payne, J., Wright, T., Wright, R., 1992. Stratigraphy and structure of the Sulphurets area, British Columbia. Current research. Geological Survey of Canada, Paper, 323–332.

Herdianita, N., Browne, P., Rodgers, K., Campbell, K., 2000. Mineralogical and textural changes accompanying ageing of silica sinter. Mineralium Deposita 35 (1), 48–62.

Herrington, R., Wilkinson, J., 1993. Colloidal gold and silica in mesothermal vein systems. Geology 21 (6), 539–542.

Herzig, P. M., Hannington, M. D., Fouquet, Y., von Stackelberg, U., Petersen, S., 1993. Gold-rich polymetallic sulfides from the lau back arc and implications for the geochemistry of gold in sea-floor hydrothermal systems of the southwest pacific. Economic Geology 88 (8), 2182–2209.

Hintze, L. F., 1973. Geologic history of Utah. Vol. 20. Dept. of Geology, Brigham Young University.

Hodgson, C. J., 1989. The structure of shear-related, vein-type gold deposits: a review. Ore Geology Reviews 4 (3), 231–273.

Hough, R., Noble, R., Hitchen, G., Hart, R., Reddy, S., Saunders, M., Clode, P., Vaughan, D., Lowe, J., Gray, D., et al., 2008. Naturally occurring gold nanoparticles and nanoplates. Geology 36 (7), 571–574.

Hough, R., Noble, R., Reich, M., 2011. Natural gold nanoparticles. Ore Geology Reviews 42 (1), 55–61.

Iller, R., 1979. The chemistry of silica: solubility, polymerization, colloid and surface properties, and biochemistry. Wiley New York.

Jana, N. R., Gearheart, L., Murphy, C. J., et al., 2001. Seed-mediated growth approach for shape-controlled synthesis of spheroidal and rod-like gold nanoparticles using a surfactant template. Advanced Materials 13 (18), 1389.

Johnson, K., Nissen, E., Arrowsmith, J., McGarey, P., Scharer, K., Blisniuk, K., 2014. Rapid mapping of ultrafine fault zone topography with structure from motion. Geosphere 10 (5), 969–986.

Jones, I., December 2013. Pretium Resources Inc: Brucejack Project, Mineral Resource Update Technical Report, Effective Date - 19 December 2013; NI 43-101 report. Ni 43-101 report, Snowden Mining Industry Consultants.

Jones, J., Sanders, J., Segnit, E., 12 1964. Structure of opal. Nature 204 (4962), 990–991.

Kamenov, G. D., Saunders, J. A., Hames, W. E., Unger, D. L., 2007. Mafic magmas as sources for gold in middle Miocene epithermal deposits of the northern Great Basin, United States: evidence from Pb isotope compositions of native gold. Economic Geology 102 (7), 1191–1195.

Kastner, M., Keene, J., Gieskes, J., 1977. Diagenesis of siliceous oozes I. Chemical controls on the rate of opal-A to opal-CT transformationan experimental study. Geochimica et Cosmochimica Acta 41 (8), 1041–1059.

Kimling, J., Maier, M., Okenve, B., Kotaidis, V., Ballot, H., Plech, A., 2006. Turkevich method for gold nanoparticle synthesis revisited. The Journal of Physical Chemistry B 110 (32), 15700–15707.

Kirikham, R., Margolis, J., 1995. Overview of the Sulphurets area, northwestern British Columbia. In: Porphyry Deposits of the Northwestern Cordillera of North America. Vol. 46. Canadian Institute of Mining, Metallurgy and Petroleum, pp. 473–483.

Kirkham, R., 1992. Preliminary geologic map of the Brucejack Creek area, British Columbia, Geological Survey of Canada, Open File 2550, scale 1:5000.

Kirkpatrick, J., Rowe, C., White, J., Brodsky, E., 2013. Silica gel formation during fault slip: Evidence from the rock record. Geology 41 (9), 1015–1018.

Kobayashi, Y., Tadaki, Y., Nagao, D., Konno, M., 2005. Deposition of gold nanoparticles on silica spheres by electroless metal plating technique. Journal of colloid and interface science 283 (2), 601–604.

Krupp, R., Seward, T., 1987. The Rotokawa geothermal system, New Zealand; an active epithermal gold-depositing environment. Economic Geology 82 (5), 1109–1129.

Krupp, R., Weiser, T., 1992. On the stability of gold-silver alloys in the weathering environment. Mineralium Deposita 27 (4), 268–275.

Lee, D. R., 2007. Characterisation and the diagenetic transformation of non-and microcrystalline silica minerals.
URL http://www.geos.ed.ac.uk/homes/s0789516/microsilica.pdf

Lim, Y. T., Park, O. O., Jung, H.-T., 2003. Gold nanolayer-encapsulated silica particles synthesized by surface seeding and shell growing method: near infrared responsive materials. Journal of colloid and interface science 263 (2), 449–453.

Lin, M., Lindsay, H., Weitz, D., Ball, R., Klein, R., Meakin, P., 1989. Universality of fractal aggregates as probed by light scattering. In: Proceedings of the Royal Society of London A: Mathematical, Physical and Engineering Sciences. Vol. 423. The Royal Society, pp. 71–87.

Lloyd, G. E., 1987. Atomic number and crystallographic contrast images with the SEM: a review of backscattered electron techniques. Mineralogical Magazine 51 (359), 3–19.

Lovering, T. G., 1972. Jasperoid in the United States; its characteristics, origin, and economic significance. Tech. rep., US Govt. Print. Off.,.

Lynne, B. Y., Campbell, K. A., Moore, J., Browne, P., 2005. Diagenesis of 1900-year-old siliceous sinter (opal-A to quartz) at Opal Mound, Roosevelt Hot Springs, Utah, USA. Sedimentary Geology 179 (3), 249–278.

Margolis, J., 1993. Geology and intrusion-related copper-gold mineralization: Sulphurets, British Columbia. Ph.D. thesis, University of Oregon, Eugene, Oregon.

Marinova, I., Ganev, V., Titorenkova, R., 2014. Colloidal origin of colloform-banded textures in the Paleogene low-sulfidation Khan Krum gold deposit, SE Bulgaria. Mineralium Deposita 49 (1), 49–74.

McNaught, A., Wilkinson, A., 2006. Compendium of Chemical Terminology, 1997. Online corrected version.

Meyer, V., Nicol, A., Childs, C., Walsh, J., Watterson, J., 2002. Progressive localisation of strain during the evolution of a normal fault population. Journal of Structural Geology 24 (8), 1215–1231.

Micklethwaite, S., Sheldon, H. A., Baker, T., 2010. Active fault and shear processes and their implications for mineral deposit formation and discovery. Journal of Structural Geology 32 (2), 151–165.

Mikhlin, Y. L., Romanchenko, A. S., 2007. Gold deposition on pyrite and the common sulfide minerals: an STM/STS and SR-XPS study of surface reactions and Au nanoparticles. Geochimica et Cosmochimica Acta 71 (24), 5985–6001.

Mikucki, E. J., 1998. Hydrothermal transport and depositional processes in Archean lode-gold systems: a review. Ore Geology Reviews 13 (1), 307–321.

Mitchell, A. H., Bell, J., 1973. Island-arc evolution and related mineral deposits. The Journal of Geology, 381–405.

Mitra, G., Ismat, Z., 2001. Microfracturing associated with reactivated fault zones and shear zones: what can it tell us about deformation history? Geological Society, London, Special Publications 186 (1), 113–140.

Mock, J., Barbic, M., Smith, D., Schultz, D., Schultz, S., 2002. Shape effects in plasmon resonance of individual colloidal silver nanoparticles. The Journal of Chemical Physics 116 (15), 6755–6759.

Moiseenko, V., Kulik, E., 2010. Conditions of the formation of gold spheroidal nanoparticles. In: Doklady Earth Sciences. Vol. 431. Springer, pp. 324–326.

Möller, P., Kersten, G., 1994. Electrochemical accumulation of visible gold on pyrite and arsenopyrite surfaces. Mineralium Deposita 29 (5), 404–413.

Monger, J., Price, R., Tempelman-Kluit, D., 1982. Tectonic accretion and the origin of the two major metamorphic and plutonic welts in the Canadian Cordillera. Geology 10 (2), 70–75.

Müller, D., Kaminski, K., Uhlig, S., Graupner, T., Herzig, P. M., Hunt, S., 2002. The transition from porphyry-to epithermal-style gold mineralization at Ladolam, Lihir Island, Papua New Guinea: a reconnaissance study. Mineralium Deposita 37 (1), 61–74.

Nakamura, Y., Muto, J., Nagahama, H., Shimizu, I., Miura, T., Arakawa, I., 2012. Amorphization of quartz by friction: Implication to silica-gel lubrication of fault surfaces. Geophysical Research Letters 39 (21).

Nelson, E. P., Kullman, A. J., Gardner, M. H., Batzle, M., 1999. Fault-fracture networks and related fluid flow and sealing, Brushy Canyon Formation, West Texas. Faults and subsurface fluid flow in the shallow crust, 69–81.

Nelson, J., Colpron, M., 2007. Tectonics and metallogeny of the British Columbia, Yukon and Alaskan Cordillera, 1.8 Ga to the present. Mineral deposits of Canada: a synthesis of major deposit-types, district metallogeny, the evolution of geological provinces, and exploration methods: Geological Association of Canada, Mineral Deposits Division, Special Publication 5, 755–791.

Nelson, J., Kyba, J., 2014. Structural and stratigraphic control of porphyry and related mineralization in the Treaty Glacier–KSM–Brucejack–Stewart trend of western Stikinia. Geological fieldwork, 2014–1.

Oehler, J. H., 1976. Hydrothermal crystallization of silica gel. Geological Society of America Bulletin 87 (8), 1143–1152.

Ojea-Jiménez, I., Romero, F. M., Bastús, N. G., Puntes, V., 2010. Small gold nanoparticles synthesized with sodium citrate and heavy water: insights into the reaction mechanism. The Journal of Physical Chemistry C 114 (4), 1800–1804.

Okamoto, A., Saishu, H., Hirano, N., Tsuchiya, N., 2010. Mineralogical and textural variation of silica minerals in hydrothermal flow-through experiments: Implications for quartz vein formation. Geochimica et Cosmochimica Acta 74 (13), 3692–3706.

Okaya, D. A., Thompson, G. A., 1985. Geometry of Cenozoic extensional faulting: Dixie Valley, Nevada. Tectonics 4 (1), 107–125.

Page, B. M., 1964. Preliminary geologic map of a part of the Stillwater Range, Churchill County, Nevada. Map.

Parchman, W., Knox, J. W., 1981. Exploration for geothermal resources in Dixie Valley, Nevada. Bulletin of Geothermal Resources Council 10, 3–6.

Passchier, C. W., Trouw, R., 2005. Microtectonics: Deformation Mechanisms, 2nd Edition. Springer, Ch. 3, pp. 25–66.

Pearce, M. A., Gazley, M. F., Hough, R., Saunders, M., Fisher, L., Kong, C., Duclaux, G., May 2015a. A nanoparticulate origin for orogenic gold. In: AGU-GAC-MAC-CGU Joint Assembly Abstracts Listing. p. 305.
URL http://ja.agu.org/2015/wp-content/uploads/sites/2/2015/06/2015_Joint_Assembly_Abstract_Proceedings.pdf

Pearce, M. A., White, A. J., Fisher, L. A., Hough, R. M., Cleverley, J. S., 2015b. Gold deposition caused by carbonation of biotite during late-stage fluid flow. Lithos 239, 114–127.

Pereira, J., Dixon, C., 1971. Mineralisation and plate tectonics. Mineralium Deposita 6 (4), 404–405.

Peterson, E. C., Mavrogenes, J. A., 2014. Linking high-grade gold mineralization to earthquake-induced fault-valve processes in the Porgera gold deposit, Papua New Guinea. Geology 42 (5), 383–386.

Poirier, J.-P., Guillopé, M., 1979. Deformation induced recrystallization of minerals. Bulletin de Mineralogie 102 (2-3), 67–74.

Pol, V., Gedanken, A., Calderon-Moreno, J., 2003. Deposition of gold nanoparticles on silica spheres: a sonochemical approach. Chemistry of materials 15 (5), 1111–1118.

Pol, V. G., Srivastava, D., Palchik, O., Palchik, V., Slifkin, M., Weiss, A., Gedanken, A., 2002. Sonochemical deposition of silver nanoparticles on silica spheres. Langmuir 18 (8), 3352–3357.

Power, W. L., Tullis, T. E., 1989. The relationship between slickenside surfaces in fine-grained quartz and the seismic cycle. Journal of Structural Geology 11 (7), 879–893.

Pretium Resources Inc., 2013. Geology of the Brucejack property.
URL http://www.pretivm.com/files/doc_downloads/geology/2013429_Geology_for_website_APRIL2013_WSB.pdf

Ramsay, J. G., 1980. The crack-seal mechanism of rock deformation. Nature 284, 135–139.

Reich, M., Utsunomiya, S., Kesler, S. E., Wang, L., Ewing, R. C., Becker, U., 2006. Thermal behavior of metal nanoparticles in geologic materials. Geology 34 (12), 1033–1036.

Reith, F., Fairbrother, L., Nolze, G., Wilhelmi, O., Clode, P. L., Gregg, A., Parsons, J. E., Wakelin, S. A., Pring, A., Hough, R., et al., 2010. Nanoparticle factories: Biofilms hold the key to gold dispersion and nugget formation. Geology 38 (9), 843–846.

Reith, F., Stewart, L., Wakelin, S. A., 2012. Supergene gold transformation: Secondary and nano-particulate gold from southern New Zealand. Chemical Geology 320, 32–45.

Rivas, L., Sanchez-Cortes, S., Garcia-Ramos, J., Morcillo, G., 2000. Mixed silver/gold colloids: a study of their formation, morphology, and surface-enhanced Raman activity. Langmuir 16 (25), 9722–9728.

Roig, J.-Y., Faure, M., Truffert, C., 1998. Folding and granite emplacement inferred from structural, strain, TEM and gravimetric analyses: the case study of the Tulle antiform, SW French Massif Central. Journal of Structural Geology 20 (9), 1169–1189.

Rowe, C., Kirkpatrick, J., White, J., Faber, C., Caine, J., 2012. " Gray Areas": Silica gels, amorphous silica and cryptocrystalline silica on fault surfaces. In: AGU Fall Meeting Abstracts. Vol. 1. p. 2654.

Sander, M. V., Black, J. E., 1988. Crystallization and recrystallization of growth-zoned vein quartz crystals from epithermal systems; implications for fluid inclusion studies. Economic Geology 83 (5), 1052–1060.

Saunders, J., Schoenly, P., 1995. Boiling, colloid nucleation and aggregation, and the genesis of bonanza Au-Ag ores of the Sleeper deposit, Nevada. Mineralium Deposita 30 (3-4), 199–210.

Saunders, J., Unger, D., Kamenov, G., Fayek, M., Hames, W., Utterback, W., 2008. Genesis of Middle Miocene Yellowstone hotspot-related bonanza epithermal Au–Ag deposits, Northern Great Basin, USA. Mineralium Deposita 43 (7), 715–734.

Saunders, J. A., 1990. Colloidal transport of gold and silica in epithermal precious-metal systems: Evidence from the Sleeper deposit, Nevada. Geology 18 (8), 757–760.

Saunders, J. A., 1994. Silica and gold textures in bonanza ores of the Sleeper Deposit, Humboldt County, Nevada; evidence for colloids and implications for epithermal ore-forming processes. Economic Geology 89 (3), 628–638.

Saunders, J. A., 2012. Textural evidence of episodic introduction of metallic nanoparticles into bonanza epithermal ores. Minerals 2 (3), 228–243.

Saunders, J. A., Mathur, R., Kamenov, G. D., Shimizu, T., Brueseke, M. E., 2015. New isotopic evidence bearing on bonanza (Au-Ag) epithermal ore-forming processes. Mineralium Deposita, 1–11.

Schoenly, P. A., Saunders, J. A., 1993. Natural gold dendrites from hydrothermal Au-Ag deposits: characteristics and computer simulations. Fractals 1 (03), 585–593.

Scott, M., Chen, C.-C., Mecklenburg, M., Zhu, C., Xu, R., Ercius, P., Dahmen, U., Regan, B., Miao, J., 2012. Electron tomography at 2.4-angstrom resolution. Nature 483 (7390), 444–447.

Seward, T., 1976. The stability of chloride complexes of silver in hydrothermal solutions up to 350 C. Geochimica et Cosmochimica Acta 40 (11), 1329–1341.

Seward, T. M., 1973. Thio complexes of gold and the transport of gold in hydrothermal ore solutions. Geochimica et Cosmochimica Acta 37 (3), 379–399.

Sibson, R. H., 1992. Earthquake faulting, induced fluid flow, and fault-hosted gold-quartz mineralization. In: Basement Tectonics 8. Springer, pp. 603–614.

Sibson, R. H., Robert, F., Poulsen, K. H., 1988. High-angle reverse faults, fluid-pressure cycling, and mesothermal gold-quartz deposits. Geology 16 (6), 551–555.

Sillitoe, R. H., 2000. Gold-rich porphyry deposits: descriptive and genetic models and their role in exploration and discovery. Reviews in Economic Geology 13, 315–345.

Sillitoe, R. H., 2010. Porphyry copper systems. Economic geology 105 (1), 3–41.

Simmons, S. F., Brown, K. L., 2006. Gold in magmatic hydrothermal solutions and the rapid formation of a giant ore deposit. Science 314 (5797), 288–291.

Simmons, S. F., Brown, K. L., 2007. The flux of gold and related metals through a volcanic arc, Taupo Volcanic Zone, New Zealand. Geology 35 (12), 1099–1102.

Simmons, S. F., Browne, P. R., 1990. Mineralogic, alteration and fluid-inclusion studies of epithermal gold-bearing veins at the Mt. Muro prospect, Central Kalimantan (Borneo), Indonesia. Journal of Geochemical Exploration 35 (1), 63–103.

Smith, L., Forster, C., Evans, J. P., 1990. Interaction between fault zones, fluid flow and heat transfer at the basin scale. In: Hydrogeology of permeability environments. Vol. 2. International Association of Hydrological Sciences, pp. 41–67.

Steefel, C. I., Van Cappellen, P., 1990. A new kinetic approach to modeling water-rock interaction: The role of nucleation, precursors, and Ostwald ripening. Geochimica et Cosmochimica Acta 54 (10), 2657–2677.

Stefánsson, A., Seward, T., 2004. Gold (I) complexing in aqueous sulphide solutions to 500 C at 500 bar. Geochimica et Cosmochimica Acta 68 (20), 4121–4143.

Stipp, M., Stunitz, H., Heilbronner, R., Schmid, S. M., 2002. The eastern Tonale fault zone: a natural laboratory for crystal plastic deformation of quartz over a temperature range from 250 to 700 C. Journal of Structural Geology 24 (12), 1861–1884.

Taylor, B. E., 2007. Epithermal gold deposits. Mineral Deposits of Canada: A synthesis of major deposit-types, district metallogeny, the evolution of geological provinces, and exploration methods: Geological Association of Canada, Mineral Deposits Division, Special Publication 5, 113–139.

Tombe, S., 2015. The Brucejack epithermal Au-Ag deposit, northwestern British Columbia. Master's thesis, University of Alberta.

Trefry, J. H., Trocine, R. P., Klinkhammer, G. P., Rona, P. A., 1985. Iron and copper enrichment of suspended particles in dispersed hydrothermal plumes along the mid-atlantic ridge. Geophysical Research Letters 12 (8), 506–509.

Turkevich, J., Stevenson, P. C., Hillier, J., 1951. A study of the nucleation and growth processes in the synthesis of colloidal gold. Discussions of the Faraday Society 11, 55–75.

Turkevich, J., Stevenson, P. C., Hillier, J., 1953. The formation of colloidal gold. The Journal of Physical Chemistry 57 (7), 670–673.

Urai, J., Williams, P., Van Roermund, H., 1991. Kinematics of crystal growth in syntectonic fibrous veins. Journal of Structural Geology 13 (7), 823–836.

van der Elst, N. J., Brodsky, E. E., Le Bas, P.-Y., Johnson, P. A., 2012. Auto-acoustic compaction in steady shear flows: Experimental evidence for suppression of shear dilatancy by internal acoustic vibration. Journal of Geophysical Research: Solid Earth (1978–2012) 117 (B9).

Vikre, P. G., 1994. Gold mineralization and fault evolution at the Dixie Comstock Mine, Churchill County, Nevada. Economic Geology 89 (4), 707–719.

Wallace, R. E., Whitney, R. A., 1984. Late Quaternary history of the Stillwater seismic gap, Nevada. Bulletin of the Seismological Society of America 74 (1), 301–314.

Walsh, J., Childs, C., Imber, J., Manzocchi, T., Watterson, J., Nell, P., 2003. Strain localisation and population changes during fault system growth within the Inner Moray Firth, Northern North Sea. Journal of Structural Geology 25 (2), 307–315.

Weatherley, D. K., Henley, R. W., 2013. Flash vaporization during earthquakes evidenced by gold deposits. Nature Geoscience 6 (4), 294–298.

Weitz, D., Huang, J., Lin, M., Sung, J., 1985. Limits of the fractal dimension for irreversible kinetic aggregation of gold colloids. Physical review letters 54 (13), 1416.

Weitz, D., Oliveria, M., 1984. Fractal structures formed by kinetic aggregation of aqueous gold colloids. Physical Review Letters 52 (16), 1433.

Westcott, S. L., Oldenburg, S. J., Lee, T. R., Halas, N. J., 1998. Formation and adsorption of clusters of gold nanoparticles onto functionalized silica nanoparticle surfaces. Langmuir 14 (19), 5396–5401.

Whetten, R. L., Khoury, J. T., Alvarez, M. M., Murthy, S., Vezmar, I., Wang, Z., Stephens, P. W., Cleveland, C. L., Luedtke, W., Landman, U., 1996. Nanocrystal gold molecules. Advanced materials 8 (5), 428–433.

Wiese, G., Healy, T., 1970. Effect of particle size on colloid stability. Transactions of the Faraday Society 66, 490–499.

Williams, D. B., Carter, C. B., 1996. The transmission electron microscope. Springer.

Williams, D. B., Carter, C. B., 2009. Transmission electron microscopy: Thickness and bending effects. Springer US, Ch. 24, pp. 407–417.

Williams, L. A., Parks, G. A., Crerar, D. A., 1985. Silica diagenesis, I. Solubility controls. Journal of Sedimentary Research 55 (3).

Williams-Jones, A. E., Bowell, R. J., Migdisov, A. A., 2009. Gold in solution. Elements 5 (5), 281–287.

Wilson, C., 1994. Crystal growth during a single-stage opening event and its implications for syntectonic veins. Journal of structural geology 16 (9), 1283–1296.

Wirth, R., 2004. Focused Ion Beam (FIB) A novel technology for advanced application of micro-and nanoanalysis in geosciences and applied mineralogy. European Journal of Mineralogy 16 (6), 863–876.

Wuithschick, M., Birnbaum, A., Witte, S., Sztucki, M., Vainio, U., Pinna, N., Rademann, K., Emmerling, F., Kraehnert, R., Polte, J. r., 2015. Turkevich in new robes: Key questions answered for the most common gold nanoparticle synthesis. ACS nano 9 (7), 7052–7071.

Zezin, D. Y., Migdisov, A. A., Williams-Jones, A. E., 2011. The solubility of gold in H 2 O–H 2 S vapour at elevated temperature and pressure. Geochimica et Cosmochimica Acta 75 (18), 5140–5153.

Zoback, M. L., Anderson, R., Thompson, G., 1981. Cainozoic evolution of the state of stress and style of tectonism of the Basin and Range province of the western United States. Philosophical Transactions of the Royal Society of London A: Mathematical, Physical and Engineering Sciences 300 (1454), 407–434.

Zotov, A., Levin, K., Khodakovskiy, I., Kozlov, V., 1986. Thermodynamic parameters of Ag+ in aqueous solution at 273–573K. Geochem. Intl 23 (9), 23–33.

Appendices

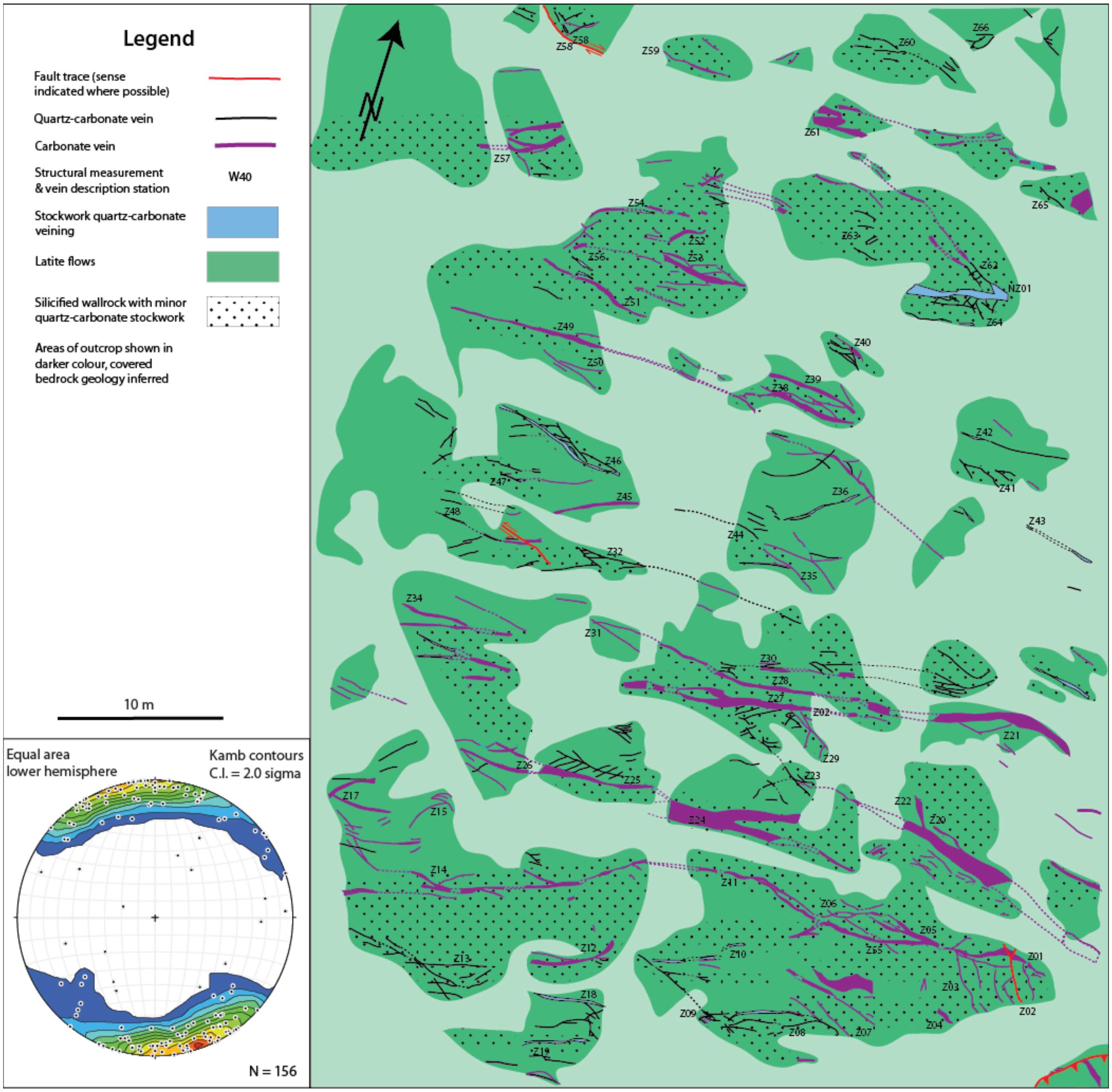

Figure A1 Lithology, stockwork quartz-carbonate veining and faults in map area 3 of the Brucejack Au-Ag deposit (see Figure 3.1 for location). Equal-area projection of poles to vein orientations shown for stations indicated on map; Kamb contour interval at 2σ indicate concentration of poles.